Fall 2014

Structural characterization of multimetallic nanoparticles

Vineetha Mukundan
Purdue University

Graduate School Form 30
(Revised 08/14)

PURDUE UNIVERSITY
GRADUATE SCHOOL
Thesis/Dissertation Acceptance

This is to certify that the thesis/dissertation prepared

By Vineetha Mukundan

Entitled
STRUCTURAL CHARACTERIZATION OF MULTI-METALLIC NANOPARTICLES

For the degree of Doctor of Philosophy

Is approved by the final examining committee:

Prof. Oana Malis

Prof. Erica Carlson

Prof. Ephraim Fischbach

Prof. Stephen M Durbin

To the best of my knowledge and as understood by the student in the Thesis/Dissertation Agreement, Publication Delay, and Certification/Disclaimer (Graduate School Form 32), this thesis/dissertation adheres to the provisions of Purdue University's "Policy on Integrity in Research" and the use of copyrighted material.

Prof. Oana Malis

Approved by Major Professor(s): _____

_____

Approved by: Prof. Andrew Hirsch 08/25/2014

Head of the Department Graduate Program Date

STRUCTURAL CHARACTERIZATION OF MULTIMETALLIC NANOPARTICLES

A Dissertation

Submitted to the Faculty

of

Purdue University

by

Vineetha Mukundan

In Partial Fulfillment of the

Requirements for the Degree

of

Doctor of Philosophy

December 2014

Purdue University

West Lafayette, Indiana

To my family

ACKNOWLEDGMENTS

There is a long list of people I need to thank without which this phase of my life is not complete. I thank my adviser, Prof. Oana Malis for her support and patience which saw to the completion of this research project. I thank my doctoral committee members for their guidance as I moved from an idea to a small body of research. I express gratitude to Prof. Ephraim Fischbach for guiding me in different stages of my grad school years. I thank Prof. Stephen Durbin for his support throughout my time at Purdue. I appreciate Prof. Erica Carlson for pointing me to few questions which I had not thought about before. I also thank Prof. Nicholas Giordano for nominating me for the Gary Wright Memorial Fellowship which funded a year of my graduate study.

I am grateful to Dr. Jean Jordan-Sweet for help with the experimental set-up at the beamline. I am much obliged to Prof C J Zhong, Dr. Jun Yin, Dr. Shiyao Shin and Dr. Jin Lou at SUNY, Binghamton for synthesizing the samples and discussions regarding them. I would like to acknowledge (Late) Prof. Gabriele Giuliani for his inspirational teaching of condensed matter physics courses which has improved my understanding of it by many leaps.

I owe my understanding of the TEM to Dr. Sergey Suslov, my TEM instructor at Purdue. He helped me find answers to my questions while learning and getting familiar with the TEM. Thanks Dr. Xin Xu, for helping me with the AFM. From the time we collaborated on a course project to the time he trained me on the Titan for EELS and in-situ experiments, I benefited from working with Dr. Mehmed Cem Akatay. Thanks, Dr. Jiayi Shao for the discussions we have had on TEM image analysis. Special thanks to Noah Opondo for helping me learn thin film processing techniques quickly.

This thesis would not have been possible without the enthusiasm of the people around me. I would like to thank my fellow doctoral students for their support and feedback. I had the pleasure to meet many friends and colleagues while at Purdue. I would like to thank the following individuals: Colin Edmunds, Itxaso Goikoetxea Idigoras, Baladithya Suri, Chandrasekhar Varanasi, Pinaki Bhattacharya, Sannah Ziama, Hochan Lee, Mayra Cervantes, Cristina Moody, Kari Frank, Sunanda Koduvayur, Sourav Dutta, Suprem Das and Mohammed Imrul Hossain. A heartfelt thank you to Mrs. Sandy Formica and Mrs. Linda Pacquay, for helping graduate students in different situations. I thank my friends turned phone pals who found time to check up on me every once-in-a while.

I take this opportunity to express my sincere gratitude to Smt. R Jayalakshmi, Smt. T N Kesi, Mrs. Aruna Nagarajan, Mrs. Dhanalkshmi, and my teachers at P S Senior Secondary School, Chennai for formally initiating me to Indian classical music and science. I would like to thank my mentors from the past, Prof. Neelima Gupte, Prof. Pranawa Deshmukh and Prof. Rama Govindarajan for their guidance and inspirational chats. I would like to thank Mrs. Abirami Srinivasan and Mrs. V Vijayshree for their company during my early college days. I thank my friends from JNCASR for the wonderful times in Bangalore. I am glad that friends and classmates from IITM have remained in touch over the years.

I realize Phd is not a smooth journey, like life itself. I would term my grad school years as years without breakfast. Many factors which nourished my life previously were simply absent. To name a few, chatting with my parents on many things got cut short to a few chats every 2-3 days, home food, temples etc. Of course, I badly missed the blazing sunshine back in Chennai. West Lafayette, except for the cold winters, is a nice town and became a home away from home over the years. Teaching through my time at Purdue helped in understanding the process and befriending young undergraduates. Organizing events for PGSA, WISP, WIP-grad and ASHA-purdue chapter, helped in getting closer to the student community. More importantly,

Purdue has a lot of resources for graduate students which go a long way in integrating grad-students community.

Lastly, I have no words to thank my family for having gone many extra miles to make things possible for me. Thank you, Amma (Mrs. Shanthi Mukundan) and Achchan (Mr. P K Mukundan). I would have done nothing without you. My parents and brother were responsible for whetting my interest in science, technology and Indian classical music. I am indebted to my brother, Vivek Mukundan for being a pillar of strength and support through swampy phases of PhD and my life in general. Amma and Achchan for believing in me and letting me have my way in spite of many tribulations and a lot of sacrifices. They are always there for me. My parents are meticulous and I always admire their brand of clarity of thought, grit and diligence. I admire the courage and the innocence with which my (late) granny lived out her life. If it had not been for the unconditional love and encouragement showered by my family, I would not have thrived.

TABLE OF CONTENTS

Page

LIST OF TABLES ix

LIST OF FIGURES x

ABSTRACT xvi

1 INTRODUCTION 1
1.1 Nanomaterials 1
1.2 Alloy nanoparticles 2
1.3 Application of noble metal nanoparticles: Fuel cells 4
1.4 Structural aspects affecting catalysis 6
1.4.1 Size effects 7
1.4.2 Shape and surface structure 8
1.4.3 Support effects 10
1.4.4 Influence of ligand 11
1.4.5 Reactive atmospheres 12
1.4.6 Alloying 14
1.4.7 Defects 15
1.4.8 Chemical ordering 16

2 THEORETICAL BACKGROUND ON METALLIC NANOPARTICLES 19
2.1 Introduction 19
2.2 Thermodynamics of bulk systems 19
2.3 Thermodynamics at surfaces: Nano regime 23
2.3.1 Melting 26
2.3.2 Chemical ordering and segregation in nanoparticles 28
2.3.3 Nanoparticle shape 34
2.4 Kinetics in metallic nanoparticles 37
2.4.1 Grain growth: coalescence and sintering 37
2.4.2 Kinetics of mixing 41

3 EXPERIMENTAL TECHNIQUES 43
3.1 Synthesis of nanoparticles 43
3.1.1 Supporting nanoparticles for different experiments 44
3.2 X-ray powder diffraction 46
3.2.1 Theory of x-ray diffraction 47
3.3 Synchrotron based x-ray diffraction 55
3.3.1 Beamline X20C at the National Synchrotron Light Source (NSLS) 56

Page

3.4 Transmission electron microscopy (TEM) . . . 63
3.4.1 High resolution transmission electron microscopy . . . 68
3.4.2 High angle annular dark field - scanning transmission electron microscopy (HAADF-STEM) . . . 71
3.4.3 Energy Dispersive X-ray spectroscopy (EDX) . . . 72
3.4.4 Electron energy loss spectroscopy (EELS) and Energy filtered transmission electron microscopy (EF-TEM) . . . 72
3.5 Other experimental techniques . . . 76
3.5.1 Atomic force microscopy (AFM) . . . 76
3.5.2 X-ray photoelexctron spectroscopy (XPS) . . . 77

4 LIMITED GRAIN GROWTH AND CHEMICAL ORDERING DURING HIGH TEMPERATURE SINTERING OF PtNiCo NANOPARTICLE AGGREGATES . . . 79
4.1 Introduction . . . 79
4.2 Experiments - Synthesis, instrumentation and measurements . . . 81
4.2.1 Nanoparticle synthesis . . . 81
4.2.2 Nanoparticle thermal processing and characterization . . . 82
4.2.3 *In situ* time resolved XRD . . . 83
4.3 Results and Discussion . . . 84
4.3.1 Early stages of sintering and lattice contraction . . . 85
4.3.2 Late stage sintering and grain growth . . . 88
4.3.3 Chemical ordering . . . 91
4.4 Conclusions . . . 92

5 NANOALLOYING AND PHASE TRANSFORMATIONS DURING THERMAL ANNEALING OF Pd AND Cu NANOPARTICLE MIXTURES . . . 95
5.1 Introduction . . . 95
5.2 Synthesis of Pd and Cu nanoparticles . . . 98
5.2.1 Copper nanoparticles . . . 98
5.2.2 Palladium nanoparticles . . . 99
5.3 Results . . . 99
5.3.1 Control samples . . . 100
5.3.2 PdCu nanoparticle mixtures on SiO_2/Si . . . 101
5.3.3 PdCu nanoparticle mixtures on other substrates . . . 112
5.4 Discussion . . . 115
5.5 Conclusion . . . 119

6 FUTURE RESEARCH DIRECTIONS . . . 121
6.1 Chemical composition and ordering studies of physical mixtures of Pd and Cu nanoparticles . . . 121
6.1.1 Nanoparticle mixtures Pd:Cu = 1:1 . . . 122
6.1.2 Nanoparticle mixtures Pd:Cu = 3:1 . . . 126
6.2 High temperature studies of PtNiFe . . . 130

Page
6.3 Simulations of coalescence and sintering of nanoparticles 133
7 SUMMARY 137
REFERENCES 141
VITA 154

LIST OF TABLES

Table Page

2.1 Scaling laws relating the neck size and diffusion coefficient [81–86] . . . 40

4.1 Summary of the nanoparticle samples examined in this study 83

LIST OF FIGURES

Figure		Page
1.1	Schematics of mixing pattern in alloy nanoparticles [1]. (a) Core-shell, (b) segregated, (c) mixed and (d) multi-shell nanoparticles.	3
1.2	Schematics of a fuel cell.	4
2.1	Atomic arrangement in disordered and ordered solid solutions.	22
2.2	Au-Cu system having different ordering structures. (a)Disordered structure (b) Cu-Au superlattice (c) Cu3Au superlattice [52].	23
2.3	Five common ordered lattices [52]. (a)$L2_0$ in Cu-Zn (b)$L1_2$ in Cu-Au (c)$L1_0$ of Au-Cu (d)$D0_3$ in Al-Fe (e)$D0_{19}$ in Cd-Mg.	24
2.4	Structure predicted by SMA-TB model for alloy AB. [4]	32
2.5	(a) Different shapes and sizes of Gold nanoparticles (b) Phase map of gold nanoparticles predicted by simulations [74].	35
2.6	Sintering mechanism proposed by Hawa and Zachariah [29].	39
3.1	X-ray beams striking on the atoms of a lattice.	47
3.2	Classical scattering of x-ray beam [100].	48
3.3	Scattering in a crystal. [100]	49
3.4	Crystallographic axes and Miller indices. [100]	51
3.5	Bragg's law and interplanar distance in a crystal. [100]	52
3.6	(a)NSLS at BNL (b) Beamlines with their main experiments in the inset.	56
3.7	XRD set up at the beamline X20C	58
3.8	Schematic block diagram of the XRD set up at beamline X20C [103].	59
3.9	Typical XRD data (a) Time evolution of the intensity of the scattered radiation from a PtNiFe nanoparticles sample (left panel)and the right panel is the XRD pattern at t= 320° s. (b) The XRD data represented in three dimensions with intensity of the X-ray peak, time and angle 2θ along the z, y and x-axis, respectively. (c) $\theta - 2\theta$ scans.	61
3.10	Schematic diagram of TEM	64

Figure Page

3.11 Two common modes of imaging in TEM (a) Imaging condition for STEM mode (b) Conventional mode of imaging [106]. 66

3.12 (a)High resolution image of Pd-Cu alloy nanoparticles (b) Fast Fourier transform of the HRTEM in (a) 69

3.13 (a)A typical STEM image of Pd-Cu nanoparticle mixture. 72

3.14 (a)A typical EDX spectra. (b) EDX maps of Pd-Cu nanoparticles. . . . 73

3.15 (a) The wide EELS spectrum with the Zero-loss peak, Plasmon peak and the edges of different elements. (b) Carbon edge at 284 eV and a very small Pd edge at 330eV (c) Cu doublet at 930 eV and 950 eV (d) Pre-edge (Figure d(i)), Post edge image (Figure d(ii)) and Cu mapped in an EFTEM image from a Pd:Cu sample (Figure d(iii)). 75

3.16 AFM images of a PtNiFe nanoparticles sample (a) Lower magnification (b) Higher magnification to measure size of nanoparticles as shown in (c). 76

3.17 Typical XPS data along with the elemental compositions of a PdCu nanoparticles sample. 78

4.1 TEM of PtNiCo nanoparticles (a) $Pt_{28}Ni_{18}Co_{54}$ (b) $Pt_{44}Ni_{14}Co_{42}$ (c) $Pt_{33}Ni_{27}Co_{40}$ (d) $Pt_{34}Ni_{16}Co_{50}$. 82

4.2 Overview of the temperature induced transformations in PtNiCo aggregates. (a) Time evolution of the XRD pattern for a $Pt_{44}Ni_{14}Co_{42}$ nanoparticle aggregate annealed at 700(Color map- red-high intensity; blue low intensity) (b)XRD spectrum at t=1200s showing cubic (111) and (200) peaks.t=0s represents the time the temperature was ramped from 100°C to 700°C at the rate of rate of 30°C/seconds. 84

4.3 TEM of the $Pt_{44}Ni_{14}Co_{42}$ nanoparticles after annealing at 850°C for 20 minutes. 85

4.4 Kinetics of the early stage sintering of $Pt_{44}Ni_{14}Co_{42}$ nanoparticle aggregate annealed at 700C. (a) Color map of the time evolution of the XRD pattern. (b) Time evolution of the (111) and (200) intergrated intensity and (c) Time evolution of the (111) and (200) average grain size t=0 represents the time the temperature is ramped from 100°C to 700°C at the rate of 30°C/s. 86

4.5 Model for the structural evolution during nanoparticle coalescence and sintering 87

Figure Page

4.6 Time evolution of (111) grain size for the $Pt_{44}Ni_{14}Co_{42}$ nanoparticles annealed at 700°C and fits of the data described in the text. T=0 represent the time the temperature was ramped from 100°C to 700°C at the rate of 30°C/s. 89

4.7 Pt-Co phase diagram showing the ordered phases. 91

4.8 Evidence of ordered structures in PtNiCo nanoparticles aggregates of different sizes and compositions annealed below 800°C. 92

5.1 (a) Color map of the XRD intensity evolution for Pd nanoparticles annealed at $500°C$ on SiO2/Si support in He atmosphere. (b) $\theta - 2\theta$ XRD scan after the thermal treatment of Pd nanoparticles in (a). (c) Color map of the XRD intensity evolution of Cu nanoparticles dispersed on SiO2/Si ramped annealed from 25 to 225°C in He gas. (d) $\theta - 2\theta$ XRD scan after the thermal treatment of Cu nanoparticles in (c). 102

5.2 (a) TEM image of the as-synthesized PdCu nanoparticles mixture (scale bar is 10 nm). (b) TEM image of SiO2/Si-supported PdCu nanoparticles after annealing at 300°C in He gas (scale bar is 50 nm). (c) TEM image of SiO2/Si-supported PdCu nanoparticles after annealing to 700°C in He gas (scale bar is 50 nm). 103

5.3 Phase diagram of bulk Pd-Cu [145]. Reprinted with permission of ASM International. All rights reserved. www.asminternational.org. 104

5.4 (a) Color map of the XRD intensity evolution for the Pd:Cu nanoparticle mixture on SiO2/Si substrate isothermally annealed at 300°C in a He atmosphere showing the formation of the ordered B2 phase. (b) Color map of the XRD intensity evolution of the Pd:Cu nanoparticle mixture on SiO2/Si ramped annealed from 300°C to 700°C in a He atmosphere showing the transformation of the B2 phase into a disordered fcc alloy phase. (c) $\theta - 2\theta$ XRD scans after annealing at 300°C and 700°C. . . . 105

5.5 (a) TEM image of the Pd:Cu nanoparticle mixture after isothermal annealing at 300°C on SiO2/Si substrate in a He atmosphere. (b) The FFT from a marked area in (a) is indexed as [311] zone axis of the PdCu B2 alloy phase. (c) High resolution image of the PdCu particle marked in (a) reveals uniform lattice fringes across the particle with an inter-planar distance of $2.14\mathring{A}$ that corresponds to [110] plane of B2 phase. Scale bars are 2nm and 5nm for images (a) and (c), respectively. 107

Figure Page

5.6 (a) Color map of the XRD intensity evolution for Pd:Cu nanoparticle mixture on SiO2/Si substrate isothermally annealed at 300°C in a forming gas atmosphere showing the formation of the ordered B2 phase. (b) Color map of the XRD intensity evolution of the Pd:Cu nanoparticle mixture on SiO2/Si ramped annealed from 300°C to 700°C in a forming gas atmosphere showing the transformation of the B2 phase into a disordered fcc alloy phase. (c) $\theta - 2\theta$ XRD scans after annealing at 300°C and 700°C. (d) Time evolution of the calculated XRD integrated intensities corresponding to the various peaks shown in (b) during ramp annealing from 300°C to 700°C. (e) Time evolution of the calculated XRD integrated intensities and domain size corresponding to the B2 phase shown in (a) during annealing at 300°C. (f) Time evolution of disordered fcc domain sizes calculated for the (111) and (200) peaks shown in (b) during ramp annealing from 300°C to 700°C. 110

5.7 (a) TEM image of the Pd:Cu nanoparticle mixture after annealing to 700°C on SiO2/Si substrate in a forming gas atmosphere. (b) The FFT from the region indicated in (a) reveal fcc structure along [110] zone axis with (111) inter-planar spacing of 2.16$\mathring{A}$. (c) A high resolution image of random alloy phase along [110] zone axis. Scale bars are 5 nm for images (a) and (c). 111

5.8 (a) Color map of the XRD intensity evolution for a Pd:Cu nanoparticle mixture on carbon-black substrate isothermally annealed at 300°C in a He gas atmosphere showing the formation of the ordered B2 phase. (b) Color map of the XRD intensity evolution for the Pd:Cu nanoparticle mixture on carbon-black ramped annealed from 300°C to 700°C in a forming gas atmosphere showing the transformation of the B2 phase into a disordered fcc alloy phase. (c) $\theta - 2\theta$ XRD scans after annealing at 300°C and 700°C. 113

5.9 (a) Color map of the XRD intensity evolution for a Pd:Cu nanoparticle mixture on alumina substrate isothermally annealed at 300°C in a He gas atmosphere. No B2 phase is formed in this process. (b) Color map of the XRD intensity evolution of the PdCu nanoparticle mixture on alumina ramped annealed from 300°C to 700°C in a He gas atmosphere showing the formation of a disordered fcc alloy phase. (c) $\theta - 2\theta$ XRD scans after annealing at 300°C and 700°C 115

5.10 HAADF-STEM and EDX maps of PdCu alloy nanoparticles after annealing to 700° on Carbon black in He gas: (a) HAADF-STEM, (b) Cu map, (c) Pd map, and (d) combined Pd and Cu map. It shows a slight Pd enrichment on the surface of the nanoparticles. 119

Figure Page

6.1 (a) Color map of the XRD intensity evolution for the Pd:Cu = 1:1 nanoparticle mixture on SiO2/Si substrate isothermally annealed at 450°C in a forming gas atmosphere showing the formation of the ordered B2 phase. (b) Color map of the XRD intensity evolution of the Pd:Cu nanoparticle mixture on SiO2/Si ramp annealed from 450°C to 750°C in a He atmosphere showing the transformation of the B2 phase into two disordered fcc alloy phases. (c) $\theta - 2\theta$ XRD scans after annealing at 450°C and 750°C. 123

6.2 (a) TEM image of the Pd:Cu= 1:1 nanoparticle mixture after isothermal annealing at 750°C on SiO2/Si substrate in forming gas atmosphere. (b) High resolution image of the PdCu particle marked in (a) reveals uniform lattice fringes across the particle with an inter-planar distance of 2.19$\mathring{A}$ that corresponds to [111] plane of Alloy 1 phase. (c) The FFT from a marked area in (b) is indexed as [311] zone axis of the PdCu alloy 1 phase. (d) High resolution image of the PdCu particle marked in (a) reveals uniform lattice fringes across the particle with an inter-planar distance of 1.93$\mathring{A}$ that corresponds to [002] plane of alloy 2 phase. (d) The FFT from a marked area in (e) is indexed as [110] zone axis of the PdCu alloy 2 phase. Scale bars are 5nm 125

6.3 (a) HAADF-STEM image of the Pd:Cu = 1:1 nanoparticles mixture. Scale bar is 50 nm (b) EDX spectrum obtained in (a). (c) EDX spectrum obtained in (a). Table: Pd and Cu compositions from (b) and (c). . . . 126

6.4 (a) Color map of the XRD intensity evolution for the Pd:Cu = 3:1 nanoparticle mixture on SiO2/Si substrate isothermally annealed at 450°C in a forming gas atmosphere showing the formation of the ordered B2 phase and another alloyed phase. (b) Color map of the XRD intensity evolution of the Pd:Cu nanoparticle mixture on SiO2/Si ramp annealed from 450°C to 750°C in forming gas atmosphere showing the incomplete transformation of the B2 phase into the disordered fcc alloy phase. (c) $\theta - 2\theta$ XRD scans after annealing at 450°C and 750°C. (d) Time evolution of the calculated XRD integrated intensities corresponding to the various peaks shown in (b) during ramp annealing from 450°C to 750°C. (e) Time evolution of the calculated XRD and domain size corresponding to the B2 and fcc phase shown in (a) during annealing at 450°C. (f) Time evolution of disordered fcc domain sizes calculated for the (111) and (200) peaks shown in (b) during ramp annealing from 450°C to 750°C. 127

Figure Page

6.5 (a) TEM image of the Pd:Cu = 3:1 nanoparticle mixture after isothermal annealing at 750°C on SiO2/Si substrate in forming gas atmosphere. (b) High resolution image of the PdCu particle marked in (a) reveals uniform lattice fringes across the particle with an inter-planar distance of 2.14$\mathring{A}$ that corresponds to [110] plane of Alloy 2 phase. (c) The FFT from a marked area in (a) is indexed as [111] zone axis of the PdCu alloy 2 phase. Scale bars are 5nm for images (a) and (c), respectively. 129

6.6 (a) HAADF-STEM image of the Pd:Cu = 3:1 nanoparticle mixture after annealing at 750°C. Scale bar is 100 nm (b) EDX spectrum obtained in (a). Table: Pd and Cu compositions from (b). 129

6.7 (a) Color map of the XRD intensity evolution for PtNiFe nanoparticle mixture spin cast on SiO2/Si substrate isothermally annealed at 950°C in He atmosphere. (b) Time evolution of the calculated XRD integrated intensities corresponding to the (111) and (200) phases seen in (a). (c) Time evolution of disordered fcc domain sizes calculated for the (111) and (200) peaks seen in (a). 132

6.8 Snapshots of the final structure of nanoparticles at t = 100 ps for three different pairs at three different temperatures. 135

ABSTRACT

Mukundan, Vineetha Ph.D., Purdue University, December 2014. Structural Characterization of Multimetallic Nanoparticles. Major Professor: Oana Malis.

Bimetallic and trimetallic alloy nanoparticles have enhanced catalytic activities due to their unique structural properties. Using *in situ* time-resolved synchrotron-based x-ray diffraction, we investigated the structural properties of nanoscale catalysts undergoing various heat treatments. Thermal treatment brings about changes in particle size, morphology, dispersion of metals on support, alloying, surface electronic properties, etc. First, the mechanisms of coalescence and grain growth in PtNiCo nanoparticles supported on planar silica on silicon were examined in detail in the temperature range $400 - 900$°C. The sintering process in PtNiCo nanoparticles was found to be accompanied by lattice contraction and $L1_0$ chemical ordering. The mass transport involved in sintering is attributed to grain boundary diffusion and its corresponding activation energy is estimated from the data analysis.

Nanoscale alloying and phase transformations in physical mixtures of Pd and Cu ultrafine nanoparticles were also investigated in real time with in situ synchrotron-based x-ray diffraction complemented by *ex situ* high-resolution transmission electron microscopy. PdCu nanoparticles are interesting because they are found to be more efficient as catalysts in ethanol oxidation reaction (EOR) than monometallic Pd catalysts. The combination of metal support interaction and reactive/non-reactive environment was found to determine the thermal evolution and ultimate structure of this binary system. The composition of the as prepared Pd:Cu mixture in this study was 34% Pd and 66% Cu. At 300°C, the nanoparticles supported on silica and carbon black intermix to form a chemically ordered CsCl-type (B2) alloy phase. The B2 phase transforms into a disordered fcc alloy at higher temperature (>450°C). The

alloy nanoparticles supported on silica and carbon black are homogeneous in volume, but evidence was found of Pd surface enrichment. In sharp contrast, when supported on alumina, the two metals segregated at 300°C to produce almost pure fcc Cu and Pd phases. Upon further annealing of the mixture on alumina above 600°C, the two metals interdiffused, forming two distinct disordered alloys of compositions 30% and 90% Pd. The annealing atmosphere also plays a major role in the structural evolution of these bimetallic nanoparticles. The nanoparticles annealed in forming gas are larger than the nanoparticles annealed in helium due to reduction of the surface oxides that promotes coalescence and sintering.

The nanoscale composition and structure of alloy catalysts affect heterogeneous catalysis. We also studied Pd:Cu nanoparticle mixtures of different compositions. In Pd:Cu of composition ratio 1:1, ordered B2 phase is formed during annealing at 450°C. During the ramped annealing from 450°C to 750°C, the B2 phase transforms into two different alloys, one alloy rich in copper and the other rich in Pd. This structural evolution is different from that of Pd-Cu system in bulk. In the 3:1 composition, the B2 phase dominates in the isothermal anneal at 450°C but a disordered alloy fcc phase is also formed. On annealing to 750°C, the disordered fcc phase grows at the expense of the B2 phase. These findings have important applications for the thermal activation of Pd-Cu nanocatalysts for EOR reactions.

1. INTRODUCTION

1.1 Nanomaterials

Nanomaterials are a class of materials whose dimensions vary from a few nanometers to a few hundreds of nanometers. The deluge of novel technologies and applications using nanomaterials developed over the last decade has reinforced the importance of this class of materials. Nanomaterials may be zero-dimensional (nanoparticles), one dimensional (nanorods and nanotubes) or two dimensional (thin films or a stack of films). Moreover, nanoparticles form aggregates in media such as colloidal suspensions, in matrices or on surfaces. Small nanoparticles are typically referred to as nanoclusters and may contain 10 to 2000 atoms. Two or more metals can be mixed to form inter-metallic compounds and alloys. This thesis focuses on PtNiCo nanoparticles and physical mixtures of Pd and Cu nanoparticles in the size range of 0.5nm to 20nm. These nanoparticles are interesting as catalysts in technologically important applications.

The nanostructures have fascinating physical and chemical properties that can be changes through control of the size, composition and degree of chemical ordering. Nanostructures undergo different phase reconstructions, different phase transformations and have modified electronic band structures as compared to their bulk counterparts. Design of new materials with tunable properties has generated enormous interest. Surface structure, composition and ordering properties of nano-scale alloys are of interest as they are important for tuning chemical reactivity. The surface energy contribution will be high due to nano-size and defects in the system. Some of the other size dependent properties include geometric and electronic structure, binding energy and melting temperature. All these characteristics of the nanomaterials can tailor their chemical and electronic properties.

1.2 Alloy nanoparticles

Thermal treatment has been known to affect the particle size, phase, morphology, dispersion of nanoparticles on the support, alloying and surface electronic properties. During thermal treatment, the nanoparticles are found to undergo structural transformations that may render the catalyst more or less efficient depending on the materials explored. The tendency of the nanoparticles to aggregate or coalesce typically leads to loss of catalytic activity and efficiency in oxygen reduction reaction (ORR). The goal of this thesis is to understand the structural aspects of nanocatalysts, and possibly identify the parameters that control the properties of the nanoparticles.

The structure, morphology and thereby the chemical properties of the nanoparticles can be fine tuned by mixing different metals at specific compositions. This presents a wide range of possibilities enabling many experiments and theoretical studies. For example, bimetallic catalysts have new properties that can be tailored as a function of the distributions and morphology of the two metals forming the alloy.

The mixing or chemical ordering of nanoparticles can take place in many different ways such as core-shell, sub-cluster segregation, ordered mixed alloy, randomly mixed alloy and multishell alloy. Figure 1.1 shows a schematic representation of some mixing patterns: core-shell (a), subcluster segregation (b), mixed (c), three shells (d), etc. The nanoparticles can be crystalline or non-crystalline. Non-crystalline materials may include icosahedra, decahedra, polytetrahedra, polyicosahedra, etc. Non-crystalline structures have efficient packing and internal strain. This is found in systems where there is size mismatch between the metals forming the alloy. The degree of mixing or ordering in nanoalloys depends on many factors such as the size of the metal atoms, strength of the bonds between the atoms, surface energies, charge transfer or electronic effects. Compared to mono-metallic clusters, bimetallic clusters can form homo-tops. Homo-tops have the same number of atoms (m+n=N), same compositions (m/n) but differ in the atomic arrangements and are used to describe alloy cluster isomers. With cluster size, the number of homo-tops increases in combinatorial ways.

The search for a most stable structure among homotops is difficult to perform. For example, for $Pd_{49}Pt_{49}$ particles, the number of homo-tops possible is 2.5×10^{28} [1].

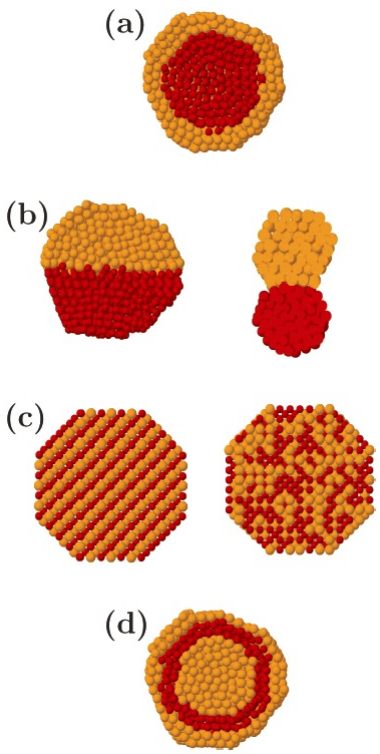

Figure 1.1. Schematics of mixing pattern in alloy nanoparticles [1]. (a) Core-shell, (b) segregated, (c) mixed and (d) multi-shell nanoparticles.

At the nanometer scale, the large surface to volume ratio increases the effect of surface energy of constituents. Moreover, the difference in surface energies of the components is an important quantity to predict their structure. To minimize the total energy, the material with smaller surface energy is expected to accumulate on the surface but this tendency is reversed in materials with large lattice mismatch. Moreover, the structure of nanomaterials produced by chemical methods is different from the thermodynamic equilibrium conditions of the bulk systems as the surface energy varies with surrounding medium and kinetics of reduction. So the final shape, size, structure and ordering in nanomaterials is the result of a competition between thermodynamics and kinetics.

1.3 Application of noble metal nanoparticles: Fuel cells

Fuel Cells are viable alternate sources of energy. They have high efficiency, are environmentally friendly, have low weight and represent an advantageous alternative power source. Fuel cells use reduction-oxidation reactions to generate power while conventionally using Platinum as catalyst. To make low cost commercially available fuel cells, it is very important to opt for robust and active nanostructured catalysts. Bimetallic and trimetallic nanoparticles have been found to have enhanced catalytic activities [2]. The nanostructures have high surface to volume ratios and more surface binding sites. These two factors affect catalytic performance dramatically.

Fuel cells are made up of three segments: the anode, the electrolyte, and the cathode. The net result of the reactions is that fuel is consumed, water or carbon dioxide is created, and an electric current is generated, which can be used to power electrical devices. The early designs of fuel cells were developed for use in the space vehicles and capsules of the 1960s.

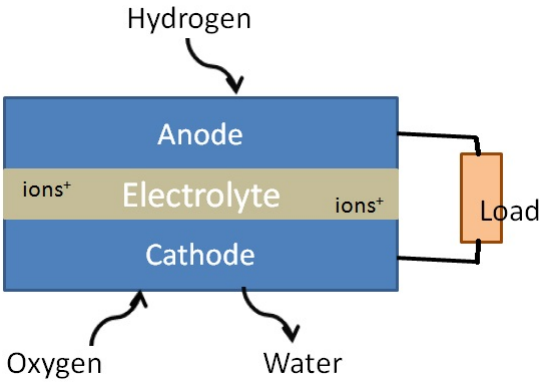

Figure 1.2. Schematics of a fuel cell.

At the anode a catalyst oxidizes the fuel, most commonly hydrogen, turning the fuel into a positively charged ion and a negatively charged electron. The electrolyte is a substance specifically designed so that ions can pass through it, but electrons cannot. The electrolyte material usually defines the type of fuel cell. The freed electrons travel through a wire creating a direct electric current. The ions travel

through the electrolyte to the cathode. Once reaching the cathode, the ions are reunited with the electrons and the two react with a third element, usually oxygen, to create water or carbon dioxide.

Catalysis consists of increasing the rate of a chemical reaction in the presence of catalyst. The catalyst brings down the energy cost of the reaction. For example, to control pollution, CO in automobile exhaust has to be oxidized. The energy required for the non-catalyzed reaction $CO + \frac{1}{2}O_2 \rightarrow CO_2$ is 500KJ/mole. This is the energy needed to break the oxygen molecule and form the CO_2. When Pt is used as a catalyst, the oxygen molecule gets split more easily and the energy of the reaction is reduced to 50-100 KJ/mole.

Chemical activity, stability and selectivity are important parameters for evaluating catalysts. Activity refers to the rate at which the reactants are consumed or the product is formed on the surface of the catalyst. Stability is the measure of the catalyst efficiency/performance as a function of time. Selectivity for a particular product from a given set of reactants is the rate of that product formation as compared to the total conversion rate. Selectivity is affected by four important factors (a) surface structure of the metal, (b) presence of selective blocking sites, (c) oxide-metal interface sites, and (d) bi-functional sites [3]. The catalysts are said to be supported when they are dispersed on other materials, normally oxide materials like alumina, silica, titanium dioxide, etc. For any catalyzed reaction, it is very important to know the sequence of reaction steps and this sequence is called the reaction pathway. This reaction pathway is important to figure out exactly how the catalytic material affects the energetics of the reaction.

Current research has the goal of improving the efficiency and the cost of catalysts. Typically the nanomaterials used as catalysts are of sizes below 10nm. The size, support and reaction atmospheres play major roles in the activity, selectivity and stability of these catalysts. Alloying affects the electronic and structural properties of the catalysts. Bimetallic nanoparticles may lead to synergistic catalytic effects that involve changes in local electronic properties of the nanoparticles and changes in

the strength of the surface adsorption for oxygen reduction reactions (ORR). In this thesis, we study a few examples of bimetallic nanoparticle systems and compare their structure to that of their monometallic bulk counterparts. The reactivity of metal surfaces can be manipulated to strengthen or weaken the adsorbate-surface bond, primarily in three ways: (a) Choice of metals (b) Atom coordination by changing the size, shape, surface orientation and (c) alloying [4]. Selectivity and activity of the bimetallic catalysts can change significantly with the surface composition, which can be changed by the reactive atmospheres (oxidizing or reducing) and the heat of sublimation of the elements.

A direct methanol fuel cell (DMFC) is a typical example of a fuel cell. In DMFC, methanol is electro-oxidized to generate electrical currents and CO_2. A good catalyst provides efficient sites for adsorption, desorption and electron transfer at the catalyst/electrolyte interface. Pt is typically used as catalyst in anodes and cathodes. Moreover, the pure Pt catalysts are easily poisoned by strongly adsorbed intermediates like the CO-intermediates. In Pt-bimetallic catalysts, the Pt activates the C-H bonds and produces Pt-CO while the second metal activates the water to accelerate oxidation of surface adsorbed CO to CO_2 [5]. These bimetallic catalysts are called bi-functional. Furthermore, a tri-metallic catalyst can minimize CO poisoning. When Mo is added to Pt-Ru for example, the catalysts are more active and Mo promotes electro-oxidation of the CO at lower potential therefore modifying the reaction path. DMFC with Pt-Ru-Mo/Carbon Nanotube as anode performed better than Pt-Ru/Carbon Nanotube [6].

1.4 Structural aspects affecting catalysis

Traditional preparation of nanocatalysts occurs in three steps: introduction of metal precursors on a support, calcination in oxidative atmosphere, and reduction in hydrogen. Originally, this process produced catalysts that had poor activity due to varied facets and sizes. To develop efficient catalysts, it is very important to tailor

their structural characteristics. Structural aspects of multi-metallic nanoparticles that affect catalysis include size, shape, phase, chemical ordering, defects and alloying. These are in turn affected by the influence of ligands used as capping agents in nanoparticles, the substrates or supports, reactive atmospheres, etc. By changing one parameter at a time, we can understand the effect it has on the structure-property relationship of the catalysts. This way we will be able to build a robust design for catalysts. The remainder of this chapter gives a few examples of how these factors play a role in the catalytic properties of the nanoparticles.

1.4.1 Size effects

The nanomaterials are ideal systems where the size reduction brings about changes in their electronic structure. From introductory quantum mechanical calculations, we know that the discrete energy levels of nanoparticles depend on the size of the particle. Naitabdi and Cuenya [7] found that Au nanoparticles supported on TiC exhibited non-metallic behavior due to quantum size effects. The band gap of Au was found to increase with decreasing cluster size, but for clusters below 1.3nm it showed a decrease in band gap.

Size and shape have very strong influence on electronic structure and can be manipulated to optimize the catalytic properties of nanoparticles. The synthesis routes are optimized to deliver nanoparticles with narrow size distribution. Somorjai and Park explored the effect of size on the chemical selectivity and activity of monometallic catalysts like Pt and Fe [8]. On decreasing the size of the nanoparticles, a higher number of uncoordinated atoms becomes available for interaction with chemical adsorbates, helping in dissociation of certain molecules or stabilizing them. Santra et al. [9] reported that metal clusters undergo changes of lattice parameters, band width, band splitting, and core-level binding energy shifts as a function of cluster size. They explored many single metals on ultra-thin oxide support materials by *in situ* scanning

tunneling microscopy and spectroscopy. These experiments prove that size affects the physical and electronic properties of the nanoparticles.

Catalytic activity may increase, decrease or remain the same with changes in the size of the nanoparticles. Frenkel and coworkers have shown that the catalytic activity for ammonia decomposition of Ru nanoparticles supported on Al_2O_3 changes by 2 orders of magnitude when their size changes from 0.8nm to 7nm [10]. High activity is also observed in nanoclusters as demonstrated by Heiz and coworkers [11] in the case of Pt clusters on MgO (100) films. Typically the nanoparticles of sizes less then 1nm behave as molecules and their activity is related to their orbital structure and the number of atoms. The number of atoms influences the catalytic activity strongly. They concluded that a morphological transition from 2D to 3D configuration happened when the number of atoms per cluster exceeds 13. Gold catalysts for CO oxidation were found to have higher rate of the reaction as their size decreases leading to lower coordination of atoms. The catalytic activity of nanoparticles can also remain constant with size as in the case of Pt on SiO_2 for benzene hydrogenation [12].

Nanoclusters, unlike bulk, have higher multiplicity of possible structures. Depending on size and temperature, monometallic nanoclusters can exist as icosahedral, decahedron or truncated octahedron [13]. Theoretical studies have explored these 3 structures with different sizes made of different metals, including Pt and Pd. Baletto et al [14] have shown that small nanoclusters exist as icosahedral shape and truncated octahedron for larger nanoparticles. The size of the nanoparticles also affects the charge transfer within the nanoparticles.

1.4.2 Shape and surface structure

Shape plays an important role in optimizing the activity in electrocatalysis by increasing the number of active sites promoting catalysis.

Narayanan and El-Sayed [15] calculated kinetic parameters for capped Pt nanoparticles of cubic, tetragonal and nearly spherical shapes in the electron transfer reaction

between hexacyanoferrate (III) and thiosulfate ions. Using absorption spectroscopy and obtaining the rate constant of the reaction, they found the activation energy was the lowest for tetrahedral nanoparticles. The tetrahedral nanoparticles are smaller in size and have sharp corners and edges capable of being chemically active or easily dissolved promoting catalytically active sites. Subsequently they confirmed faster dissolution of surface Pt atoms on tetrahedral particles compared to cubic and spherical nanoparticles.

Xu et al. [16] explored Ag nanoparticles of cubic, truncated triangular nanoplates and spherical shapes for oxidation of styrene. The rate of reaction for the cubic particles was fourteen times higher than that of triangular nanoplates and four times higher than that of spherical nanoparticles. Higher activity for nanocubes was attributed to the (100) facets.

Tian et al. [17] concluded that the Pt nanoparticles of tetra-hexahedral shape with high index facets have enhanced activity for electro- oxidation of formic acid and ethanol compared to Pt nanospheres. They attributed this behavior to increased steps and dangling bonds promoting catalysis.

The surface structure plays a critical factor in the catalytic properties. Surface structure like the edges, corners, particle- substrate interfacial sites have been known to change the catalytic activity [9,18]. In ammonia synthesis using iron, Somorjai and co-workers have concluded that the surface structures with (111) and (211) orientation have higher activity than surfaces with (100), (210) and (110) orientation [19]. It was also studied theoretically by Van Hardeveld and Hartog that the number of edge atoms increases over the total number of surface atoms when the size decreases below 5nm [20]. Freund at al. [21] showed that in the decomposition of methanol on Pd crystallites, the carbon and hydrocarbon species block edges and steps. As a result, they conclude that the activity for carbon-oxygen bond breakage is enhanced.

Van Santen [22] rationalizes the importance of step edges in dissociative adsorption for the cleavage of the πbond for molecules like CO, NO, N_2 and O_2. The cleavage of the σ-bond, for C-C in alkane hydrolysis increases with the presence of step or kinks.

Tao et al. [23] examined the behavior of stepped Pt single crystals in CO gas. From their scanning tunneling microscopy experiments in ultra-high vacuum conditions, they found the doubling of terrace width and step height on the Pt (557) surface leading to increased surface roughness. No such trend was observed in Pt (332) surfaces. Upon introducing CO at high pressure, the surface coverage of CO was increased and the surfaces underwent restructuring that helps in increasing its electrochemical activity due to step formation.

1.4.3 Support effects

The role played by the substrate in catalytic reactivity of supported nanoparticles cannot be neglected. The substrate can affect catalysis by (a) preventing nanoparticles from coarsening (b) leading to formation of reaction sites (c) changing the structure and shape (d) charge transfer between substrate and nanoparticles (e) stabilizing intermediate reaction species, etc.

Pt nanoparticles supported on carbon were found to undergo dissolution of Pt with particle agglomeration leading to loss of surface area and a decrease in catalytic performance [24]. The support plays a major role in promoting catalysis by acting as an adsorbent of the gases involved in the reaction. Gold catalysts with different support materials were explored for CO oxidation by ion-molecule-reaction mass spectrometry [25]. Enhanced catalysis was observed for active supports like Fe_2O_3, TiO_2, NiO_x, etc., which adsorb the oxygen molecule strongly. Heiz and coworkers have shown that the defective MgO (100) substrates with oxygen vacancies strongly bind the Au clusters and increase their electronic charge leading to a low energy pathway for CO oxidation [26]. Sometimes the substrates can help reactants like H_2 adsorb onto the metal nanoparticles and then diffuse on the substrate with lower energy pathway for the formation of H-atoms [27]. Au nanoparticles dispersed on two different substrates of CeO_2 and ZnO (0001) were considered for water gas shift

reaction. Higher activity was found for Au-CeO_2 system due to the role of oxygen vacancy formation in CeO_2 [28].

The support can also get directly involved in the catalytic reaction, or control the mobility of the catalytic materials leading to lower energy requirement for the reaction. It was also found that the crystal structure of the support affects the reactivity of the catalysts. Yan et al. reported that the brookite structure of TiO_2 reduces sintering of Au nanoparticles as compared to the anatase structure of TiO_2 [29]. In some cases reported, the noble metals supported on reducible oxides experience strong metal-support interaction (SMSI) due to the strong metal-suboxide bond. A three way catalyst is used for simultaneous conversion of CO, hydrocarbons and nitrogen oxide in automobile exhaust. Maire et al [30] explored the Pt-Rh nanocatalysts on CeO_2- Al_2O_3 and found that alloys were formed with low sintering. Ceria also improves metal dispersion. The noble-metal catalysts exhibited epitaxy on CeOx due to strong metal support interaction.

1.4.4 Influence of ligand

Capping agents are polymers or other organics that bind to the surface of nanoparticles to prevent aggregation, stabilize the nanoparticles in solution during synthesis, and preserve their structure. Typically the product of colloidal synthesis of metallic nanoparticles has a core-shell structure with a metallic core and organic material as shell. Essentially these capping agents can resist the access of different molecules to the nanoparticle surface or promote formation of different compounds with the ligands. The alloying and final sizes of the nanoparticles are also influenced by the environment of the capping agent around the nanoparticles.

Capping agents can form complexes with metal precursors and affect the final shape of the nanoparticles. Niu et al [31] monitored the shape evolution of the oleylamine capped Pd nanocrystals. Palladium acetylacetonates (metal precursor) forms an intermediate complex at room temperature. Reduction followed by increased

amount of oleylamine lead to the formation of different polyhedrons. Here the capping agent oleylamine plays a crucial role in shape evolution by mediating the interplay between crystal strain and surface energy.

The capping agents or the surfactant molecules of the nanoparticles have also been known to change the chemical ordering in them. Coordinating CO molecule to PdAu leads to core-surface segregation inversion driven by the strong Pd-CO bonding [32]. Xian et al [33] examined the poly(N-vinyl-2-pyrrolidone) (ligand) capped Pd nanoparticles and found an interesting size-dependent interaction of capping molecules with Pd nanocrystals. Their average size decreases monotonically as the ligand monomer/Pd molar ratio increases up to 1.0. Charge transfer was confirmed to occur from a chemisorbed ligand to Pd nanocrystals. This capping agent is reactive in catalytic environment consuming oxygen and nitrogen atoms.

1.4.5 Reactive atmospheres

Depending on the reactive atmospheres and the type of support, the metal particles can undergo many different changes such as surface oxide formation, sintering, restructuring or redispersion. These processes involve chemisorption in specific environments leading to increase or decrease in catalytically active areas/sites such as steps, kink sites, vacancies at the edge, etc. Room temperature CO adsorption on Au or Pt nanoparticles can lead to clustering [23] or faceting [34]. Tao et al [23] explored small Pt particles with stepped single crystal surfaces and found them to undergo restructuring to form nano-sized clusters from flat terraces. Upon pumping out the CO, the surfaces revert to the original morphology. This demonstrates the connection between coverage of reactant molecules and the atomic structure of the catalytic surfaces under specific reaction conditions. Madey and coworkers [34] in their review examined the atomically rough surfaces of transition metals like W, Mo, Ir, Rh and Re and alloy NiAl that form facets when they adsorb gases or metallic monolayers when annealed at high temperature. They discussed faceting with thermodynamics

involving the surface structure, surface reactivity and surface electronic properties. They have demonstrated the use of faceted surfaces as templates for selective growth and nucleation of metallic nanoclusters.

M. Cabie et al. [35] also observed the Pt nanoparticles in a gas atmosphere by environmental transmission electron microscopy during cycles of oxidation-reduction. In oxygen atmospheres the Pt nanoparticles form more (100) faces than in the case of hydrogen environment due to the stronger adsorption of oxygen on the (100) surfaces. The shape formation was found to be reversible with increase or decrease of the (111)/(100) ratio in hydrogen and oxygen atmospheres with few millibars pressure.

Au-Cu bimetallic nanoparticles dispersed on ordered mesoporous silica SBA-15 are more active in CO oxidation than their monometallic counterparts. Initially the catalysts consisted of Au_3Cu_1 and Cu_2O, as Cu was oxidized during the pre-treatment conditions. During CO oxidation, CO adsorbs to Au and also reacts with oxygen in CuO_x [36]. Similar behavior was also observed in Au-Ag and Au-Pd systems. Freund and coworkers [37] monitored Au nanoparticles deposited on FeO (111) thin films in different atmospheres like H2, O2, CO and CO+O_2 by scanning tunneling microscopy. In CO and CO+O_2 atmospheres, there was destabilization of the Au nanoparticles at step edges leading to formation of mobile Au species capable of moving on the oxide support.

Nolte et al. [38] investigated Rh nanoparticles supported on MgO(001) using grazing incidence x-ray diffraction and TEM experiments. On oxidation they found an increase in the total area of (100) facets at the expense of (111) surfaces. This was reversible in nanoparticle reduction during CO oxidation.

The influence of CO and H adsorption on the Pd, Au and Pt nanoclusters was detailed in the calculation by Paz-Borbon et al. [39]. They found that the H-adsorption releases surface stress and forms five-fold symmetry structures. CO adsorption does not change the energy of these clusters. Another effect of reactive species on the nano alloy is the formation of stable compounds like oxides, sulphides or carbides. For example, exposure of Pt-Co to oxygen leads to the formation of a wurzite CoO

oxide shell [40]. The electronic structure of the cobalt oxide in the nanoscale was different from the bulk counterpart.

1.4.6 Alloying

The composition in bimetallic systems is important for reducing cost of catalysts and enhancing catalytic efficiency by modification of electronic properties. Charge transfer phenomena between two metals change the binding energy of adsorbates, lowers the energy barrier of the reaction, increases resistance to poisoning of the catalysts, etc. The nature of the second metal, the preparation and the treatment of the nanoparticles have lasting influence on the activity of alloy nanoparticles.

Direct methanol fuel cells are being made economically viable by alloying Pt with less expensive metals such as Ru, Cr, Sn, Os, etc. These metals not only lower the costs but also have enhanced activity at the electrodes and resist poisoning caused by the by-products of the fuel cell reactions [41]. In particular, Ru provides preferential sites for OH adsorption that oxidizes to CO_2 from alcohol, preventing the CO poisoning by accumulation on the catalysts.

Croy et al. [42] experimented with PtM (M = Au, Pd, Ru and Fe) nanoparticles supported on ZrO_2 for methanol decomposition. They reported changes in stability of PtOX species on these nanoparticles depending on the affinity for oxygen of the secondary metals. Low reactivity was reported for these nanoparticles compared to pure Pt clusters.

Recently Stamenkovic et al. [43] have shown that the $Pt_3Ni(111)$ surface is ten-folds more active than the Pt(111) surface in the oxygen reduction reaction in polymer electrolyte membrane fuel cells (PEMFC). This was attributed to the compositional oscillation on Pt_3Ni surface and the lowering of the d-band center. Furthermore, they established that a strong relationship exists between surface electronic structure and activity in oxidation-reduction reactions.

In some cases, the addition of another metal to the noble metal leads to promotion of catalytic activity. Pd is a good catalytic metal for selective hydrogenation of 1,3-butadiene. When combined with Au, Piccolo et al. have shown that PdAu is more selective to butene formation than pure Pd surfaces. The increased activity is due to an Au-induced weakening of the butane-Pd bond [44].

In some cases, bimetallic nanoparticles have better catalytic properties than the monometallic counterparts because they reduce contamination of the catalysts. In sulfuration process, the number of sulphur atoms decreased in the vicinity of Pt atoms compared to that in monometallic Pt catalysts. Using extended x-ray fine structure (EXAFS) measurements, Bensaddik et al. [45] showed that the second metal modifies the behavior of the Pt clusters on adsorption of H_2S. Ye et al. [46] have shown that the Pt-Pd dendrimer nanoclusters (consisting of 180 atoms) have a relative catalytic activity enhancement of 2.4 compared to otherwise identical monometallic Pt nanoparticles.

Bimetallic catalysts are important in petrochemical industry providing high activity, selectivity and stability for the methyl cyclopentane ring opening. For example, Pt-Ir is a promising candidate for the conversion of methyl cyclopentane because it is resistant to surface carbon deposits [47].

1.4.7 Defects

Defects such as stacking faults and oxygen centers enhance the electrochemical activity of catalysts. Ducreux et al. [48] examined the Co catalysts supported on silica and alumina using *in situ* x-ray diffraction. They confirmed the presence of stacking faults and the coexistence of both fcc and hcp particles. Co catalysts are used in the Fischer-Tropsch process where the hydrocarbons are produced from hydrogen and carbon monoxide.

Gan et al. [49] explored the role of pentagon defects on the bamboo shaped carbon nanotubes used as substrates to disperse Pt-Ru nanoparticles for anodes in direct

methanol fuel cells. When compared to the conventional carbon nanotube and Vulcan carbon black, the bamboo shaped carbon nanotube showed highest activity and this was attributed to the interaction of the defects with the Pt-Ru nanoparticles involving charge transfer from the nanotubes to the nanocatalysts.

1.4.8 Chemical ordering

Chemical ordering at the nano scales is different from that in bulk alloys. The ordering process in alloys is affected by the presence of surfaces. Any alloy would phase separate or order at low temperature due to interatomic interactions. When the interaction is strong, the alloy will have ordered structures up to the melting temperature. When the interaction is weak, the alloy forms a solid solution. In the intermediate regime, there can be one or more ordered phases before it forms disordered structures below melting point. Upon adding an element B to an element A, we expect the lattice parameter of the alloy to change. Even when forming ordered structures in alloys, the symmetry decreases and there might be deformation of the unit cell. Ordering in nanoparticles is the result of the interplay between chemical effects and structural effects.

Mayrhofer et al [50] studied PtCo nanoparticles and found that the surface segregation of Pt with Pt_3Co core results in superior activity in oxygen reduction reaction as compared to plain Pt catalysts. The surface segregation of Pt is possible due to the higher adsorption enthalpy of CO on Pt than on Co. The mass activity of Pt shell with Pt_3Co core nanocatalysts increases by a factor of 2-2.5 in alkaline solutions for oxygen reduction reaction compared to that of pure Pt and just Pt_3Co nanocatalysts. Miegge et al [51] examined the Pd-Ni alloy with low Pd compositions and found that the activity of alloys Pd_1Ni_{99} and Pd_5Ni_{95} towards 1,3 butadiene hydrogenation was comparable to that of Pd (111) and (110) single crystal faces. This was attributed to the surface enrichment by Pd, and the surface composition was found to be 20% and 50% for Pd_1Ni_{99} and Pd_5Ni_{95}, respectively. This behaviour was investigated using

the x-ray photoelectron spectroscopy and low energy ion spectroscopy and explained in terms of geometry and electronic effects.

As discussed above, it is a major challenge to create functional nanoparticles for catalysis by tuning their size, shape, phase, structure, composition and surface properties. In this thesis, we explore thermally activated processing of multi-metallic nanoparticles studying different aspects of their structure. We briefly discuss the theoretical aspects of the thermodynamics and kinetics involved in multi-metallic nanoparticles in chapter 2. Chapter 3 gives an overview of the experiments performed in this study. Chapter 4 presents a study of sintering mechanisms in tri-metallic nanoparticles (PtNiCo). Chapter 5 reviews the evolution of Pd and Cu nanoparticles mixtures as a function of different substrates, different annealing atmospheres, and chemical ordering etc. Chapter 6 presents a few results obtained in other multi-metallic nanoparticles systems and future research directions.

2. THEORETICAL BACKGROUND ON METALLIC NANOPARTICLES

2.1 Introduction

Reducing materials to the nanoscale provides a fundamental mechanism to modify their behavior and properties. The physical and chemical properties of nanoparticles can be tailored by changing their size, surface ordering and phase. Two structural aspects have strong influence on the properties of nanoparticles. First, the surface to volume ratio in the nanoparticles is large. Second, the translational invariance in nanoscale systems is no longer present. Nanomaterials can have non-crystallographic geometries such as structures with five-fold symmetry.

The thermodynamics and kinetics involved in the structural transformations of metallic nanoparticles induced by thermal treatment are the main focus of this thesis. The physical properties of the materials in the nano regime are different from those in bulk. One such example is the decrease in the melting temperature with the decrease in size of the nanoparticles. We briefly discuss the thermodynamics and kinetics relevant to our present study. This chapter also presents a brief literature survey on the theoretical studies on chemical ordering, melting, shape and sintering of noble metal nanoparticles.

2.2 Thermodynamics of bulk systems

Phase transformations are changes that occur within a material system from one phase to another. A typical example is the change of phase of a particular structure to a different phase in an alloy. A phase has unique structure, composition and homogeneous properties. A phase transformation occurs due to instability of one

phase compared to another. A system in equilibrium is the most stable state. At constant temperature and pressure a system is stable when the Gibbs free energy is lowest dG=0. The Gibbs free energy G is related to the temperature T and enthalpy H by the equation G = H – TS where S is the entropy (degree of order).

A single component bulk system has either a pure element or one type of molecule throughout the system. The variation in G for a single component system is given by dG = -S dT + V dP. At constant pressure $\left(\frac{\partial G}{\partial T}\right)_P = -S$. For temperature up to the melting temperature T_m, the solid phase is the stable phase and above T_m the liquid phase is in equilibrium. At the equilibrium temperature T_m, the free energy of solid and liquid are equal and the entropy of fusion L is given by $\Delta S = \frac{\Delta H}{T_m} = \frac{L}{T_m}$. If the solid phase can exist in different structures, the free energy curves of these different structures are important and the temperature at which the curves intersect gives the equilibrium temperature for a polymorphic (a solid material can exist in more than one crystal structure) transformation. For example, iron transforms from bcc (body centered) ferrite to fcc (face centered) austentite at $910°C$ at atmospheric pressure.

If the single component system is heated, its enthalpy is raised by C_p, the specific heat at constant pressure. In this case, the specific heat is used to define the enthalpy and entropy as follows: $H = \int_{298}^{T} C_P dT$ and $S = \int_{298}^{T} \frac{C_P}{T} dT$. At constant temperature, the free energy of a phase increases with pressure as $\left(\frac{\partial G}{\partial P}\right)_T = V$. If two phases have different volumes, their free energies vary differently. For the single component system with two different phases in equilibrium, the change in pressure with respect to change in temperature is given by $\left(\frac{\partial P}{\partial T_{eq}}\right) = \frac{\Delta H}{T_{eq} * \Delta V}$ and this is the Clausius-Clapeyron equation.

In the bulk phase when two materials get mixed, they form a binary solution. Here the enthalpy of mixing plays a big role. Suppose elements A and B mix to form a binary solution. In 1 mol solution, $X_A + X_B = 1$ where X_A is the mole fraction of element A and X_B is the mole fraction of element B. The Gibbs free energy is given by $\Delta G_{mixing} = \Delta H_{mixing} - T\Delta S_{mixing}$ where ΔH_{mixing} is the enthalpy of mixing, T is the temperature and ΔS_{mixing} is the entropy of mixing. For ideal solutions $\Delta H_{mixing} = 0$,

$\Delta G_{mixing} = -T\Delta S_{mixing}$, and the entropy of mixing is related to mole fractions of the elements A and B as $\Delta S_{mixing} = -R\left(X_A lnX_A + X_B lnX_B\right)$ where R is the universal gas constant. It is also important to understand the effect of adding or removing atoms from the binary solutions. When the number of atoms, T and P are allowed to vary, the free energy is given by $dG = -SdT + VdP + \mu_A dn_A + \mu_B dn_B$ where μ_A and μ_B are the chemical potential of A and B.

Regular solutions have $\Delta H_{mix} \neq 0$ as found in many binary systems. Here the two possibilities of mixing are enthalpy of mixing is endothermic (heat absorbed) or exothermic (heat evolved). In the chemical model, the heat of mixing is attributed to bond energies between adjacent atoms. Three types of bonds exist in ordinary binary solid solutions: (a) A-A bonds with energy ε_{AA} and the number of these bonds present, P_{AA} ,(b) B-B bonds with energy ε_{BB} and the number of these bonds present, P_{BB}, and (c) A-B bonds with energy ε_{AB} and number of bonds, P_{AB}. The enthalpy of mixing is given by $\Delta H_{mix} = P_{AB}\varepsilon$ where $\varepsilon = \varepsilon_{AB} - \frac{1}{2}\left(\varepsilon_{AA} + \varepsilon_{BB}\right)$. Here again there are three possibilities. If ε is zero, the solution is ideal and the atoms are completely randomly arranged. If $\varepsilon < 0$, the atoms prefer to be surrounded by atoms of the opposite types (other element) and this increases P_{AB}. If $\varepsilon > 0$, each atom prefers to be surrounded by atoms of the same element and P_{AB} is minimized. In cases of ε closer to zero (such solutions are called regular solutions), the enthalpy of mixing is given by $\Delta H_{mix} = N_a z\varepsilon X_A X_B$ where N_a is Avagadro number and the Gibbs free energy is given by $\Delta G_{mixing} = N_a z\varepsilon X_A X_B + RT\left(X_A lnX_A + X_B lnX_B\right)$. When the enthalpy of mixing is negative, mixing results in free energy decrease at all temperatures. When the enthalpy of mixing is positive, the free energy can have positive or negative curvature depending on the temperature.

In reality, the arrangement of atoms in binary systems is a competition between lowest internal energy and entropy to achieve minimum free energy. In a system with $\varepsilon > 0$, the internal energy is reduced by increasing the number of A-A and B-B bonds forming a disordered alloy as shown in figure 2.1(a). In a system with $\varepsilon < 0$, the

internal energy is reduced by increasing the number of A-B bonds as shown in figure 2.1(b) and forming an ordered solid solution.

The Gibbs phase rule is typically applicable to bulk alloys. Here P + F = C + 2 where P is the number of phases, F is the degree of freedom and C is the number of components forming the alloy. At zero temperature, a positive enthalpy of mixing indicates that the homogeneous alloy is not stable and the material will separate into two phases. When the temperature is non zero the entropy of mixing lowers the Gibbs free energy following the equation $\Delta G_{mixing} = \Delta H_{mixing} - T\Delta S_{mixing}$. Hence miscibility is influenced by temperature and composition. If the enthalpy of mixing is negative, the homogeneous alloy is stable and entropy stabilizes the miscibility with temperature.

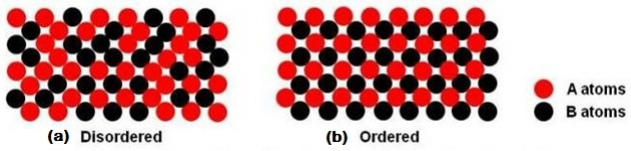

Figure 2.1. Atomic arrangement in disordered and ordered solid solutions.

There are many factors that play important roles in chemical ordering of atoms in alloys. One such factor is the atomic size of the elements which can introduce strain in the structure. If the difference between atom sizes is large, then the solution formed is an interstitial solid solution. In this case the big atoms form the cubic or hcp structure and the smaller atoms occupy the interstices between the bigger atoms. If the chemical bonds between the atoms are strong, then they form highly ordered intermetallic phases. In many cases, there are intermediate phases present in the alloy at different temperatures. Some other factors that affect the structure are valency and electronegativity. Intermediate phases typically undergo phase transformations to a more stable state at low temperature.

In ordered phases, the atoms are can have short range order or long range order. If long range order is present in an alloy, it can form substitutional, clustering or

interstitial solutions. For example, in Au-Cu alloy, at high temperature, the Cu and Au atoms are randomly arranged. At low temperature and 50/50 Cu/Au composition, the alloy takes an ordered structure with Cu and Au atoms arranged in alternate layers forming a super lattice. When the composition is Cu_3Au, another super lattice is possible as shown in figure 2.2 below [52].

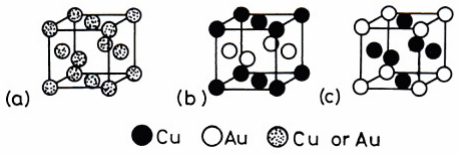

Figure 2.2. Au-Cu system having different ordering structures. (a)Disordered structure (b) Cu-Au superlattice (c) Cu3Au superlattice [52].

Some of the other common ordered lattices and their notations are given below. $L2_0$ in Cu-Zn system is shown in figure 2.3(a) where the corners of a cube are occupied by Cu atoms and the body center is occupied by a Zn atom. The other systems where this structure occurs are FeCo, NiAl, FeAl and AgMg. $L1_2$ is a structure in Cu-Au system shown also in figure 2.3 (b). It has Au atoms in the corners and the face centers occupied by Cu atoms. Other examples of this structure are Ni_3Mn, Ni_3Fe, Ni_3Al, Pt_3Fe etc. In $L1_0$ of Au-Cu, there are alternate layers of Au and Cu atoms. This structure is also present in CoPt and FePt. Some of the other structures listed in the figure 2.3 are $D0_3$(d) and $D0_{19}$(e) [53].

2.3 Thermodynamics at surfaces: Nano regime

One of the major reasons for the difference in the behavior of the nanoparticles and the bulk is the surface of the nanoparticles. The surface is the sharp boundary between the particle and the surrounding or between different phases. Surface energy plays an important role in the thermodynamics of the nanoparticles. The surface energy influences the free energy as $G = U - TS + \gamma A$, where γ is the surface

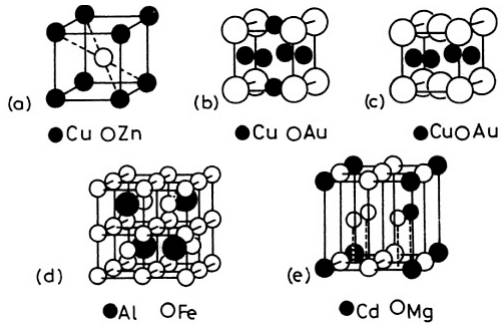

Figure 2.3. Five common ordered lattices [52]. (a)$L2_0$ in Cu-Zn (b)$L1_2$ in Cu-Au (c)$L1_0$ of Au-Cu (d)$D0_3$ in Al-Fe (e)$D0_{19}$ in Cd-Mg.

tension and A is the area of the nanomaterial. To increase the surface area of the solid under equilibrium conditions of pressure and temperature, the reversible work done is given by $\delta W = \gamma dA$, where γ is the surface tension. The change in Gibbs free energy G is given by $dG = -SdT + VdP + \gamma dA$ where S, T, P and V are the entropy, temperature, pressure and volume respectively. In nanoparticles, the number of atoms on the surface is comparable to the number of atoms in the volume of the nanoparticles. The surface to volume ratio varies inversely with the diameter of the particle or cluster. This has direct impact on surface related properties. Surface energy can be explained by assuming the nanomaterials are obtained by breaking up from a larger piece of material. The resulting surface of the nanomaterials has broken bonds contributing to surface energy. The surface energy also changes depending on the terminating ions or surfaces. Dissimilar crystallographic planes have different surface energies. A facetted particle presents specific crystallographic planes that minimize surface energy.

Surface energy per mole is given by $U_{surface} = \frac{6M\gamma}{\rho D}$ and the hydrostatic pressure is dependent on size as $P = \frac{4\sigma}{D}$ [54]. Here D is the particle diameter, M is the molecular weight, ρ is the density of the materials. It is important to note that the surface energy per mole is inversely proportional to the size of the particles. This influences physical properties of the material such as stress and strain in the system. Another example of

the influence of the surface energy is when particles coagulate during synthesis. The difference in the surface energies of the original particles and the coagulated particles leads to energy dissipation and to an increase in temperature. This temperature increase is inversely proportional to the size of the particles. Coagulation is related to sintering or grain growth of particles as well and will be discussed further in section 2.4.1.

Grain growth leads to reduction in surface area and surface energy. With the initial size of the particle d and final size d_{final} after grain growth, the reduction in surface energy is inversely related to the size of the particle [54]:

$$\Delta U_{surface} = \frac{M6\gamma}{\rho d_{final}} \left(\frac{d_{final}}{d} - 1 \right)$$

During phase transformations, the enthalpy changes with size as shown in [54],

$$\Delta H_{trans-nano} = \Delta H_{trans} - \frac{6M\gamma_{new}}{\rho_{new} d_{new}} \left[1 - \left(\frac{\gamma_{old}}{\gamma_{new}} \right) \left(\frac{\rho_{new}}{\rho_{old}} \right)^{\frac{2}{3}} \right]$$

This represents the inverse linear relationship between the change in enthalpy and the particle size. The Clausius-Clapeyron equation shows that the vapor pressure varies with surface energy and particle size as $P = P_{\infty} exp\left(\frac{4\gamma V_m}{DRT}\right)$ where P_{∞} is the vapor pressure on flat plane, V_m is the molar volume, R is the gas constant and T is the temperature. So the vapour pressure increases drastically with the decrease in particle diameter. In gas phase synthesis, it is easier to synthesize small particles of materials with low vapor pressure. This influences the shape of the particles as well.

Samorjai et al. [55] defined the chemical potential of an ideal solution for binary systems as $\mu_i^b = \mu_i^{0,b} + RTlnx_i^b$ where i=1,2, μ_i^b is the chemical potential of bulk solution and x_i^b is the mole fraction of i^{th} component. The main cause of surface segregation is the binding energy which affects the chemical bonding and surface tension. For metals, there is a strong relation between surface tension and heat of sublimation. Surface composition is strongly dependent on the surface tension of the components, heat of mixing, and temperature.

Some examples of surface effects are islanding, surface roughness, texturing and faceting. Microstructure, atomic mobility and mechanical strength varies with crys-

tal structure, grain structure, defects and compositional variations. An exhaustive review of the different thermodynamical quantities that change dramatically in the nanoscales is beyond the scope of this thesis. Next we discuss key properties like melting, morphologies and ordering in nanoparticles, not seen in bulk.

2.3.1 Melting

Many studies have been devoted to the effect of size and composition on the melting temperature of monometallic nanoparticles. The nanoparticles are known to have melting temperature much lower than that of the bulk. Melting, nucleation and sintering mechanisms of metallic nanoparticles are still not completely understood. Surface melting manifests as sharp variations in structural and thermodynamic parameters across the diameter of the nanoparticles. Computer simulations have shown that nanoalloys undergo structural transformations such as recrystallization, before they undergo melting. Nucleation can be homogeneous (throughout the medium of the nanoparticles) or heterogeneous (preferential at the interfaces or defects). Crystallization involves the formation of solid nanoparticles precipitating from solutions or melts. Recrystallization follows melting where crystals form via chemical solid-liquid separation, and mass transfer from liquid solution to a pure solid crystalline phase occurs.

Buffat and Borel [56] first experimentally confirmed the depression of melting temperature in gold nanoparticles. Since the interface and surface energies play a major role in nanoparticles, the overall morphology and geometry of the nanoparticles should be considered. The melting of nanoparticles is affected by the compositions of the nanoalloy. From classical thermodynamics, it was found $\frac{T_m}{T_0} = 1 - \frac{2}{\rho_s L r_s}\left[\gamma_s - \gamma_l \left(\frac{\rho_s}{\rho_l}\right)^{\frac{2}{3}}\right]$ where r_s is the radius of the solid [12, 56]. Here T_m = melting temperature, T_0 = temperature of triple point of bulk phase, ρ_s, ρ_l = densities of solid and liquid phases, L= latent heat of fusion, and γ_s, γ_l = surface tension

in solid and liquid phases. The finite-size of the nanoalloy particles can also affect other phase transition temperatures.

Surface melting is strongly prevalent in nanomaterials [57]. Since the atoms on the surface are less coordinated, the surface melts at lower temperature compared to the volume melting temperature. Surface induced disorder is also seen in many alloys. This happens when a layer of disordered phase wets the surface close to the melting temperature and this is pre-melting [58]. For example, Mei and Lu concluded that the (110) surfaces of Al, Cu and Ni show surface pre-melting. The (100) surfaces of Pb, Ni and Au undergo incomplete surface melting especially when they have packing density between (110) and (111).

Miao et al. [59] monitored the melting of Pd clusters and nanowires using Sutton-Chen potential in a molecular dynamics study. They found the nanoclusters have lower melting temperature compared to that of the nanowire. Surface pre-melting at much lower temperature was observed. Lui et al. [60] found there were three time periods before the complete melting of the gold nanoparticles takes place. The three processes and the associated three time scales correspond to disordering, reordering and surface melting. They also studied the melting of differently shaped nanoparticles. Icosahedra have the lowest melting temperature and star-like decahedra have higher melting temperatures. They studied the pair-correlation function and mean square displacement for understanding the melting of different clusters.

Delogu [61] investigated the melting of $AuCu_3$ clusters of sizes 1-10nm with the second moment approximation-tight binding (SMA-TB) approach and found that the disordering process starts at the surface, and Au segregates with a concentration gradient between the surface and bulk. Chen et al. [62] modeled the melting of 55 atom Ag-Au nanoalloys using Gupta potential. They found the melting temperature to decrease with increasing Au content. This implies that the melting behavior is dependent not only on the size but composition as well. Here Au has higher melting temperature than Ag. Sankaranarayanan et al. [63] simulated the melting of Pd-Pt

core-shell clusters and found that melting happens in two stages in this system. The external Pd shell undergoes surface melting followed by melting of the Pt core.

2.3.2 Chemical ordering and segregation in nanoparticles

Chemical ordering refers to the arrangement of the metal atoms in alloy nanoparticles. When metals A and B mix to form an alloy, the chemical ordering in the alloy has many possibilities as described in section 2.2. The nanoparticle can have a disordered mixed structure, ordered mixed pattern, segregated pattern, core-shell segregated pattern , or multi-shell pattern as shown in figure 1.1. Mixed alloys can be either random or ordered as in the case of $L1_0$ geometry of AuCu and AuAg alloys [1, 64]. Segregated motifs manifest themselves as core/shell where core is of metal A and shell of metal B or multi-shell A-B-A as in Pd-Au nanoparticles [65], or as A-B-A-B in Pd-Pt nanoparticles [66]. Chemical ordering is affected by size, surface energies and strength of homonuclear and heteronuclear bonds of the constituting elements in an alloy. When alloying, new structural motifs can be created and the chemical properties can be tuned as a function of compositions of the metals present and the degree of atomic mixing of the two metals.

Monte Carlo method and Molecular dynamics (MD) have been used in canonical or semi-grand canonical ensemble to study nanoalloys. Quenched MD is used to determine the ground state structures at 0K. The Hamiltonians used to model the alloy systems require semi-emperical potential to explore the energy landscape. Density functional theory (DFT) methods are used either for fitting the semi-emperical potentials or to determine more accurately the lower energy structure of different isomers. To find stable structures in a cluster configuration, one needs to find a global minimum of the potential energy surface generated by interaction models. The energy landscapes are generated by density functional theory calculations and the equilibrium properties of the nanoalloys are predicted by Molecular Dynamics or Monte Carlo simulations. With a wide spectrum of sizes, compositions and structure, it is a

challenge to predict the equilibrium configuration. Finite temperature properties are averages calculated from sampling the energy landscape over different configurations. A major aspect of the theoretical studies involves the choice of the energetic models with appropriate potentials that mimic the metallic systems behavior. It involves methods to calculate the total energy of the nanoclusters, to calculate the physical properties and quantities that match experimental evidence. It also launches a search on favored structure for certain size ranges either by geometry or by quantum effects. The energetics, thermodynamics, and kinetics of the nanoclusters give the complete picture of the evolution of the nanoparticles.

Andreazza et al [67] probed the CoPt nanoclusters in a temperature range of 300-900 K for different non periodic structures at equal concentration. They found the existence of bi-stability in 3.5nm sized CoPt alloy nanoparticles at 900 K, where the ordered and disordered nanocrystal co-exist. It is important to understand surface phase diagrams of alloys to explain the ordering mechanisms in nanoparticles or clusters.

Barcaro [68] has shown that in the case of few platinum impurities within Pd-rich clusters, the Pt atoms tend to populate the (111) surfaces and this tendency increases with size of the clusters. Particularly in the composition range around 1:1, PdPt forms a multi-shell arrangement where the subsurface shells have reversed chemical ordering compared to the surface shell with the Pd atoms occupying the central positions of the (111) facets and Pt occupies the (100) facets and edges. This leads to a patchwork of islands of atoms of the two elements [68]. Core shell arrangement can also be expected in case of mixing two species with different cohesion in the bulk and in cases when the size mismatch is small. The more cohesive element will achieve full coordination and form a close packed core. The less cohesive element will have low coordination and is surface segregated with non-crystalline fivefold arrangement. This is seen in the case of Pd-Pt where the Pd forms a decahedral structure on top and the Pt atoms form the core with double tetrahedron [69].

Mariscal et al. [70] monitored the coalescence by collision of different pairs of clusters of Au-Pt, Au-Pd and Cu-Ag with Embedded Atom method (EAM) potentials. Au-Pt coalescence formed the core and Au shell structures. In Au-Pd collision, coalescence lead to intermixed clusters. In Cu-Ag collisions, three shell onion-like structures were formed. Pt being more cohesive than Au, it remains as a core in case of Au-Pt. In Pd-Au, the difference in cohesive energy between the two metals is small and with the negative heat of mixing, it leads to an intermixed cluster.

Simulations of chemical ordering

In this section, we briefly introduce the model used to study chemical ordering in noble metals and their alloys for applications as fuel cell catalysts. In the crystalline state, each atom can be referred to a specific lattice site n, the actual position being given by $\overrightarrow{R_n} = \overrightarrow{n} + \overrightarrow{u_n}$ where $\overrightarrow{u_n}$ is the atomic displacement. Initially the lattice has only atom A, and then atom B is added as impurity to form an alloy. For binary alloys, each site has two degrees of freedom and it is denoted by the occupation number $p_n = 0$ or 1 depending on whether atom A or B is at the site n with displacement $\overrightarrow{u_n}$. This formulation can be extrapolated for a multi-component alloy with p_n^i,i = A, B, C... and so on. In binary systems, the chemical and displacement effects are coupled. We assume the energy to be a function of the configuration, $H(p_n, u_n)$, where the partition function is given by $Z = \sum_{p_n,u_n} \exp\left(-\frac{H}{k_B T}\right)$ and the free energy is given by $F(V,T,N^i) = -K_B T lnZ$ where V is the volume and N^i is the number of atoms of type i. The variation in the free energy is given by $dF = PdV - SdT + \sum_i \mu^i dN^i$ where S is the entropy. For an binary alloys with constant number of atoms $N = \sum_i N^i$ and $N^B = Nc, N^A = N(1-c)$ where c is the concentration of the B atoms, the free energy change is $dF(T,c) = -SdT + \left(\mu^A - \mu^B\right) Ndc = -SdT + \mu N dc$ where $\mu = \mu^A - \mu^B$.

For noble metals, a many-body potential like the second moment approximation (SMA) derived from the electronic structure in the framework of tight binding

approximation can be chosen. The model combines the tight-binding Ising model (TBIM) on a rigid lattice and the SMA, taking into account essentially the difference in the bandwidth of the two constituents but permitting lattice relaxation. TBIM describes in a realistic way surface segregation and ordering phenomena at bimetallic surfaces [69, 70] and nanoalloys [4, 71–75]. For an alloy $A_{(1-c)}B_c$, the Hamiltonian is given by:

$$H^{eff} = \sum_n p_n \left(\Delta h_n^{eff} - \sum_{m \neq n} V_{nm} \right) + \sum_{n,m \neq n} p_n p_m V_{nm}$$

Where p_n is the occupation number equal to 1 or 0, depending on whether the site n is occupied or not by an atom of type A. For a binary alloy $A_{(1-c)}B_c$, $p_n = 0$ means the site n is occupied by an atom of type B. The alloy effective pair interaction is $V_{nm} = 1/2 \left(V_{nm}^{AA} + V_{nm}^{BB} - 2V_{nm}^{AB} \right)$ between the atoms at sites n and m characterizing the tendency to bulk ordering ($V > 0$) or to phase separation ($V < 0$). Here V_{AA}, V_{BB} and V_{AB} are homo and hetero atomic pair interactions. The local surface field Δh_0^{eff} is identical to the difference in surface energies between the pure constituents A and B ($h_0^{eff} = \gamma^A - \gamma^B$) and $\Delta h_p^{eff} = 0$ if $p \neq 0$. These models are similar to the Ising model used for modeling magnetic materials where the control parameter is the magnetic field. In the case of alloys, the control parameter is the concentration.

$$H\left(\{\sigma_n\}\right) = -\frac{1}{2} \sum_{n,m} J_{nm} \sigma_n \sigma_m - h \sum_n \sigma_n$$

with $J_{nm} = \frac{-V_{nm}}{4}$ The degree of mixing in an alloy $A_m B_n$ is influenced by [1]: (a) The relative strength of the homonuclear bonds (A-A, B-B) and heteronuclear bond (A-B). If A-B bonds are stronger, then mixing happens. If not, segregation happens with the strongest homonuclear bond forming the core. (b) The surface energies of A and B play a major role. The element with lower surface energy will form the shell. (c) The relative atomic sizes of the elements. (d) The relative electronegativity of the elements. (e) The surface ligands and support also plays a role in the mixing of the nanoalloy. For a detailed treatment of the models, the reader is directed to the textbook by Alloyeau [4].

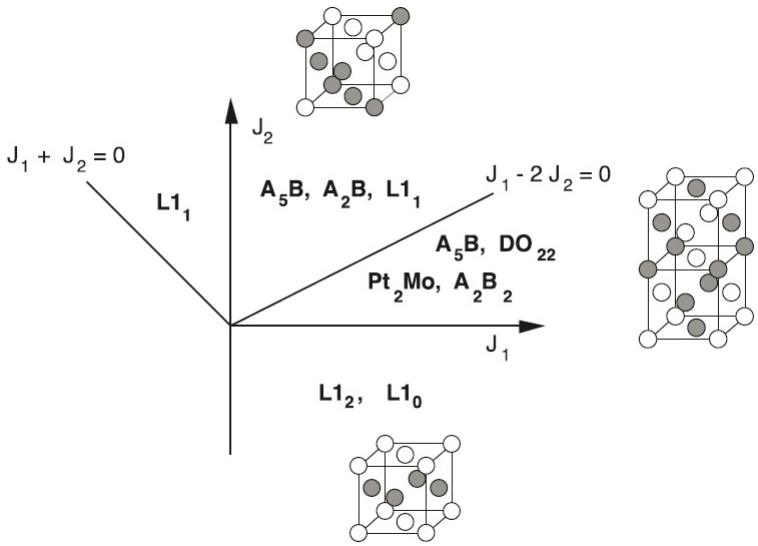

Figure 2.4. Structure predicted by SMA-TB model for alloy AB. [4]

In this formulation, the ground state of the FCC lattice can take different structures depending on first and second neighbor interactions at $c = \frac{1}{2}$ as shown in figure 2.4. Depending on the concentration of A and B, the figure shows different structural possibilities. In simple cases, the phases are of the simple FCC or BCC structure. Some of the ordered structures seen in binary alloys are shown in figure 2.2 and figure 2.3. As we have seen before, the $L1_0$ has alternate layers of atoms of different elements. $L1_2$ is a structure where the corners are atoms of one element and the face centers are occupied by atoms of another element (Cu_3Au).

Phase diagram

The phase diagram is a plot of the concentration versus the temperature indicating stability ranges of various structures. In bulk, we have two different situations depending on the interaction between the atoms of the elements forming a binary alloy. We can have mixing (alloying) or phase segregation. In the case of alloying there are regions of the phase diagram where ordered and disordered phases coexist. The concentration is the order parameter used in understanding the thermodynamics

of alloys. Order-disorder transitions in a crystal structure are parameterized by the loss of symmetry. The phase transition temperature is an important parameter to monitor. There can be two types of transitions: first order transitions (exhibit a discontinuity in the first derivative of the free energy with respect to some thermodynamic variable), and the second order transitions (exhibit a discontinuity in the second derivative of the free energy with respect to some thermodynamic variable).

In the particular case of the first order transition of $L1_2$ to disordered A1 fcc, normally seen in binary A_3B alloys like Cu_3Pd, Cu_3Au and Co_3Pt, the symmetry lost is the translational symmetry. The structure is reported to exhibit three structural variants separated by anti-phase boundaries. Anti-phase boundaries (APB) are planar defects that affect the physical properties of materials. The behavior of APB close to the transition temperature depends on the order of the transition. The local width of the APB is the direct measure of the correlation length used in the mean field theory to study the phase transitions in alloys.

Ricolleau et al. [72] examined a first order transition in Cu-Pd (17%) by monitoring the domain wall thickness as a function of temperature. In the vicinity of the Tc, three types of anti-phase boundaries appeared in their dark-field transmission electron microscopy images. At low temperature, the domain walls are sharp and the boundary extends over a few atomic planes becoming partially disordered. The disordered layer increases with temperature with the disordered phase emerging at transition temperature Tc with two new order-disorder interfaces. They identified the APB wetting regime and two-phase regime. APB width is the order parameter that was found to have a logarithmic dependence on temperature.

At higher temperature Fe-Al has disordered bcc structure which transforms into an ordered B2 (CsCl-like structure) phase. Second order transitions are rare in alloys but they were found to happen in Fe-Al alloys. Another phase transformation happens at lower temperature when the B2 phase changes to DO_3 phase. Le Floch et al. [73] monitored the contrast and intensity of the APB in their combined weak-beam and

conventional dark-field transmission electron microscopy images. APB broaden and vanish close to Tc.

2.3.3 Nanoparticle shape

The shape of nanoparticles is important as it dictates not only the geometry but also the number of atoms forming the clusters. Multi-scale computational studies can model nanoparticles and study the evolution of properties as a function of total number of atoms (or molecular units) in the system. A variety of polymorphic crystal structures exist in the nanoparticles and a combination of experiments and simulations can provide insights into structure-property relationships. The binding energy of a cluster of size N can be written as [1] : $E_b = aN + bN^{\frac{2}{3}} + cN^{\frac{1}{3}} + d$ where the first term is the volume contribution followed by the surface contribution and the rest of the terms come from energy of facets, edges and vertices. From the geometrical point of view, most metals have a face centered cubic (fcc) crystalline structure. Face centered cubic clusters can have octahedron, truncated octrahedron and cuboctahedron shapes. Octahedrons are made of two square pyramids sharing a base and have high surface/volume ratio. Cutting off the vertices from the octahedron generates a truncated octahedron, having eight closed packed (111) and six square (100) facets. Examples of a non-crystalline structure are the icosahedrons (Ih) and the decahedron (Dh). The icosahedron has only (111) close packed facets. The decahedron is formed by two pentagonal pyramids with shared base. The Icosahedral motif is favored at small sizes (<2nm), the truncated octahedron clusters are favored for larger sizes (>5nm), and the decahedra are favored for intermediate size ranges.

Density functional theory calculations have shown that gold nanoparticles can take any of the stable structures shown in figure 2.5(a) [74]. The numbers in the subscripts are the numbers of atoms forming the nanoparticles. Nanoparticles ($\approx 5nm$) having 146 to 318 atoms are found to have icosahedral or truncated octahedral structures. These structural motifs sample a very small part of the structure phase space.

The icosahedral and decahedral structures become less stable with more atoms due to accumulated strain energy. The phase diagrams for the nanoscale materials have axes with number of atoms N and average diameter D apart from temperature, compositions, and pressure. A phase map as shown in figure 2.5(b)includes the structural motif and shapes with the phase diagram.

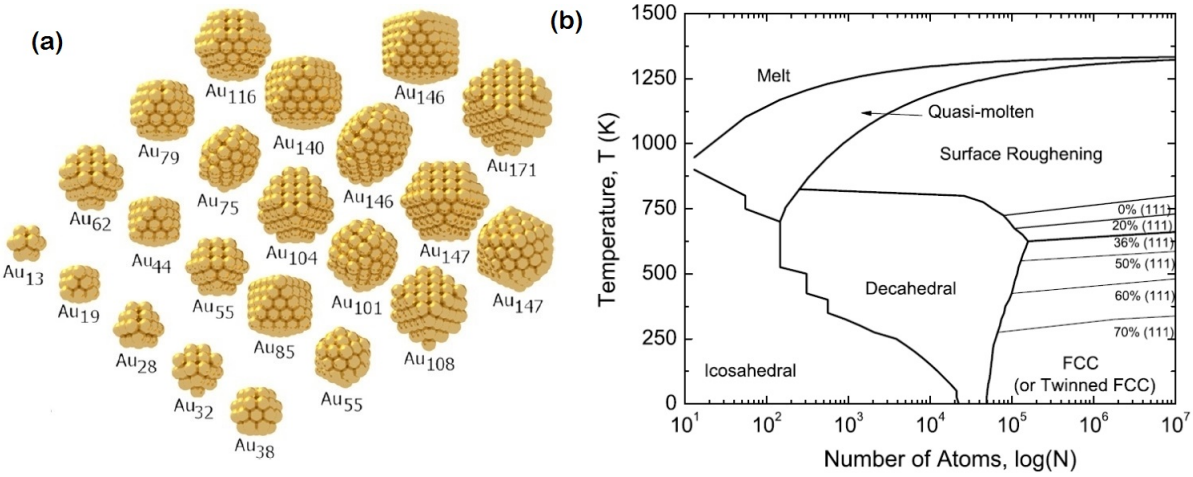

Figure 2.5. (a) Different shapes and sizes of Gold nanoparticles (b) Phase map of gold nanoparticles predicted by simulations [74].

Theoretical studies have explored the concept of magic number in some detail. Magic metal clusters are characterized by structural and electronic shell closure. The structural shell closure corresponds to particles consisting of a number of atoms that enables high symmetry like the icosahedral, decahedral and octahedral motifs by Mackay Constructions [13]. The size of the most energetically favored structure is called the magic size. The electronic shell closure corresponds to the case when the electrons of the clusters completely fill the valence band separated from the conduction band by an energy gap of 1-2eV. It has been theoretically proven that these structural motifs have high energetic stability, and they enable a study of energy as a function of size. Also the magic number of the cluster enables building the whole cluster by

the symmetry operations of the point groups. These clusters have sizes in the range of 50 to 200 atoms [13].

Icosahedral structures have reduced surface energy and high internal stress. Theoretical studies suggest that in the case of two metals of different atomic sizes mixing and forming core-shell structure, they have great stability in an icoashedral structure [75]. Poly icosahedral structures are ubiquitous and exist in five fold and six fold symmetry. This is favoured in case of binary nanoalloys of sizes of few nanometers [76].

Computer simulations found that the minimum number of atoms constituting a stable gold cluster with the icosahedral structure is 147 while this number is 1300 atoms for the dodecahedral structure. The geometry crosses over from the dodecahedral structure to face centered cubic when 500 atoms forms a cluster [12]. Typically, the crystalline structures in bulk take the shape of octahedra or truncated octahedra. In the nanoscale, the materials takes the form of icosahedra, polytetrahedra and polyicosahedra, etc. These structures have efficient packing with inherent strain. There is also strain when there is size mismatch between the atomic species constituting the alloys.

Andreazza et al. [67] inspected the CoPt nanoclusters in a temperature range of 300-900 K for structures like truncated octahedron, icosahedrons and decahedron of different sizes at equal concentration. At temperature less than 600K, annealing induces coalescence in icosahedral clusters. At higher temperature, they undergo internal atom arrangement to form decahedron with transition to fcc structure. From their Monte-Carlo simulations with tight binding semi-empirical potentials, chemical ordering happens after transition to fcc structure and there is a structural transition from decahedron at small sizes to truncated octahedron in 2-2.5nm size range.

2.4 Kinetics in metallic nanoparticles

The kinetic phenomena relevant to this thesis are coalescence and grain growth, occurring during nanoparticles sintering, and the kinetics of mixing, ordering and phase segregation. Here we briefly discuss a few relevant examples involving noble metals nanoparticles.

2.4.1 Grain growth: coalescence and sintering

The study of the kinetics of phase growth is necessary to understand the mechanisms and estimate parameters relevant to grain growth. Sintering is important because it has been reported to have a deleterious effect on catalysis. Sintering has been studied extensively in powders. In this case, atoms diffuse across the boundaries of the grains, fusing the particles together. The models used to understand grain growth in nanoparticles fall into two regimes. First, at high temperature the cluster remains in liquid form during growth (melting) and the final cluster structure depends on kinetics of cooling after the growth process. Therefore, it is important to understand how the cluster solidifies if melting occurs during grain growth. Another phenomenon being explored is the coalescence of nanoclusters in the late stage of grain growth (recrystallization). Since nanomaterials have many size-dependent properties, it is important to find out how the nanoparticles change during grain growth. These processes involve diffusion of atoms in nanoparticles at challenging time and length scales.

Another interesting aspect of grain growth is the diffusion scaling law. We know the mean square diffusion path is $\bar{X}^2 \alpha D' t$. The mean square path is proportional to the size of the particles and the diffusion coefficient. The diffusion coefficient $D\prime$ is related to the activation energy Q and temperature, as $D' = D'_o \exp\left(-\frac{Q}{RT}\right)\big)$. The activation energy for diffusion in nanomaterials differs by many orders of magnitude from the bulk value.

MD is a standard tool to investigate the kinetics of grain growth. Typically, simulations involve particles made of more than 500 atoms and study the coalescence between two such nanoparticles. These studies compute the physical quantities like diffusion coefficient or surface tension, and explore how the nanoparticles evolve with time. The simulations need to be carried out at constant temperature which corresponds to the coalescence of supported nanoparticles with the substrate acting as heat bath. All properties are calculated using MD averages over all possible configurations weighted by the probability of their occurrences. This requires the MD simulations to be long enough so that sufficient representative configurations have been sampled. The MD software packages for these purposes are GROMACS and LAMMPS which are used to study large molecular systems.

Lewis et al. [77] carried out molecular simulation of coalescence of free gold clusters. A single cluster is formed by deformation of two constituent clusters with the reduction of the surface area, followed by diffusion. The coalescence of a solid and liquid cluster occurs in two stages. In the first stage, the contact surface increases and is faceted. In the second stage, the object evolves from a non-spherical particle to a sphere. The spherical shape is reached by diffusion. The time scale for sintering was found to differ from the macroscopic bulk sintering time scales predicted by earlier models [78].

One of the earliest phenomenological theories proposed by Frenkel [79] suggested that the crystalline bodies undergo diffusion under the influence of surface tension. The work done by surface tension was equated to energy dissipation due to viscous flow and the time required for the final grain to become round was found to be proportional to the initial size of the grain and inversely proportional to the surface tension. This viscous law model was further developed by Hawa and Zachariah [80] to visualize sintering of nanoparticles. Their calculation showed that sintering happens in three basic steps as indicated in Figure 2.6. The particles come together to minimize surface area, forming a cylinder, followed by initial sintering at the ends and global contraction throughout the cylinder. Finally, the particle undergoes contraction to

Figure 2.6. Sintering mechanism proposed by Hawa and Zachariah [29].

become a sphere. These studies concentrate on the early stages of sintering where the particles form a neck region. Size dependent melting temperature was verified in their simulations. Also, they calculated the diffusion coefficient and activation energy for the diffusion mechanism involved in the system and compared them to available experimental data.

From the sintering of bulk materials [81–86] for metallurgical applications, different mechanisms that drive coalescence of two solid particles or clusters have different scaling laws correlating the size D (diameter), neck size x, and sintering time t as summarized in Table 2.1. Here η is the viscosity of materials, γ = Surface energy, b = Burgers vector, T = absolute temperature, ρ = theoretical density, δ = grain boundary width, D_v = volume diffusivity, D_s = surface diffusivity, D_b = grain boundary diffusivity and Ω = atomic volume.

Sintering in nanoparticles is found to be faster and the sintering kinetics are different compared to larger micron-sized particles. Herrings law and other analytical models [82] cannot be extrapolated to predict the relationship between particle size and sintering temperature [87]. Herring scaling law states that when powders with similar shapes but different sizes are sintered under the same experimental conditions

Table 2.1.
Scaling laws relating the neck size and diffusion coefficient [81–86]

Type of Diffusion	Neck size dependence on time
Viscous flow	$\left(\frac{x}{D}\right)^2 = \frac{3\gamma t}{2\eta D}$
Plastic flow	$\left(\frac{x}{D}\right)^2 = \frac{9\pi\gamma b D_v t}{k_B T D}$
Volume diffusion	$\left(\frac{x}{D}\right)^5 = \frac{80\gamma\Omega D_v t}{k_B T D^3}$
Grain boundary diffusion	$\left(\frac{x}{D}\right)^6 = \frac{20\gamma\Omega D_b \delta t}{k_B T D^4}$
Surface diffusion	$\left(\frac{x}{D}\right)^7 = \frac{56\gamma D_s \delta t \Omega^{\frac{4}{3}}}{k_B T D^4}$
Lattice diffusion	$\left(\frac{x}{D}\right)^4 = \frac{16\gamma_s D_l t\Omega}{k_B T D^4}$

and by the same sintering mechanism, the scaling law predicts the relative periods of sintering time required to get the same degree of sintering [82]. For sintering of two kinds of powders with radii a_1 and a_2 where $a_2 = \mu a_1$, the required sintering time t_2 and time t_1 are related as $t_2 = \mu^\alpha t_1$ where α is an exponent that varies with the sintering mechanism involved. The differences from the bulk could be due to different structure/phase with different defect structures and different diffusion behavior. Several works compared the sintering process of nanoparticles both experimentally and theoretically and found good agreement with the neck theory [87]. Xing and Rosner [88] proposed coalescence occurs by surface diffusion and found their simulation results were consistent with experimental results of alumina and titania nanoparticles. Zhu and Averback [89] evaluated the diffusion coefficient for sintering copper nanoparticles and found their grain boundary diffusion coefficient was three orders of magnitude larger than the experimental values.

MD simulation by Arcidiacono et al. [90] predicted diverse mechanisms at the initial stages of coalescence with neck formation. Their results showed that for nanoparticles of sizes $> 2nm$ in diameter, grain-boundary diffusion dominates and agrees with phenomenological models. For smaller nanoparticles, surface diffusion and grain boundary diffusion compete. They also found that the relative rotation of the parti-

cles may provide another route for elimination of the boundary during coalescence. Grochela et al. [91] have examined the shapes of gold nanoparticles before and after sintering. Their study concluded that in early stage coalescence, decahedral and fcc (truncated octahedral and cuboctahedral) morphologies occur. Kuo et al. [92] investigated melting of supported and unsupported gold nanoparticles. For unsupported nanoparticles of 2-5nm, a structural transformation to an icosahedral structure at high temperatures was observed and is followed by a quasi-molten state. When the particles are supported on silica substrate, they changed structure at higher temperature and were deformed due to stress arising from the gold/silica interface.

2.4.2 Kinetics of mixing

The mixing process and formation of equilibrium structure is expected to be faster in multimetallic nanoalloys compared to the bulk materials. This phenomenon is interesting and is present in alloying, melting and grain growth of nanoparticles.

Yasuda and co workers [93] investigated the mixing of copper atoms in gold clusters with *in situ* TEM. At room temperature they observed spontaneous mixing forming a solid solution and the diffusion coefficient of Cu was 9 orders of magnitude larger than that for Cu dissolution in bulk Au. At lower temperature, the mixing leads to a Au core surrounded by Cu-Au solid solution. The solid solution was also found at temperatures below the bulk order-disorder transition temperature. For clusters of 10nm, dissolution occurs only on the surface. For larger clusters of 30nm, there was no dissolution. Shimizu et al. [94] used Morse-like pair potential to study the same system and found negative heat of mixing aids the complete mixing process and it occurs in solid phase. They also confirmed the low temperature surface melting in the Au-Cu system.

Shimizu and co-workers [95] examined the mixing in 4d metallic nanoalloys (Ru-Mo, Mo-Nb and Mo-Zr) using SMA-TB type model potential. Rapid mixing was predicted for systems with negative heat of mixing and this was valid for all compo-

sitions. For systems with small positive heat of mixing, atomic convection leading to dopant atoms (lower content) diffusing into the core was found.

In this chapter we briefly discussed the various phenomena/structural transformations of metal nanoparticles with theoretical and experimental examples from recent literature. Starting from the basic thermodynamical relations, melting, phase transformations, alloying and chemical ordering were discussed. In the next two chapters, our experiments pertaining to grain growth of trimetallic PtNiCo nanoparticles and transformations in Pd-Cu nanoparticle mixtures are presented in detail.

3. EXPERIMENTAL TECHNIQUES

In this chapter we discuss the experimental techniques used in this thesis for the study of the structural transformations in multi-metallic nanoparticles. We start with the synthesis of the nanoparticles along with the sample preparation for various experiments. The main techniques employed, x-ray diffraction and transmission electron microscopy, are discussed with examples of data and their analysis. Other techniques used in this study are briefly described.

3.1 Synthesis of nanoparticles

The nanoparticles can take various sizes and shapes such as triangles, cubes, stars, flowers etc. In this study, we used spherical monodisperse nanoparticles of Pd, Cu, Au and alloys such as PtNiCo, PtIrCo. We studied the alloying in physical mixtures consisting of two different monometallic nanoparticles and the evolution of already alloyed nanoparticles in case of the grain-growth experiments. The nanoparticles can be synthesized by methods requiring ultra-high vacuum like pulsed laser deposition, atomic layer deposition, etc. The major challenges for these techniques are agglomeration of the nanoparticles and broad distribution of the nanoparticles size. On the other hand, wet chemical synthesis methods produce encapsulated nanoparticles. The organic capping agents are necessary to protect the monodispersity of the nanoparticles and prevent the particles from coalescence. For this study, the nanoparticles are synthesized by wet chemical synthesis method. Other wet chemistry methods include co-precipitation, incipient wetness impregnation, successive reduction and thermal decomposition methods.

The wet chemical synthesis method was developed by Brust et al. [96, 97] for the synthesis of gold nanoparticles. Hydrogen tetra-chloroaurate (III) hydrate (HAuCl4),

the metal precursor is mixed with tetra octyl ammonium bromide (TOABr) in toluene. TOABr is a phase transfer reagent and in this reaction it is used to transfer the product formed from aqueous phase to organic phase. The aqueous phase is then removed and thiol is added. TOABr is replaced by thiol which stabilizes the metal pre-cursor. Then sodium borohydride (NaBH4) is added to reduce the metal precursor and form the nanoparticles with thiol cap. The end product consists of small nanoparticles (usually of size less than 2nm) with alkanethiol caps. The nanoparticles are stable and have a shelf life of a few weeks.

3.1.1 Supporting nanoparticles for different experiments

The main techniques used to study the nanoparticles are x-ray diffraction, transmission electron microscopy, x-ray photoelectron spectroscopy and atomic force microscopy. Using synchrotron-based x-ray diffraction, we can examine the behavior of nanoparticles and study the ensemble-averaged processes like grain growth and phase transformations. With electron microscopy, we probe the evolution of the atomic structure of individual nanoparticles. This combination of techniques offers great advantages for understanding the nanoparticles from the structural point of view. To characterize the structural evolution of the nanoparticle samples with thermal treatment, we used various experimental techniques requiring different sample preparations. This section briefly describes the sample preparation done for each of the characterization techniques.

For x-ray diffraction, the as-prepared nanoparticles were dispensed on Si substrates that had a 0.5um thick SiO2 oxide film on them. Initially the substrates were cleaned with acetone and dried using nitrogen gas to get a dust-free surface. Then the nanoparticles were drop cast using micro-liter disposable syringes. These samples were air dried in a high efficiency particulate air (HEPA) hood. Some samples were also annealed at $200°C$ on a hot plate for ten minutes to prevent the organic capping agents from interfering with the structural evolution of the metallic nanoparticles [98].

The samples were then annealed in a vacuum chamber as described in the section on synchrotron based x-ray diffraction. We also studied the evolution of the nanoparticles on other substrates such as carbon, alumina, glass etc. For these experiments, the nanoparticles were first dispersed on these substrates and then mounted on the regular flat SiO2/Si substrate.

For TEM experiments, several different types of grids were used. The Cu grids were 3mm in diameter with thin carbon support film and were obtained from Ted Pella, Inc. The annealed nanoparticles on Si substrates (used for XRD experiments) were removed with hexane, and then were dispensed on Cu grids. The grids were air dried to let the hexane evaporate. In most cases, the evaporation was not complete and often led to dark circles or carbon contamination being formed when the samples were imaged with the electron beam. So to prevent this issue, the grids with the samples were plasma cleaned to remove additional carbonaceous matter and hexane. Plasma cleaning was carried out on Fischione Instrument model 1020 with flowing Argon containing 2.17% of oxygen for 15-20 seconds. It was very important to remove the carbon content in the sample as it provided a dark background around nanoparticles, often preventing good contrast in the images. These samples were used for high resolution transmission electron microscopy, electron energy loss spectroscopy and energy filtered transmission electron microscopy. Using energy dispersive x-ray spectroscopy (EDX) experiments, the elemental content and distribution of the element in the nanoparticles were studied. While mapping Cu on the Pd-Cu nanoparticles dispensed on Cu grids, the maps were saturated with signal from the Cu grid and were not useful. So for EDX experiments, the samples were dispensed on Molybdenum or gold coated grids with holey C film on them. The Mo grids were obtained from Pacific GridTech and Au coated grids were obtained from Ted Pella, Inc.

For AFM and XPS measurements, the samples on the Si substrates were the same as used in XRD experiments. The techniques used to monitor the structural evolution of the nanoparticles with thermal treatment are briefly discussed in the next few sec-

tions. These sections summarily explain the motivation, basic physics involved in the technique and data analysis involved. Next, we discuss x-ray diffraction techniques.

3.2 X-ray powder diffraction

X-ray diffraction (XRD) is a nondestructive method used to determine the crystallinity and phase properties of bi and tri-metallic nanoparticles. The main components of a XRD instrument are the x-ray source, goniometer to position the sample and move to desired angles and detector to measure the intensity of the x-ray scattered by the specimen. The diffractogram consists of plots of diffracted intensity as a function of scattering angle or the scattering vector. XRD can be obtained for single crystal or poly crystalline material but an amorphous material will not produce peaks as the x-ray beam is not scattered coherently. For diffraction to take place, the wavelength of the beam needs to be similar to the atomic layer spacing in the sample and the material needs to be crystalline.

Suppose two coherent beams scatter on two different planes of atoms in the lattice of the material as shown in figure 3.1. The crystal structure has translational symmetry and the atoms are arranged with a lattice spacing d. For the scattered x-rays from the planes of the lattice to interfere constructively, the path difference between the two scattered beams has to be an integral multiple of the wavelength of the x-rays. This is Braggs crystallographic equation.

$$n\lambda = 2d\sin\theta \tag{3.1}$$

Braggs equation (3.1)can be used to estimate the lattice spacing d of the structure if one knows the wavelength of the x-ray (λ) and the angle of the detector (2θ). Here n is an integer. The lattice spacing can be used to calculate the lattice parameter with the numerical factor corresponding to the lattice plane. Other information such as grain size, film thickness, mosaicity and lattice distortion can be obtained from the shapes, widths and intensities of the diffraction peaks. Depending on the crystal symmetries, different structures exhibit different diffraction peaks. Using the struc-

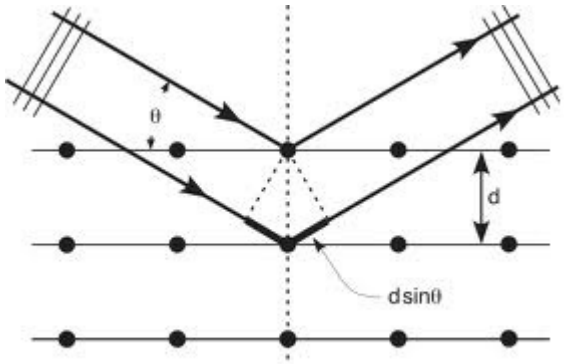

Figure 3.1. X-ray beams striking on the atoms of a lattice.

ture factor calculations, one can predict the reflections that are forbidden and those that will appear in the diffractogram. For detailed descriptions of the structure factor calculations, the reader is directed to solid state physics textbooks [99]. The structure factor related to our XRD measurements is described in the next section.

The potential of multifunctional materials like catalysts is dependent on the ability to control shape, size and ordering of nanoparticles. This requires controlling growth of large collections of nanoparticles by monitoring the relevant parameters *in situ* and in real time. Powder diffraction with *in situ* temperature and pressure capabilities is ideal for studying structural transformations during chemical reactions as in catalysis in electrochemical cells. In this thesis, the phase transitions induced by thermal treatment in metal nanoparticles are examined.

3.2.1 Theory of x-ray diffraction

When an x-ray beam falls on an atom, two processes occur: (1) the beam may be absorbed with an ejection of an electron from the atom or (2) the beam may be scattered. The incident beam is an electromagnetic wave with electric field vector varying sinusoidally with time and position. The electric field is perpendicular to the direction of propagation of the beam. This electric field exerts a force on the

electron in the atom causing acceleration of the electrons. An accelerated charge radiates in all directions of the atom forming the scattered radiation that has the same frequency as the incident beam. The classical theory predicts the scattered intensity of the sample in electron units and the polarization of the scattered beam. There are two kinds of scattering: (a) unmodified scattering (same wavelength) and (b) Compton modified scattering (longer wavelength) [100]. Bragg reflections arise from the unmodified scattering from the crystal. The modified scattering occurs from different electrons and is incoherent. The sum of the intensities of the unmodified and modified scattering from each electron is equal to the classical intensity per electron. To calculate the classical scattered intensity, let us consider the single free electron

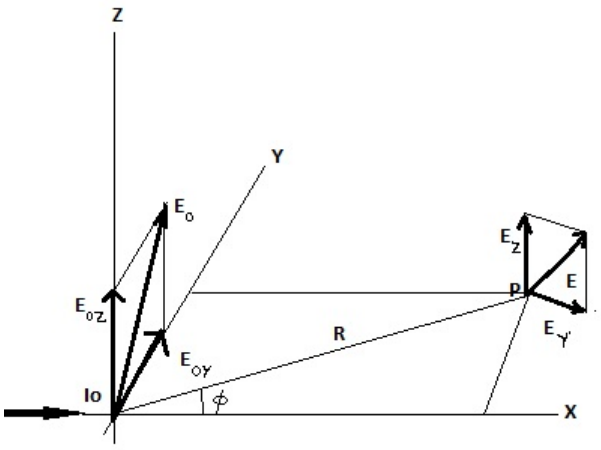

Figure 3.2. Classical scattering of x-ray beam [100].

at the origin of Figure 3.2 interacting with an unpolarized beam directed along the X-axis. We need to calculate the intensity of the scattered radiation at the point P (in the XY-plane) which is at the distance R from the electron and an angle ϕ with the x-axis. The incident beam is unpolarized, i.e the electric field vector takes all orientations in the YZ- plane with equal probability. The average electric field due to electron acceleration is given by

$$\langle E^2 \rangle = \langle E_0^2 \rangle \frac{e^4}{m^2 c^4 R^2} \left(\frac{1 + \cos^2 \phi}{2} \right) \tag{3.2}$$

The Intensity is related to the electric field in cgs units as $I = \frac{c}{8\pi}\langle E^2 \rangle$

$$I = I_0 \frac{e^4}{m^2 c^4 R^2} \left(\frac{1 + \cos^2 \phi}{2} \right) \tag{3.3}$$

Let us first discuss scattering by an atom. Consider the incident beam of amplitude E_0 polarized so that E_0 is normal to the plane of the paper as shown in figure 3.3. The monochromatic incident beam of intensity I_0 has a wavelength of λ falling on a crystal in the figure 3.3 shown below. Suppose the atom is at O. The electric field acting on an electron at $\overrightarrow{r_n}$ is $\epsilon_0 = E_0 \cos\left(2\pi\nu t - \frac{2\pi X_1}{\lambda}\right)$.The point of observation is at P, at a distance R from the atom. The total distance to P is $X_1 + X_2$. The instantaneous electric field at the point of observation due to the unmodified scattering from electron n located at $\overrightarrow{r_n}$ is

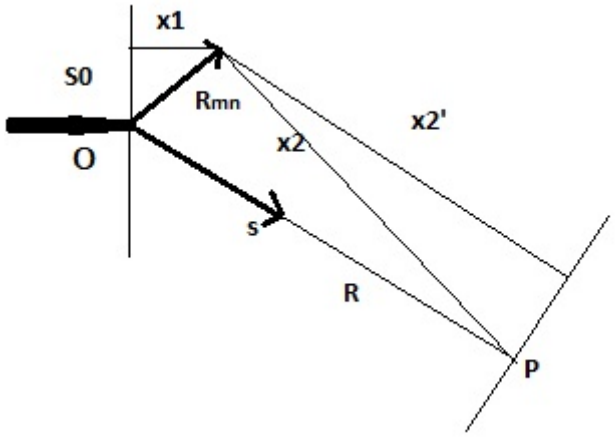

Figure 3.3. Scattering in a crystal. [100]

$$\epsilon_n = \frac{E_0 e^2}{mc^2 X_2} \cos\left(2\pi\nu t - \frac{2\pi}{\lambda}(X_1 + X_2)\right) \tag{3.4}$$

Considering the source and the point of observation are at distances far away compared to $\overrightarrow{r_n}$, the plane wave approximation can be used to get $X_1 + X_2 \rightarrow \overrightarrow{r_n} \cdot \overrightarrow{s_0} + R - \overrightarrow{r_n} \cdot \overrightarrow{s} = R - (\overrightarrow{s} - \overrightarrow{s_0}) \cdot \overrightarrow{r_n}$. The instantaneous field at P is the sum of the

instantaneous electric field for the unmodified scattering due to each of the electrons in the atom at O

$$\epsilon = \frac{E_0 e^2}{mc^2 X_2} \exp 2\pi i \left[\nu t - \left(\frac{R}{\lambda}\right)\right] \sum_n \exp\left(\frac{2\pi i}{\lambda}\right)(\overrightarrow{s} - \overrightarrow{s_0}) \cdot \overrightarrow{r_n} \tag{3.5}$$

If the charge element is ρdV at the position r, the sum is replaced by an integral

$$\epsilon = \frac{E_0 e^2}{mc^2 X_2} \exp 2\pi i \left[\nu t - \left(\frac{R}{\lambda}\right)\right] \int \exp\left(\frac{2\pi i}{\lambda}\right)(\overrightarrow{s} - \overrightarrow{s_0}) \cdot \overrightarrow{r_n} \rho dV \tag{3.6}$$

The scattering factor per electron is defined as $f_e = \int \exp\left(\frac{2\pi i}{\lambda}\right)(\overrightarrow{s} - \overrightarrow{s_0}) \cdot \overrightarrow{r_n} \rho dV$ and this quantity is the ratio of the amplitude of unmodified scattering from one electron to the classical amplitude scattered by an electron. Assuming spherical distribution of charges for an atom containing several electrons, the amplitude of unmodified scattering per atom is the sum of the amplitudes for all electrons where $k = \frac{4\pi \sin\theta}{\lambda}$

$$f = \sum_n f_{en} = \sum_n \int_0^\infty 4\pi r^2 \rho_n(r) \frac{\sin kr}{kr} dr \tag{3.7}$$

f is the atomic scattering factor and is based on the assumption that the x-ray wavelength is much smaller than any of the absorption edge wavelengths in the atom and the electron distribution has spherical symmetry.

A crystal has translational symmetry and the crystal axes are given by vectors $\overrightarrow{a_1}, \overrightarrow{a_2}, \overrightarrow{a_3}$. The parallelepiped formed with the 3 vectors is the smallest volume called the unit cell. When repeated it makes up the crystal. The volume of the parallelepiped is given by $v_a = \overrightarrow{a_1} \cdot \overrightarrow{a_2} \times \overrightarrow{a_3}$. Different atoms in a unit cell are referred as 1,2,3,4..n and their positions from the origin are given by $\overrightarrow{r_1}, \overrightarrow{r_2}, \overrightarrow{r_3}....\overrightarrow{r_n}$. The unit cell is designated by three integers and the position of the atom of type n in the unit cell is given by $\overrightarrow{R_m^n} = m_1\overrightarrow{a_1} + m_2\overrightarrow{a_2} + m_3\overrightarrow{a_3} + \overrightarrow{r_n}$.

A set of crystallographic planes is denoted by the Miller indices hkl. The (hkl) plane has intercepts at $\frac{a_1}{h}, \frac{a_2}{k}$ and $\frac{a_3}{l}$ on the crystallographic axes as shown in figure 3.4. H_{hkl} is a vector perpendicular to the planes hkl and its magnitude is the reciprocal of the inter-planar spacing. The vector H_{hkl} is defined in terms of the reciprocal set

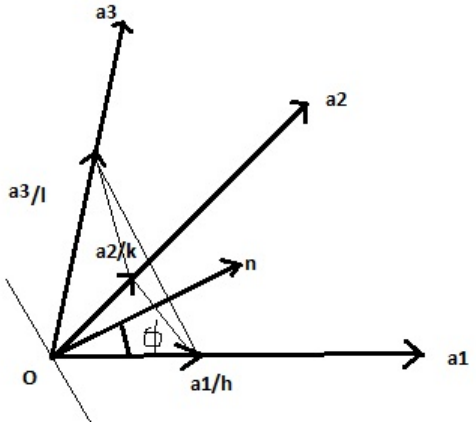

Figure 3.4. Crystallographic axes and Miller indices. [100]

of vectors $\overrightarrow{b_1}, \overrightarrow{b_2}, \overrightarrow{b_3}$ as $\overrightarrow{H_{hkl}} = h\overrightarrow{b_1} + k\overrightarrow{b_2} + l\overrightarrow{b_3}$ where the vectors $\overrightarrow{b_1}, \overrightarrow{b_2}, \overrightarrow{b_3}$ are related to the crystal axes $\overrightarrow{a_1}, \overrightarrow{a_2}, \overrightarrow{a_3}$ as follows:

$$\overrightarrow{b_1} = \frac{\overrightarrow{a_2} \times \overrightarrow{a_3}}{v_a}; \overrightarrow{b_2} = \frac{\overrightarrow{a_3} \times \overrightarrow{a_1}}{v_a}; \overrightarrow{b_3} = \frac{\overrightarrow{a_1} \times \overrightarrow{a_2}}{v_a} \tag{3.8}$$

From these relations, we know $\overrightarrow{a_1} \cdot \overrightarrow{b_1} = 1$ and $\overrightarrow{a_1} \cdot \overrightarrow{b_2} = 0$.

The spacing of the hkl planes is d_{hkl} the perpendicular distance between planes $d_{hkl} = \frac{1}{|H_{hkl}|}$. It is useful to express the Braggs law in terms of the vector H_{hkl}. If $\overrightarrow{s_0}$ and $\overrightarrow{s}$ are unit vectors in the direction of the incident and diffracted beams, we have the vectors $\frac{\overrightarrow{s_0}}{\lambda}$ and $\frac{\overrightarrow{s}}{\lambda}$ make an angle θ with the diffracting planes as seen in figure 3.5

$$| \frac{s - s_0}{\lambda} | = \frac{2\sin\theta}{\lambda} = | H_{hkl} | = \frac{1}{d_{hkl}} \tag{3.9}$$

$$\frac{1}{d_{hkl}^2} = | H_{hkl} |^2 = h^2\overrightarrow{b_1}\cdot\overrightarrow{b_1} + k^2\overrightarrow{b_2}\cdot\overrightarrow{b_2} + l^2\overrightarrow{b_3}\cdot\overrightarrow{b_3} + 2hk\overrightarrow{b_1}\cdot\overrightarrow{b_2} + 2kl\overrightarrow{b_2}\cdot\overrightarrow{b_3} + 2lh\overrightarrow{b_3}\cdot\overrightarrow{b_1} \tag{3.10}$$

Converting to the crystal axes we find

$$\frac{1}{d_{hkl}^2} = \left\{ \begin{array}{c} h^2 | \overrightarrow{a_2} \times \overrightarrow{a_3} |^2 + k^2 | \overrightarrow{a_3} \times \overrightarrow{a_1} |^2 + l^2 | \overrightarrow{a_1} \times \overrightarrow{a_2} |^2 + \\ 2hk (\overrightarrow{a_2} \times \overrightarrow{a_3}) \cdot (\overrightarrow{a_3} \times \overrightarrow{a_1}) + 2kl (\overrightarrow{a_3} \times \overrightarrow{a_1}) \cdot (\overrightarrow{a_1} \times \overrightarrow{a_2}) + \\ 2lh (\overrightarrow{a_1} \times \overrightarrow{a_2}) \cdot (\overrightarrow{a_2} \times \overrightarrow{a_3}) \end{array} \right\} \Big/ v_a^2 \tag{3.11}$$

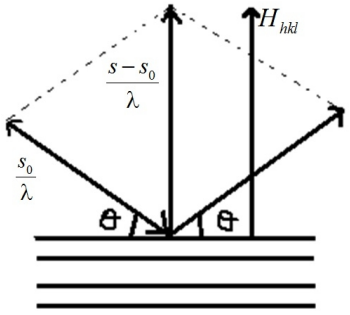

Figure 3.5. Bragg's law and interplanar distance in a crystal. [100]

For cubic lattice where $a = b = c, \alpha = \beta = \gamma = 90°$ the interplanar distance is $\frac{1}{d_{hkl}^2} = \frac{h^2+k^2+l^2}{a^2}$. Now lets calculate the unmodified scattering at P due to atom (m,n) in a crystal

$$\epsilon_p = \frac{E_0 e^2}{mc^2 R} f_n \exp i\{2\pi\nu t - \left(\frac{2\pi}{\lambda}\right)[R - (\overrightarrow{s} - \overrightarrow{s_0}) \cdot (m_1\overrightarrow{a_1} + m_2\overrightarrow{a_1} + m_1\overrightarrow{a_1})]\} \quad (3.12)$$

Summing over all n and all the unit cells of m_1, m_2, m_3 the instantaneous field is

$$\begin{aligned}\epsilon_p = \frac{E_0 e^2}{mc^2 R} \exp 2\pi i \left[\nu t - \left(\frac{R}{\lambda}\right)\right] \sum_n f_n exp\left(\frac{2\pi i}{\lambda}\right)(\overrightarrow{s} - \overrightarrow{s_0}) \cdot \overrightarrow{r_n} \\ \sum_{m_1=0}^{N_1-1} exp\left(\frac{2\pi i}{\lambda}\right)(\overrightarrow{s} - \overrightarrow{s_0}) \cdot m_1\overrightarrow{a_1} \sum_{m_2=0}^{N_2-1} exp\left(\frac{2\pi i}{\lambda}\right)(\overrightarrow{s} - \overrightarrow{s_0}) \cdot m_2\overrightarrow{a_2} \\ \sum_{m_3=0}^{N_3-1} exp\left(\frac{2\pi i}{\lambda}\right)(\overrightarrow{s} - \overrightarrow{s_0}) \cdot m_3\overrightarrow{a_3}\end{aligned} \quad (3.13)$$

Initially we assumed the incident beam to be polarized with electric field perpendicular to the plane of the paper. For an unpolarized beam, E_0 take all orientations perpendicular to $\overrightarrow{s_0}$. For an unpolarized incident beam of intensity I_0 the intensity I_p from a small parallelopipedon crystal is given by

$$\begin{aligned}I_p = I_e F^2 \frac{\sin^2\left(\frac{\pi}{\lambda}\right)(\overrightarrow{s} - \overrightarrow{s_0}) \cdot N_1\overrightarrow{a_1}}{\sin^2\left(\frac{\pi}{\lambda}\right)(\overrightarrow{s} - \overrightarrow{s_0}) \cdot \overrightarrow{a_1}} \frac{\sin^2\left(\frac{\pi}{\lambda}\right)(\overrightarrow{s} - \overrightarrow{s_0}) \cdot N_2\overrightarrow{a_2}}{\sin^2\left(\frac{\pi}{\lambda}\right)(\overrightarrow{s} - \overrightarrow{s_0}) \cdot \overrightarrow{a_2}} \\ \times \frac{\sin^2\left(\frac{\pi}{\lambda}\right)(\overrightarrow{s} - \overrightarrow{s_0}) \cdot N_3\overrightarrow{a_3}}{\sin^2\left(\frac{\pi}{\lambda}\right)(\overrightarrow{s} - \overrightarrow{s_0}) \cdot \overrightarrow{a_3}}\end{aligned} \quad (3.14)$$

where $I_e = I_0 \frac{e^4}{m^2 c^4 R^2} \left(\frac{1+\cos^2 2\theta}{2} \right)$ and $F = \sum_n f_n \exp\left(\frac{-B \sin^2 \theta}{\lambda^2} \right) \exp\left(2\pi i \left(hx_n + ky_n + lz_n\right)\right)$ is the structure factor. Here the factor B takes into consideration the displacement of atoms due to thermal vibrations.

The expression $\frac{\sin^2 Nx}{\sin^2 x}$ is zero everywhere except in the vicinity of $x = n\pi$. So the intensity I_p will be zero unless the three quotients are simultaneously close to their maximum values. So for I_p to be a maximum, it must satisfy the 3 conditions with $h\prime$, $k\prime$, $l\prime$ as integers

$$\begin{aligned} (\overrightarrow{s} - \overrightarrow{s_0}) \cdot \overrightarrow{a_1} &= h\prime\lambda \\ (\overrightarrow{s} - \overrightarrow{s_0}) \cdot \overrightarrow{a_2} &= k\prime\lambda \\ (\overrightarrow{s} - \overrightarrow{s_0}) \cdot \overrightarrow{a_3} &= l\prime\lambda \end{aligned} \tag{3.15}$$

which is $\overrightarrow{s} - \overrightarrow{s_0} = \lambda H_{h\prime k\prime l\prime}$ and this is the Laue equation.

Structure factor for a Bragg reflection

The structure factor $F = \sum_n f_n \exp\left(\frac{2\pi i}{\lambda}\right) (\overrightarrow{s} - \overrightarrow{s_0}) \cdot \overrightarrow{r_n}$ is related to the scattering factor of an atom as in equation below

$$\begin{aligned} F_{hkl} = \sum_n f_n \exp 2\pi i \left(h\overrightarrow{b_1} + k\overrightarrow{b_2} + l\overrightarrow{b_3} \right) \cdot (x_n \overrightarrow{a_1} + y_n \overrightarrow{a_2} + z_n \overrightarrow{a_3}) \\ = \sum_n f_n \exp 2\pi i \left(hx_n + ky_n + lz_n\right) \end{aligned} \tag{3.16}$$

We know that the lattice plus the basis make up the crystal structure. In a crystal whose Bravais lattice is face-centered, the basis vectors of the atoms are (x_n, y_n, z_n), $\left(x_n + \frac{1}{2}, y_n + \frac{1}{2}, z_n\right)$, $\left(x_n + \frac{1}{2}, y_n, z_n + \frac{1}{2}\right)$,$\left(x_n, y_n + \frac{1}{2}, z_n + \frac{1}{2}\right)$ and the simpler form is

$$\begin{aligned} F_{hkl} = [1 + \exp i\pi (h+k) + \exp i\pi (k+l) + \exp i\pi (l+h)] \\ \sum_{\frac{n}{4}} f_n \exp 2\pi i \left(hx_n + ky_n + lz_n\right) \end{aligned} \tag{3.17}$$

If h, k, l are all odd or all even, then $F_{hkl} = 4 \sum_{\frac{n}{4}} f_n \exp 2\pi i \left(hx_n + ky_n + lz_n\right)$, and if hkl is mixed, then $F_{hkl} = 0$.

For this study, the most common structure we looked at was the face centered structure. For example, a rock salt structure with Cl at (0, 0, 0) and Na at (1/2, 1/2,

1/2), the structure factor will take 3 forms as follows: hkl all even, $F_{hkl} = 4\,(f_{Cl} + f_{Na})$; hkl all odd $F_{hkl} = 4\,(f_{Cl} - f_{Na})$; and hkl are mixed, then $F_{hkl} = 0$.

The incident beam is not parallel in normal imaging conditions and different parts of the same small crystal would not be parallel. In this case, there will be diffraction radiation over a range of angle on either side of the exact Bragg law direction, requiring a narrow slit on the peak of the diffracted beam. Assume that during the measurement, the crystal is rotated at constant angular velocity ω parallel to the planes hkl and normal to the incident beam, and the total diffracted energy given out by the crystal is measured. The total energy E, an experimentally observable quantity is obtained by integrating the intensity over time and over area of the receiving surface, the final expression is $E = \frac{I_0}{\omega}\left(\frac{e^4}{m^2c^4}\right)\frac{\lambda^3\delta V F^2}{v_a^2}\left(\frac{1+\cos^2 2\theta}{2\sin 2\theta}\right)$ where δV is the volume of the small crystal.

In powder method, a monochromatic beam falls on a powder sample made of crystals in random orientations. Let M be the number of crystals in the sample, δV the average volume per crystal and vectors H_{hkl} are constructed for each crystal. For the powder sample, the effective number of these vectors will be Mm_{hkl} which depends on (hkl) and crystal symmetry. The total diffracted power in a (hkl) reflection is given by

$$P = I_0\left(\frac{e^4}{m^2c^4}\right)\frac{V\lambda^3 m F^2}{4v_a^2}\left(\frac{1+\cos^2 2\theta}{2\sin 2\theta}\right) \tag{3.18}$$

In practice, we measure the power per unit length of the diffraction circle on the receiving surface, given by

$$P = \frac{I_0}{16\pi R}\left(\frac{e^4}{m^2c^4}\right)\frac{V\lambda^3 m F^2}{v_a^2}\left(\frac{1+\cos^2 2\theta}{2\sin\theta\sin 2\theta}\right) \tag{3.19}$$

This important quantity is directly proportional to the peak area on a diffractometer pattern. This quantity in our measurement provides an estimate of the phase volume in multi-metallic nanoparticles or thin films.

3.3 Synchrotron based x-ray diffraction

Synchrotron based x-ray sources facilitate many experiments not possible with conventional x-ray sources. The high flux and wide range of x-ray energy are some of the big advantages of using a synchrotron facility. In this study, synchrotron based x-ray diffraction technique is used to study the structural evolution of nanoparticles undergoing thermal annealing.

Synchrotron facilities make high flux electron beams by accelerating electrons close to velocity of light in ultra high vacuum segments attached to a storage ring. The electron beams are injected in bunches and each of the electron bunches contributes to the total current. The energy of the emitted x-rays is dependent on the energy of the electron in the storage ring. The storage rings have many segments. The curved segments have bending magnets which direct the electrons on a circular path. Wigglers and undulators consisting of arrays of magnets produce magnetic fields which are alternating. In bending magnets and wigglers, the tighter curvature ensures high energy of the x-rays. Undulators have magnets positioned precisely to accelerate the electrons due to Lorentz force. As the electron beams pass through the insertion devices, they accelerate to produce photon emission. This causes the electrons to oscillate and each oscillation emits synchrotron radiation that can be manipulated to the desired wavelength, amplitude and frequency. Bending magnets and undulators have a series of peaks at higher multiples of a fundamental energy with wavelength λ. The energy of the fundamental and its harmonics are varied by the gaps between the magnets. Lorentz contraction sharpens the radiation and it diverges only a few mm over a large distance. Brightness averaged over solid angle is used to quantify the beam line. Each beam line is designed for a specific set of experiments. Monochromators and goniometers are used as per the experimental requirements in the hutch of the beam line [101].

3.3.1 Beamline X20C at the National Synchrotron Light Source (NSLS)

NSLS at Brookhaven National Laboratory (BNL) has a second generation storage ring. NSLS has two storage rings: one for vacuum Ultraviolet or soft x-rays and one for hard x-rays (figure 3.6). The soft x-rays ring has electron energies of 0.8 to 2.0 GeV and is used for photoelectron spectroscopy and lithography. Hard x-rays are produced by electrons of energies 2.6 to 8GeV and are used for diffraction and extended x-ray absorption fine structure (EXAFS). Some of the uses of the high flux x-rays are to probe interfaces in complicated stacked structures, characterize polymers and *in situ* phase transformations. There are several beam ports on the hard x-ray ring where the dipole magnet emits synchrotron radiation. Each of the beam ports are subdivided into beam lines catering to a particular experimental technique. The hard x-ray ring at NSLS has a 170m circumference with 60 beam

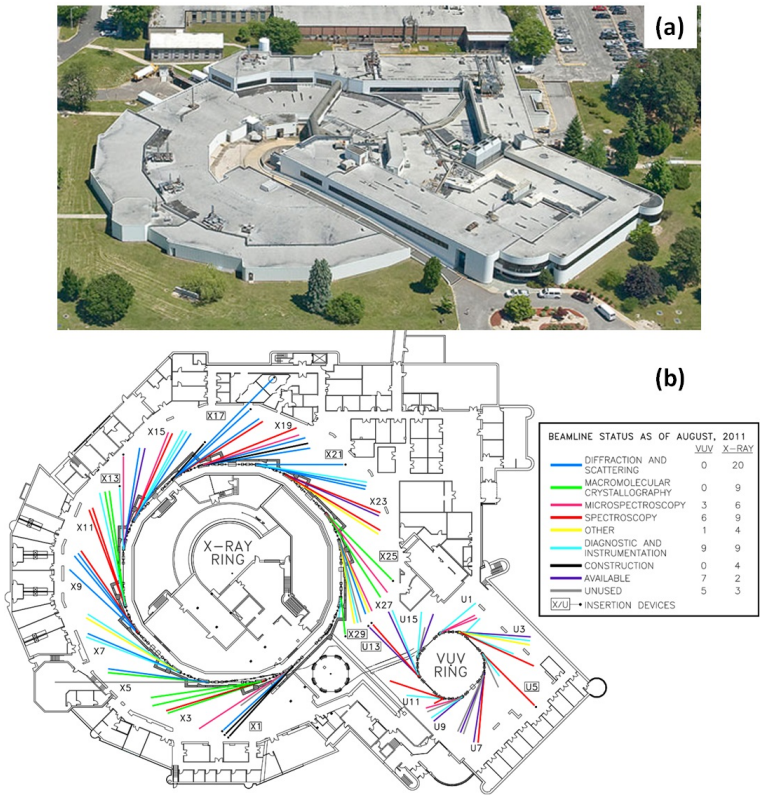

Figure 3.6. (a)NSLS at BNL (b) Beamlines with their main experiments in the inset.

lines and 30 beam ports. The energies of the electrons are 2.58 or 2.8 GeV and the maximum current is 25-400mA. The x-rays from the storage ring are directed to the beamline in an evacuated stainless steel pipe and are passed through the beryllium window into the experimental set up hutch. The experiments done with hard x-rays are diffraction, inelastic scattering, EXAFS, topography, tomography, small angle scattering, fluorescence, atomic spectroscopy, microscopy and radiography. The high x-ray intensity of the synchrotron radiation sources and efficient position sensitive area detectors allow high quality diffraction data with good time resolution. These set-ups can study the dynamics of processes in materials in physical or chemical reactions or static experiments of materials in complex situations such as catalysts in operating conditions.

Paul Horn, Robert Birgeneau and G. B. Stephenson of IBM developed the beamlines in the port X20. The studies at the Port X20 are basically of 5 types: (i) triple axis diffraction for measuring strain relaxation in SiGe structures, (ii) grazing incidence diffraction for studying ordering in polymers, (iii) time resolved *in situ* diffraction to study phase transformations, (iv) microdiffraction to measure strain field in Si by evaporated Ni metal features, and (v) reflectivity techniques to measure the interfacial and surface roughness. These techniques measure (i) lattice spacing changes due to applied stress or epitaxial strain (ii) changes in peaks positions in case of phase transformations in crystalline materials (iii) orientation and texture in polycrystalline materials. The measurements described in this thesis were mostly time resolved *in situ* diffraction to study phase transformations, changes in peak positions, peak widths and integrated intensity.

Beam line X20C is dedicated to *in situ* time resolved x-ray diffraction studies and the instrumentation was developed to study diffusion barriers, kinetics of phase separation and texture evolution in alloys. X20C has a standard Huber diffractometer configured for time-resolved diffraction with a special chamber and fast linear detector as shown in figure 3.7 [102].

The important components of beam line X20C are the monochromator, detectors to collect the diffraction data in rapid time scales and a unique chamber with ability to control the sample temperature. Additionally, the set-up can do four-point resistance measurements and elastic light scattering measurements from a sample. The monochromator consists of W-Si synthetic multilayer of d-spacing of $\approx 22\mathring{A}$ allowing an energy spread of $\Delta E/E \approx 1.2X10^{-2}$ and beam intensity of the order of 10^{11} photons/s at 6-8KeV. This monochromator yields 100 times more flux than monochromators on beam lines X20A and B.

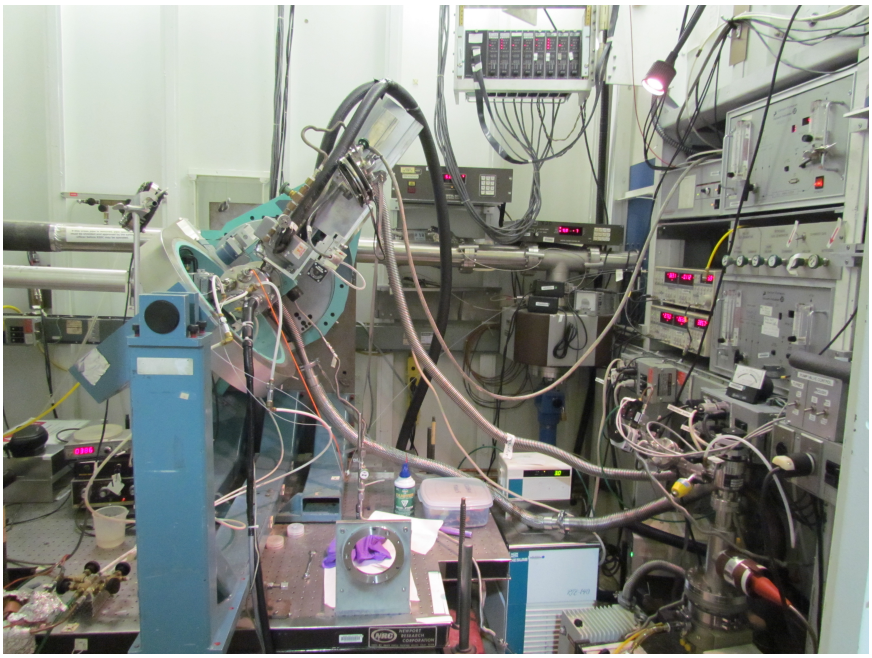

Figure 3.7. XRD set up at the beamline X20C

The detector is a linear diode array of length 1 inch or a CCD detector which has an area of $1 \times 1inch^2$. The linear detector can take 1024 point scattering patterns in 17 milliseconds [103]. The chamber enables rapid thermal annealing of the sample. The temperature of the sample can be increased to 1200°C in vacuum and inert gases. It can also quench the sample to room temperature to freeze its structure for ex-situ analysis. A sample can be extensively studied for the entire temperature range in a short span of time along with the effect of variation of ramp rate, substrate type, end

point temperatures, doping etc. The schematic diagram of the beam line X20C along with its important components are shown below in figure 3.8.

Additional capabilities include a rapid thermal annealing stage in a continuous flow of high-purity helium gas or forming gas (5.17 % H2 in N2). A linear position-sensitive detector was used to record the XRD pattern around the face centered cubic (111) and (200) peaks (45°-60° angular range) with two-second time resolution. The nanoparticle mixtures dispersed on carbon powder, 0.5 m-thick SiO2 layer, and alumina membranes were supported by a Si (100) wafer that was held in place with four pins on a molybdenum sample holder. High vacuum was first established in the sample chamber at the beginning of the experiments to remove all oxygen, and then the chosen gas was continuously flowed. Various thermal treatments are made possible by a Eurotherm programmable temperature controller measuring the temperature of the sample holder with a thermocouple. Each of the annealing cycles lasted for ten minutes. Before and after each thermal treatment θ-2θ scans were recorded in the 20°-60° angular range at room temperature. The contour map of the diffracted x-

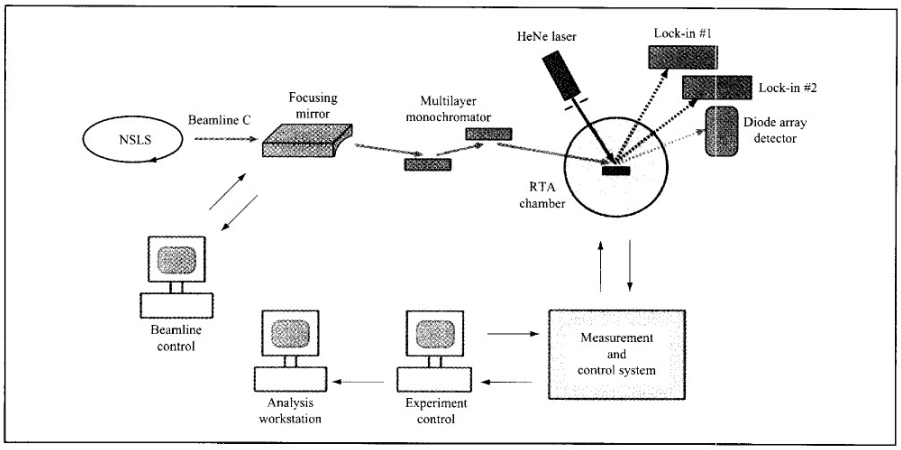

Figure 3.8. Schematic block diagram of the XRD set up at beamline X20C [103].

ray intensity is obtained in a typical *in situ* study as shown in figure 3.9. Red and blue represent high and low intensity, respectively. This set up is ideal for studying structural transformations in catalytic materials as a function of thermal annealing in

conditions similar to the ones the material is subjected to during the typical synthesis process. The X-rays from the synchrotron source have high flux and brightness that are suitable to measure signals from thin, small and low density samples.

Two kinds of data are acquired in this study. The first one is the isothermal/ramped annealed data which shows the evolution of the intensity of the XRD peaks from the samples with time/temperature. Typically, a conventional *ex situ* XRD pattern gives the intensity of the scattered x-rays from the sample as a function of the angle of the detector. Figure 3.9 shows the XRD data from the beamline X20C corresponding to PtNiFe nanoparticles annealed to 950°C. The left side panel of figure 3.9 (a) is the color map showing the intensity variation of the (111) and (200) peaks of the fcc structure. The right side of the panel in figure 3.9 (a) shows the XRD plot at t= 320 seconds. Here the formation of the disordered alloy is indicated by the peaks at 48.5° and 56.5° corresponding to the fcc (111) and fcc (200) planes respectively. This data can also be visualized as a 3-dimensional plot with x-axis, y-axis and z-axis corresponding to the angle of the detector, time, and intensity of the scattered x-rays, respectively, as shown in figure 3.9(b).Throughout this study, the XRD data are presented in the form shown in figure 3.9(a). Figure 3.9(b) is shown here to facilitate understanding of the data. In case of isothermal annealing, the y-axis is the time as the temperature is maintained constant throughout the experiment. In case of the ramped annealing, the temperature is ramped and the data can be plotted with time or temperature on the y-axis. Figure 3.9(c) shows the $\theta - 2\theta$ scans of the diffraction pattern before the anneal and after quenching the annealed sample to room temperature. Here we see initially the XRD is a diffuse broad peak typical of small crystalline nanoparticles (<5nm). During annealing the nanoparticles undergo grain growth forming sharp peaks with fcc structure. It is very important to scan the samples after each anneal to check the phases present. The $\theta - 2\theta$ scans are done in the range $20 - 60°$. Here we have shown the data after background subtraction and removing the peaks corresponding to the substrate on which the nanoparticles were dispersed.

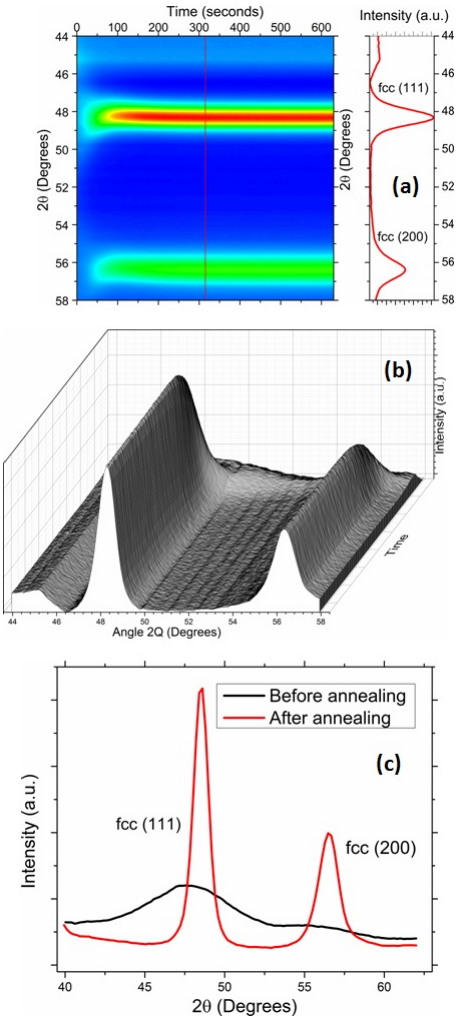

Figure 3.9. Typical XRD data (a) Time evolution of the intensity of the scattered radiation from a PtNiFe nanoparticles sample (left panel)and the right panel is the XRD pattern at t= 320° s. (b) The XRD data represented in three dimensions with intensity of the X-ray peak, time and angle 2θ along the z, y and x-axis, respectively. (c) $\theta - 2\theta$ scans.

In order to explore the details of the phase evolution of the nanoparticles with thermal processing, it is very important to analyze the XRD data obtained. To extract the information about the phase-transformation, the diffraction pattern was fitted with a series of Lorentzian peaks, typically a single peak corresponding to the non-crystalline phase before heating and two or three peaks after heating corresponding

to the fcc (111) and (200) peaks. The phase volume, lattice constant and grain size were calculated using the peak area, peak center, and peak width, respectively. The mathematical form of the Lorentzian is

$$y = y_0 + \frac{2A}{\pi}\frac{w}{4\left(x - x_c\right)^2 + w^2} \tag{3.20}$$

where x is the angle of the detector, y the intensity, y_0 is the background, A is the peak area, x_c is the peak center and w is the peak width. Apart from the identification of structure and phase of the materials, XRD data can be analyzed for grain size, elemental content, strain, etc. Using the peak width and Debye-Scherrer formula, one can obtain the qualitative grain size of the nanoparticles :

$$\tau = \frac{K\lambda}{\beta\cos\theta} \tag{3.21}$$

where K is the shape factor, λ is the wavelength of the x-ray used and β is the full width at half maximum (FWHM) of the diffraction peak in radians. The Scherrer formula was found to accurately reproduce the diameter of spherical nanoparticles as measured with TEM when used with the proper coefficient [104]. K= 1 for spherical particles was used in this study. We also found good agreement between the TEM and XRD size calculated from the Scherrer formula using the FWHM of symmetric $\theta - 2\theta$ scans, but we note that due to the limited angular acceptance of our detector, the small particle sizes (<7nm) can be underestimated by as much as 10% in the time-resolved scans which were taken with a fixed detector.

Vegard's law [105] is an empirical rule that states that a linear relation exists, at constant temperature, between the crystal lattice parameter of an alloy and the concentrations of the constituent elements along with their lattice constants. For example, the lattice parameter of an alloy Z formed from elements X of lattice parameter a_x and Y of lattice parameter a_Y is given by

$$a_z = \left(f a_x\right) + \left(\left(1 - f\right) a_Y\right) \tag{3.22}$$

where a_Z the lattice parameter of the alloy Z, and f is is is the fraction of element X in the alloy. Vegard's law was used to calculate the nanoalloy composition.

3.4 Transmission electron microscopy (TEM)

In transmission electron microscopy, the electron beam passes through the nanoparticles dispersed on a microgrid. This technique measures the size distribution with sufficiently high resolution, the particle structure and morphology. TEM allows imaging of defects as well. Different modes of imaging in TEM help in extracting different information about the sample being probed. Bright field imaging, a commonly used imaging mode, is a projection of the sample to two dimensions. Selected area diffraction is used to identify crystallographic structures and phases from different regions of the sample. Converged beam electron diffraction can be used to identify the point-group symmetries and nanoscale diffraction. Diffraction contrast imaging is used to identify stacking faults, dislocations and grain boundaries. High angle annular dark field- scanning transmission electron microscopy (HAADF-STEM) mode of imaging enables atomic number contrast in images at atomic resolution. Energy dispersive x-ray spectroscopy (EDX) is used for detecting elements in the sample. Electron energy loss spectroscopy (EELS) probes the chemical states of the elements present in the samples. EELS along with energy-filtered imaging allow imaging using electrons that have lost a particular energy value (corresponding to an element) and therefore can map that element in the sample.

A TEM microscope has three major components: the illumination system, the objective lens/stage and the imaging system. The gun and condenser lenses (C1, C2 and C2 aperture) form the illumination system as shown in the schematic diagram of the TEM in Figures 3.10 and 3.11. The standard electron source is a field emission gun (FEG) which has a needle shaped tungsten crystal emitting electrons due to field emission in a high electric field. In FEGs, the electrostatic lens acts as a virtual source with a probe diameter of the order of sub-nanometers. The optical system in the TEM is mostly comprised of lenses made of copper coils. The magnetic field is produced by the current in the coils. The electron beam trajectory is manipulated by magnetic field and can be focused just like in an optical microscope. The focal

length (f) of the lens is given by $\frac{1}{f} = \frac{e^2}{4mv^2}\int_{L1}^{L2} B^2(z)\,dz$ where B is the magnetic field, v is the speed of the incident electrons, m is the mass, e is the charge, and z is the direction defined by the optical axis [106]. Since the magnetic field is dependent directly on the current in the coils, more current leads to smaller focal length.

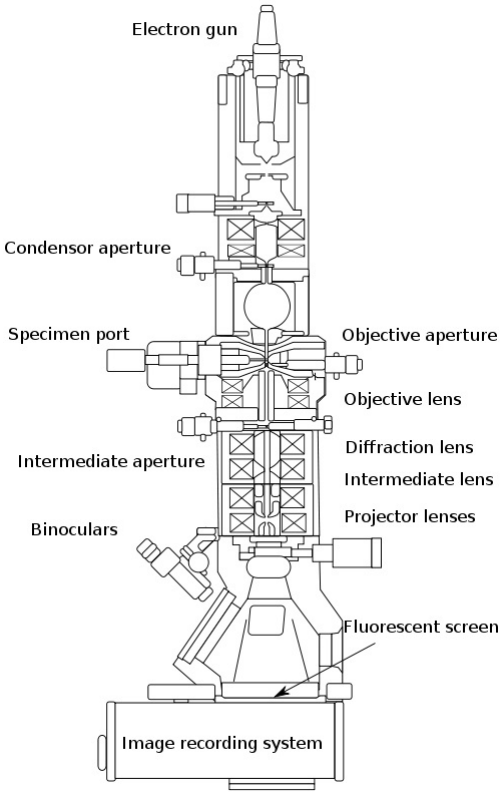

Figure 3.10. Schematic diagram of TEM

There are three groups of lenses in the microscope. The first group of lenses forms the image of the source on the sample. It consists of condenser lenses C1 and C2, condenser mini-lens and upper objective lens (figure 3.11). The current in the coil controls the probe size and the convergence angle of the beam on the sample. The beam size is also affected by the condenser aperture on C2 which limits the angular opening of the electron source and increases the coherence of the beam, an important condition for diffraction.

The interaction of the electrons with matter is about 10^4-10^5 times higher than with x-rays or neutrons, enabling strong absorption of electrons by specimen. The absorption is dependent on the accelerating voltage and thickness of the sample. With an accelerating voltage of 200kV, the speed of the electrons is 0.695 times the speed of light and corresponds to a wavelength of 0.00251nm. At this wavelength, it enables diffraction on crystal lattices which leads to many important modes of imaging in TEM.

The illumination system operates in two modes parallel beam and convergent beam. Selected area electron diffraction (SAED) involves the parallel beam while scanning transmission electron microscopy (STEM) and spectroscopy use the convergent beam. STEM mode uses an extremely convergent electron probe and scans over a small part of the sample, enabling analysis of the structure and local chemistry of nanoalloys. The other mode is the conventional TEM imaging mode which is similar to the operation of an optical microscope. The beam sample interaction takes place in the specimen holder leading to the creation of images and diffraction patterns that are magnified for viewing. The defects in the objective lenses are overcome by aberration-corrected systems which are attached in this section of the TEM.

The imaging system uses several lenses like the magnifying lenses consisting of the intermediate lenses and diffraction lenses. The final lenses are the projector lenses. The detection system typically consists of charged coupled devices (CCD) type cameras. A CCD camera is an array of photodiodes. The data-acquisition and data-processing interface of current microscopes are easier with CCDs.

Diffraction in nanoparticles is of two kinds. When the nanoparticles have a particular orientation one observes the diffraction as in the case of monocrystal, i.e an arrangement of spots with particular angles and distances suggesting a particular geometry and symmetry of the crystal lattice. Otherwise, in the case of randomly oriented nanoparticles, the diffraction pattern shows mostly diffuse rings around the transmitted beam. The conventional mode of imaging and diffraction are the basic functions of the TEM used to obtain the size and the structure of the nanomaterials.

Conventional TEM and selected area diffraction (SAED) use the parallel mode of illumination. If the C2 lens is used to produce an image of the source at the front focal plane of the upper objective pole piece, then a parallel beam of electrons results. In these cases, a smaller C2 condenser lens is focussed and therefore makes the beam more parallel. Figure 3.11(a) illustrates the condition required for STEM. The upper pole piece of the objective lens acts as C3 lens and controls the beam hitting the specimen. Primarily, the C2 lens is underfocussed and the beam is convergent. The convergent beam mode is a probe used in EELS, HAADF-STEM and EDX.

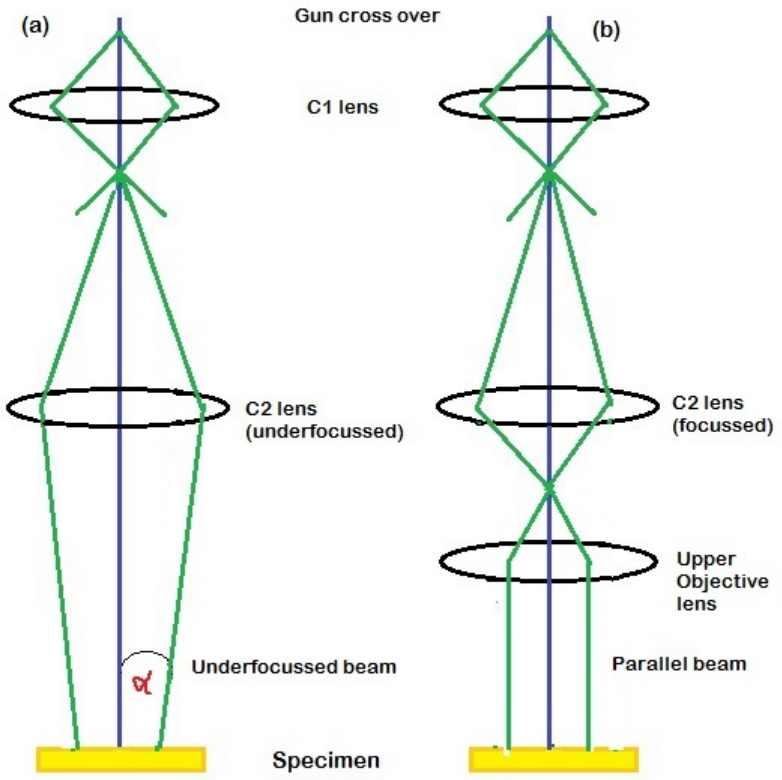

Figure 3.11. Two common modes of imaging in TEM (a) Imaging condition for STEM mode (b) Conventional mode of imaging [106].

The second part of the TEM is the objective lens and stage. The stage is used to insert the sample into the column. The standard sample holder is called the single-tilt holder. If the experiments require tilting of the sample to a particular zone axis, then

the double tilt holder is used. The height of the sample in the column is measured by z-height. The reference plane for the holder is the Eucentric plane and is normal to the optic axis ensuring the image is in focus and the point in the optical axis will not move laterally when tilted around the axis. Since all allignment in the TEM changes with z-height, the first step when the sample is inserted into the column of the TEM is to do z-height and Eucentric height adjustments. The objective lens takes the electrons from the sample, disperses them to create a diffraction pattern in the back-focal plane and recombines them to form an image in the image plane. The objective aperture controls the collection angles and influences the resolution of the TEM.

The imaging system of the TEM has two primary modes of operation (a) Diffraction mode and (b) Image mode. In the diffraction mode, the main step is to set the imaging-lenses so the back-focal plane of the objective lens acts as an object for the intermediate lenses. An aperture is inserted above the specimen to permit only the electrons diffracted from a specific area of the sample. While acquiring the diffraction pattern image, the direct beam is so intense that it is covered by the beam stopper to prevent damages to the camera. For the bright field image, the objective diaphragm is used to block all the diffraction pattern except the direct beam. For the dark field image, the objective diaphragm is used to block the direct beam. For the conventional image mode, the object plane of the intermediate lenses is the image plane of the objective lenses and the image is projected to the viewing screen.

Two factors limiting the objective lenses are sperical aberrations and astigmatism. Sperical aberrations have a strong dependance on the probe size, parametrized by a minimum radius $r_{min} \approx 0.91\,(C_s\lambda^3)^{\frac{1}{4}}$ where Cs is the spherical aberration coefficient of the lens.The C2 aperture also depends on the collection angles [106] $\alpha_{opt} = 0.77\frac{\lambda^{\frac{1}{4}}}{C_s^{\frac{1}{4}}}$. Astigmatism occurs when the electrons sense non-uniform magnetic fields when they pass the optical axis. This is corrected by the stigmators for the condenser lenses in illumination system and in the objective lens in the imaging system. Astigmatism also arises due to misaligned condenser aperture or contamination. So it is important to

align the condenser aperture to correct stigmation, so that the image of the electron source is circular. Apart from spherical aberration, there is chromatic aberration when the beam passes down a sample. Chromatic aberration also affects the images, and it gets worse with thicker samples. The objective lenses bend the electrons of lower energy more and the point in the sample is blurred to form a disk in the image plane. The radius of this disk is $r_{chr} = C_c \frac{\Delta E}{E_0} \beta$ Where the C_c chromatic aberration coefficient of the lens, ΔE is the energy loss of the electrons, E_0 is the initial beam energy and β is the angle of collection of the lens.

Specific TEM based techniques used to study the trimetallic Pt-based, Pd-Cu, Pd-Au and Au-Cu nanoparticles are high resolution TEM (HRTEM), high angle annular dark field scanning transmission electron microscopy (HAADF-STEM), energy dispersive x-ray spectroscopy (EDX) mapping, electron energy loss spectroscopy (EELS) and energy-filtered TEM (EFTEM). These experiments were performed on FEI Tecnai and FEI Titan at Purdue University. EDX measurements were performed by our collaborator, Dr. D. N. Zakharov on Hitachi HD 2700C at the Center for Functional Nanomaterials, Brookhaven National Laboratory.

3.4.1 High resolution transmission electron microscopy

Size and crystalline structure strongly influence different properties of metallic nanoparticles, especially in the size range below 10nm. HRTEM is a technique of choice as it allows simultaneous size and structure analysis. HRTEM produces an image of the interference between the scattered and unscattered beams. This is achieved by means of an aperture in the back focal plane of the objective lens. The contrast in these images is obtained from the relative phase shifts in the electron beams and it is also called phase contrast imaging. A Fourier transform of the HRTEM image reveals the crystal structure and defects in the sample as shown in the figure below.

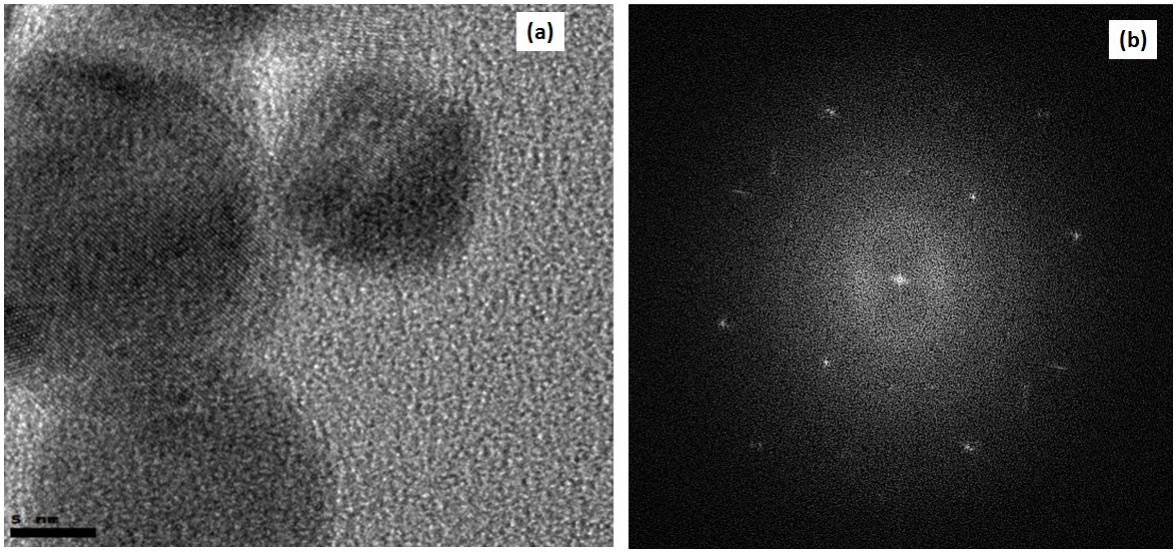

Figure 3.12. (a)High resolution image of Pd-Cu alloy nanoparticles (b) Fast Fourier transform of the HRTEM in (a)

HRTEM data analysis

Since it is very challenging to orient groups of small nanoparticles along a zone axis and to capture the diffraction pattern, it is advantageous to use the fast Fourier transforms (FFT) of the HRTEM images. The high resolution TEM images were used to estimate the lattice spacing corresponding to a structure of the materials. It is very important to have a high resolution TEM image which has structures resolved in more than one direction to predict the exact structure of the material. CrystalMaker is a visualization software package developed by academics in Oxford Universitys Begbroke Science Park, UK. The FFT of a HRTEM image is generated using Gatans Digital Micrograph software, and the diffraction patterns with various zone axes are obtained from Single Crystal, software from CrystalMaker. In order to simulate the diffraction pattern, the Inorganic Crystal Structure Database was searched for the various structures of the alloy and compounds to obtain the corresponding crystallographic information file (.cif) files. These .cif files or .cmdf files (CrystalMaker data

format) can be used to generate a 3 dimensional image of the crystal structure using commonly available programs like JMol, CrystalMaker, etc. The distance between the spots and the angles between the spots in the diffraction pattern were measured using Gatan s Digital Micrograph and Image J, another image processing software developed at the National Institute of Health. These quantities are compared with the simulated diffraction pattern from Single crystal and information is inferred such as Miller indices of each of the diffraction spots, the zone axis of the image, etc.

For measuring the size of the particles, the images of nanoparticles at various magnifications were acquired. To help ImageJ software detect the nanoparticles, circles were drawn around the nanoparticles on the image files. ImageJ calculates the area and perimeter of the nanoparticles. The nanoparticles were spherical for most of the experiments in this thesis. The diameters of the particles were obtained for at least 100 nanoparticles and the size distribution was plotted using Origin. These distributions were fitted with Gaussian curves to estimate the average size and error in these measurements.

To get good high resolution images in TEM, it is very important to understand and keep the stigmations to the minimum. The performance of the TEM is given by the contrast transfer function, and this is affected by the spherical and chromatic aberration of the lenses involved in imaging. The contrast transfer function is dependent on variation of the focal length of the objective lens Δf, the chromatic and spherical aberrations denoted by C_c and C_s and the spatial frequency ν:

$$T(\nu) = \exp -i\chi(\nu) = \exp -i\pi\lambda\left(C_s\lambda^2\frac{\nu^4}{2} + \Delta f\nu^2\right) \tag{3.23}$$

where $\chi(\nu)$ is the total phase shift which modifies the amplitude and phase of the wavefront of the beam between the object plane and back focal plane of the lens. The total coherent transfer function is a product of the coherent transfer function and the envelope functions. The envelope function gives information on the spatial and temporal coherence of the beam. The temporal coherence leads to the spread of the defocus of the image δ which is dependent on the fluctuations in the high voltage source, lens current ΔI_{obj} and the energy dispersion in the electron beam ΔE

[106]. $\delta = C_c \left(4 \left(\frac{\Delta I_{obj}}{I_{obj}} \right)^2 + \left(\frac{\Delta E}{V} \right)^2 + \left(\frac{\Delta V}{V} \right)^2 \right)$ where C_c is the chromatic aberration coefficient.

The envelope function corresponding to the temporal coherence is

$$E_c(\nu) = \exp\left(-\frac{1}{2} (\pi \lambda \delta)^2 \nu^4 \right) \tag{3.24}$$

This function accounts for the sample drift and vibrations. The envelope function corresponding to the spatial coherence has a dependence on divergence of the beam emitted by the gun parameterized by the angle of convergence on the sample and is given by $E_s(\nu) = \exp\left(-\frac{\pi \alpha^2}{Ln2} \left(C_s \lambda^2 \nu^3 + \Delta f \nu \right)^2 \right)$

3.4.2 High angle annular dark field - scanning transmission electron microscopy (HAADF-STEM)

STEM can access the Z-contrast, i.e. elemental composition of bi- or tri-metallic nanoparticles. High angle annular dark field (HAADF) STEM is capable of imaging atomic clusters and allows single columns to be clearly identified within each nanoparticle with atomic scale resolution.

This mode of imaging requires the intensity of the beam on a specific area of the specimen to be increased. In this case, the C2 is focussed and the beam is most convergent. This reduces the image contrast and to form an image, the beam is scanned over the sample in this mode of operation. The beam is made parallel by using scan coils to pivot the beam about the front focal plane of the objective pole piece. The beam then emerges through a third condenser lens parallel to the optic axis to form the image on specimen plane. The quality of STEM images is dictated by the quality of the STEM detector. Figure 3.13 shows a STEM image taken by the Titan 300 kV at Birck Nanotechnology Center, Purdue University. In STEM images, the brightest regions have high Z-value, i.e. element with high atomic number. In this case, the sample has both Pd and Cu nanoparticles and the bright regions correspond to the Pd atoms in the sample.

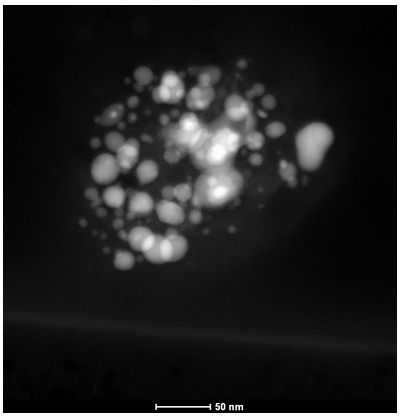

Figure 3.13. (a)A typical STEM image of Pd-Cu nanoparticle mixture.

3.4.3 Energy Dispersive X-ray spectroscopy (EDX)

Electrons can eject a core electron from an atom in the sample because the energy of the electron beam is more than the binding energy of the core electrons. This causes X-ray-photons to be emitted with an energy equivalent to the energy difference caused by the movement of an electron from a higher orbital to the core shell. The X-ray-photon emitted is characteristic of a particular element. The EDX analysis uses a detector placed above the sample to count and analyze the energy of the x-rays emitted by the sample. The EDX data consists of an energy spectrum of the emitted x-rays in the range 0-20 keV in which elements can be identified from the spectral peaks. EDX analysis performed on multi-metallic nanoparticles can provide evidence of the relative compositions of their elements as shown in figure 3.14 in the case of PdCu nanoparticles.

3.4.4 Electron energy loss spectroscopy (EELS) and Energy filtered transmission electron microscopy (EF-TEM)

Transmission electron microscopy uses EELS or EDX for chemical analysis. EELS is due to the inelastic scattering process the electron beam undergoes when it interacts with the sample materials. When the high energy electron beam passes through the

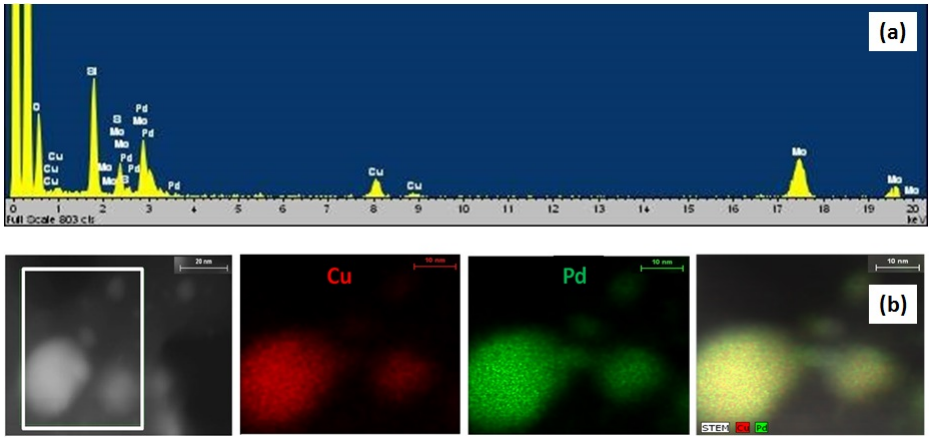

Figure 3.14. (a)A typical EDX spectra. (b) EDX maps of Pd-Cu nanoparticles.

sample, free electron (most metallic samples) plasmons are created. These plasmons are vibrations undergone by the electron beam and they generate broad peaks in EELS spectra. Plasmon spectra can measure the free electron density and thickness of samples. EELS shows absorption edges at energies required to eject core electrons from the materials. After the core electron is excited, the core hole decays by emission of characteristic x-rays which is recorded in the EDX.

When the electron beam traverses the specimen, some of the electrons lose energy to plasmons and core excitation. To measure the EELS spectra, an EELS spectrometer is mounted after the projector lenses in the microscope. This spectrometer has a magnetic sector having a homogeneous magnetic field which disperses the electron energy, and the electrons of the same energy follow the same curved path. The magnetic sector also focuses the electrons in the plane of the paper. The electrons losing more energy to the specimen will move more slowly and are bent upward. A slit and scintillation counter are placed on the focal plane of the magnetic sector. The magnetic sector spectrometer is coupled to the microscope and the collection angle is controlled by objective aperture or the aperture at the entrance of the spectrometer. The energy resolution of 0.1eV is possible with the field emission gun and Wien filter. Electrons of velocity v for which the electric and magnetic force cancel pass through

the exit aperture of the Wien filter. The Wien filter disperses electrons of different energy into different angles and then allows electrons of particular energy to pass through the aperture. We briefly discuss the general features of EELS spectra shown in figure 3.15. The big peak at 0eV in figure 3.15 (a) corresponds to the zero-loss peak from the electrons of energy 200KeV passing through the specimen without any energy loss. Next we see a plasmon peak around 25eV as shown in figure 3.15 (a) from the electrons of energy 199.975KeV caused by the excitation of one Plasmon from the sample. The background in EELS falls fast proportional to (Δk^2) where k corresponds to the wave vector of the electron. The important features of EELS that reveal the chemical composition of the samples are the core losses. For example in PdCu nanoparticles sampled using Titan 300KeV, we see a core loss at 284eV, 330eV (see figure 3.15 (b)) and a doublet at 930 and 950eV (see figure 3.15 (C)). The core loss at 280eV corresponds to the excitation of electrons from 1s out of the C atom called the K-edge. From Pd atom, the electron energy loss shows as edge peak at 330 eV. The Cu atom has a doublet corresponding to the edges L_2 and L_3. The L_3 edge at 930 eV corresponds to the excitation of the $2p_{\frac{3}{2}}$ electrons out of the Cu atom and L2 edge at 950 eV corresponds to the excitation of the $2p_{\frac{1}{2}}$ electron out of the Cu atom. The regions in the EELS spectrum around a core loss edge are also called the electron energy loss near edge structure (ELNES). They are used to study the chemical bonding in the samples. Changes in the chemical bonding of the atom alter the lowest unoccupied molecular orbital and this shifts the onset energy of the core edge.

Energy-filtered transmission electron microscopy (EFTEM) uses a variable-size slit to form an image with only the electrons of a desired energy value. It makes use of a 3-window method to get the chemical map of a desired element (corresponding to the energy value) in nanoparticles or in thin films. Here in figure 3.15 (d), we show a typical EFTEM set of images. This method consists of obtaining the image with a slit centered at the absorption edge of the element with two pre-threshold images. In figure 3.15 (d), the first two images are the pre-edge and post-edge images

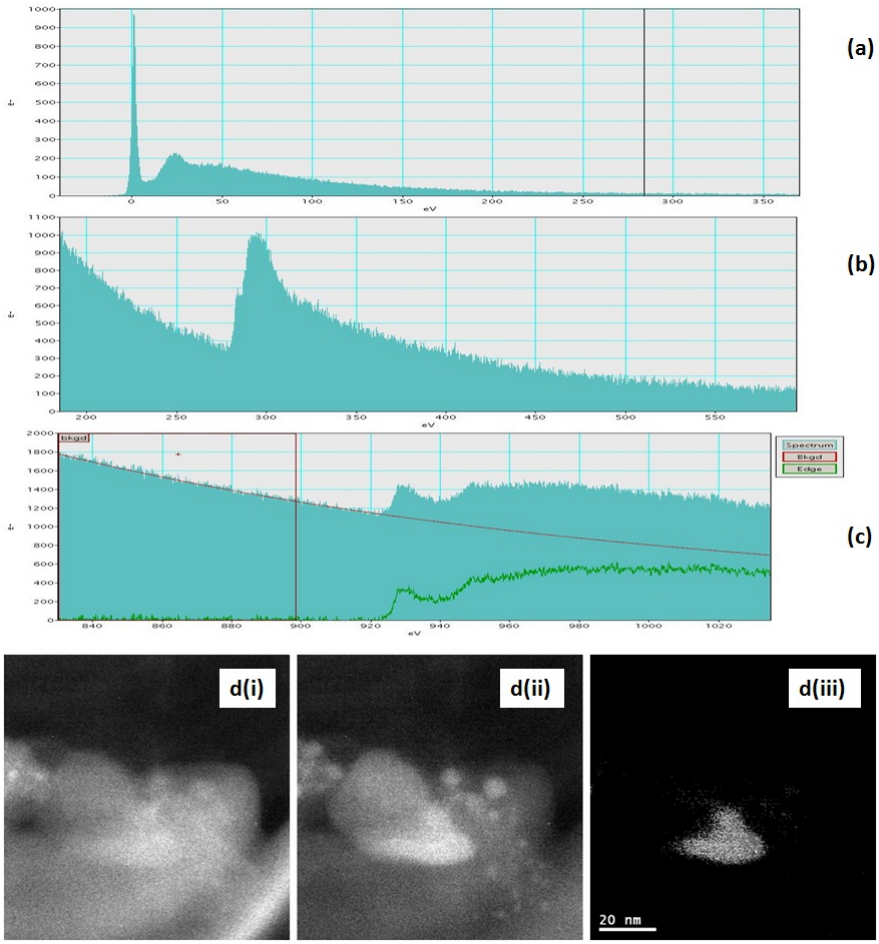

Figure 3.15. (a) The wide EELS spectrum with the Zero-loss peak, Plasmon peak and the edges of different elements. (b) Carbon edge at 284 eV and a very small Pd edge at 330eV (c) Cu doublet at 930 eV and 950 eV (d) Pre-edge (Figure d(i)), Post edge image (Figure d(ii)) and Cu mapped in an EFTEM image from a Pd:Cu sample (Figure d(iii)).

and the third image shows a Cu-map in a sample containing Pd, Cu, sulfur and organic materials. The spatial resolution of the EFTEM images is less than that of the HRTEM but it is still a very useful technique for chemical characterization of immiscible alloy samples.

3.5 Other experimental techniques

Atomic Force Microscopy (AFM) and X-ray photoelectron spectroscopy (XPS) were also used to study the morphology and the composition of the nanoparticle samples examined in this study.

3.5.1 Atomic force microscopy (AFM)

This method is used to observe the morphology of the nanoparticles after being deposited and annealed on a substrate. Size and morphology of the supported nanoparticles were monitored by atomic force microscopy. AFM can be used to measure van der Waals, friction, capillary, chemical bonding and solvation forces.

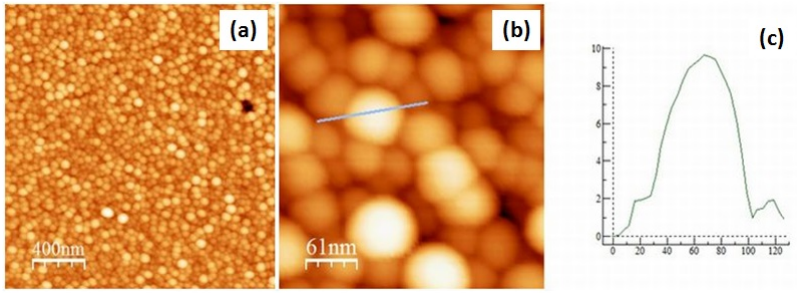

Figure 3.16. AFM images of a PtNiFe nanoparticles sample (a) Lower magnification (b) Higher magnification to measure size of nanoparticles as shown in (c).

Tapping mode of imaging was used to ensure minimum destruction of the sample. Standard silicon SPM probe of force constant 45N/m with a resonant frequency of 325 kHz was used. It has a tip radius <10nm attached to a cantilever of dimensions 3.4X1.6X0.4mm. The atomic force microscopy imaging was carried out using a Veeco Dimension 3100 AFM at the Birck Nanotechnology Center at Purdue University. The typical resolution was 1-5nm; maximum scan size was 90 micron in the x-y range and 5 micron in z-direction. WSxM software was used to analyze the images, including the average morphological height of the sample, surface roughness of the substrates,

sticky or non-sticky surfaces, etc. The AFM data was utilized to check the morphology and size of our nanoparticles. Figure 3.16 shows the data acquired from an AFM of a PtNiFe nanoparticles sample.

3.5.2 X-ray photoelexctron spectroscopy (XPS)

XPS is a surface technique used to study the elemental composition, chemical and electronic state of the materials probed. This technique makes use of light induced electron emission and photoelectric effect. XPS can detect all elements with Z greater than 3 (lithium) and the minimum amount of material required for detection is one part per thousand range. Organic materials are not analyzed by XPS because the high energy X-ray beam can damage the sample. XPS uses x-ray to irradiate the first 10nm of the material surface in ultra-high vacuum conditions. The kinetic energy of the electrons and the number of electrons are measured by XPS.

The XPS measurements were done on Kratos Axis Ultra DLD at BNC, Purdue University, using a Monochromatic Al K (1486.6 eV) x-ray source. XPS uses the Auger process to detect elements in the samples. This process involves filling of a core shell vacancy (when a core electron is removed) by another electron in the atom and emission of an electron from the same atom. Photoemission involves photon absorption and ionization, atom and neighbor response on photoelectron creation and photoelectron escape from the atom to the surface. The binding energy of the atom is the difference in energy between the state with n electrons and (n-1) electrons and free photoelectron. The photoemission has left a core hole in the atom after the photoelectron has escaped. This is followed by relaxation due to delocalization of the hole by the rearrangement of electrons in the orbital of the atom or its neighbors. Each element of the periodic table has a unique electronic structure and the electrons are emitted with specific kinetic energies. The emission lines are well tabulated and there are webpages like the NISTs XPS Database dedicated to the tabulation of the emission lines recorded so far. XPS data consists of intensity of the photoelectron (counts per

seconds) versus binding energy (eV). The peaks in the spectrum correspond to a particular element and the spectrum can be analyzed for the chemical content of the sample, oxidation states of an element, coverage and thickness calculations. Figure 3.17 shows a XPS spectra obtained for a Pd-Cu alloy nanoparticles sample.

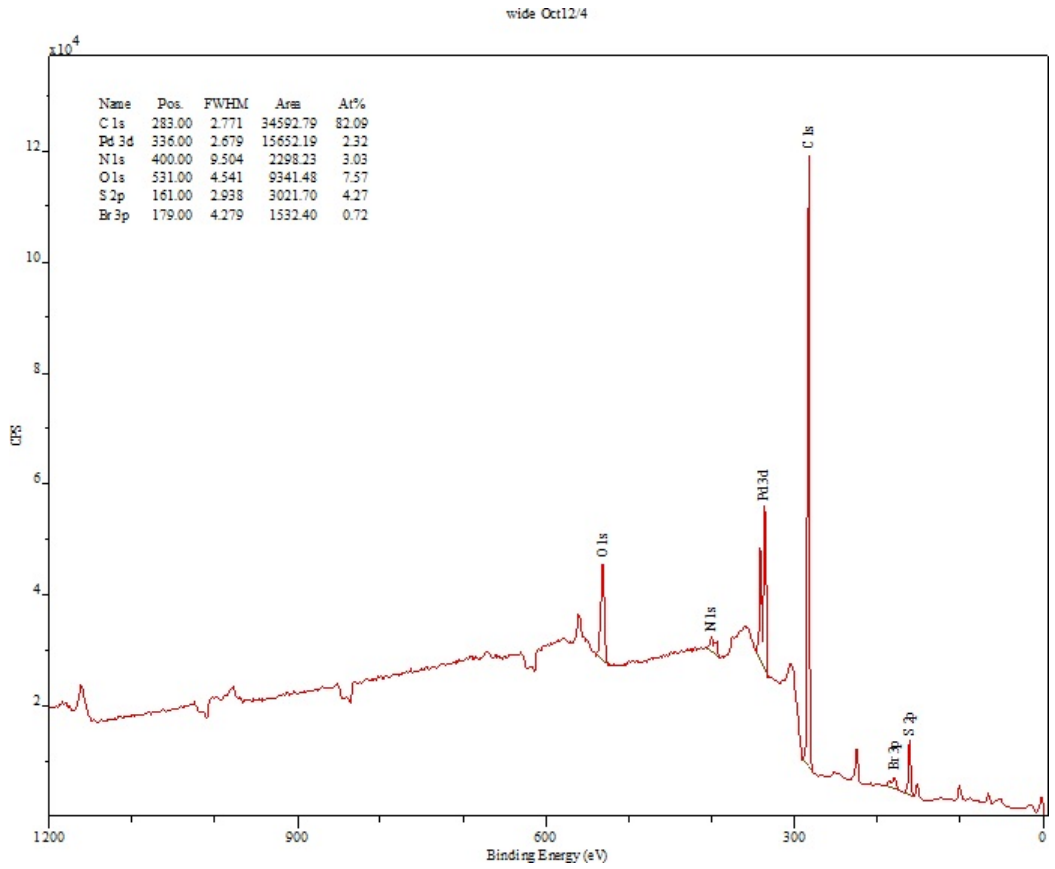

Figure 3.17. Typical XPS data along with the elemental compositions of a PdCu nanoparticles sample.

4. LIMITED GRAIN GROWTH AND CHEMICAL ORDERING DURING HIGH TEMPERATURE SINTERING OF PtNiCo NANOPARTICLE AGGREGATES

4.1 Introduction

Controlling nanoscale structure through relatively simple physical processes is a major problem in nanotechnology. Since most of the unique chemical properties of nanoparticles can be associated with specific structural properties, this is a problem of broad interest in practical applications ranging from metallurgy to electronics and catalysis [107].This chapter investigates high-temperature induced structural changes in Pt-based multi-metallic nanoparticles of interest in catalysis. Pt-containing bimetallic and trimetallic nanoparticles have been proven to exhibit remarkable catalytic properties that make them promising candidates to replace traditional bulk catalysts in fuel cell applications [2, 107–110]. Platinum is the material of choice for traditional catalysts [111]. However, Pt is expensive and in short supply world-wide. Therefore, designing catalysts with reduced Pt/noble metal content but with comparable or superior catalytic properties is of extreme importance for a variety of fields involving catalysis. In particular the availability and success of fuel cell technology critically depends on our ability to further improve catalyst performance and reduce the catalyst cost that currently amounts to as much as 30% of the fuel cell cost. Most noteworthy, some ternary nanocatalysts (i.e. PtVFe, PtNiFe), have been found to exhibit catalytic activities in fuel cell reactions that are 4-5 times higher than that of pure Pt catalysts [112]. PtNiCo binary and ternary nanoparticles, such as the

compositions examined in this chapter, also have great potential for applications in proton-exchange membrane fuel cells (PEMFCs) [**?**].

It is fairly well known that nanocrystalline materials undergo sintering upon high-temperature treatment. Depending on the application, sintering may be desirable for densification purposes, or may be deleterious because it leads to particle growth [113]. Due to interest for metallurgical applications, sintering in nanocrystalline materials has been investigated more intensively than sintering in nanoparticle aggregates. The exact mechanisms of high-temperature coalescence and size growth in Pt-alloy nanoparticle ensembles are relatively poorly understood at this point. Significant work has been done to study sintering of Au nanoparticles at room temperature [114, 115] but the work on Pt nanoparticle has been limited to pure Pt at room temperature [116].

Relatively little is known about high-temperature sintering of nanoparticle aggregates in general and in particular about sintering of Pt-alloy nanoparticles. Pt-containing multi-metallic nanoparticles present some specific challenges related to their complex phase diagrams and high melting temperatures. Recently, the importance of sintering in determining the properties of nanoparticle catalysts has come into focus [117]. Nanoparticle catalysts are routinely thermally treated to achieve optimal catalytic properties. During this thermal treatment the nanoparticles undergo little understood structural changes, such as phase and size changes, that affect their performance. For example, the enhanced electrocatalytic activity of PtNiCo trimetallic nanoparticles has been attributed to high-temperature induced structural changes such as lattice shrinkage and composition changes [110]. Moreover, presently there are no quantitative predictive tools that would allow rational design of nanoparticle processing in order to control nanoscale structure and implicitly properties.

This chapter attempts to explain and quantify the high-temperature induced structural changes in PtNiCo bimetallic and trimetallic nanoparticle aggregates. Synchrotron-based *in situ* time-resolved x-ray diffraction (XRD) is used to probe the evolution of PtNiCo nanoparticles aggregates on planar silica substrates. The high-flux of the

synchrotron x-ray source is not only convenient because it drastically reduces characterization time, but absolutely necessary to examine the fine structural details of the small volumes of nanomaterials. The synchrotron x-ray source offers the advantage of providing statistically relevant information for process control in macroscopic samples, information that is complementary to the information on isolated particles available from room-temperature TEM measurements. Moreover, the *in situ* XRD measurements have the ability to probe the early stages of the process by following the processes in real time with second time-scale resolution at temperatures inaccessible with any other *in situ* techniques (up to $950°C$). The binary and ternary Pt-alloyed nanoparticles aggregates were found to undergo complex structural transformations that involve sintering, lattice contraction, and $L1_0$-type chemical ordering upon annealing at high temperatures. A model for the structural evolution of the nanoparticles in the early stages of the sintering process is proposed. The grain growth in the late stages of sintering is examined in detail and compared with available theoretical models.

4.2 Experiments - Synthesis, instrumentation and measurements

4.2.1 Nanoparticle synthesis

PtNiCo, PtCo, and PtNi nanoparticles of various compositions were synthesized by a combination of molecular encapsulation, reduction/decomposition, and thermal processing protocols [109, 110]. The various compositions were obtained by manipulating the relative concentrations of metal precursors such as platinum(II) acetylacetonate, nickel(II) acetylacetonate, and/or cobalt(III) acetylacetonate and capping agents such as oleylamine and oleic acid. The details of the procedure are described elsewhere [109, 110].

The compositions of bimetallic and trimetallic nanoparticles were measured with Direct Current Plasma Atomic Emission Spectrometry (DCP-AES). The as-synthesized nanoparticles examined in this chapter are summarized in Table I. Figure 4.1 shows

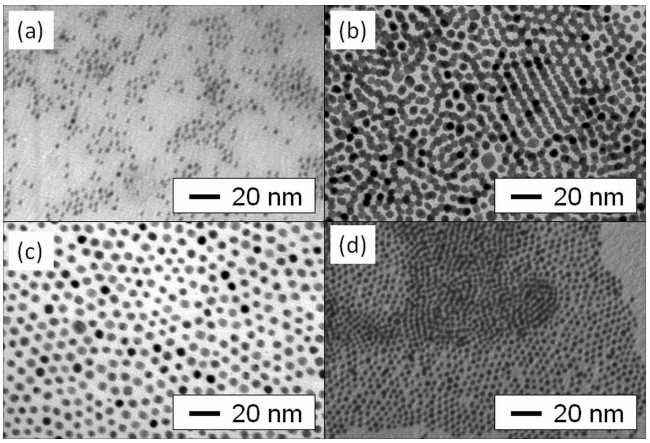

Figure 4.1. TEM of PtNiCo nanoparticles (a) $Pt_{28}Ni_{18}Co_{54}$ (b) $Pt_{44}Ni_{14}Co_{42}$ (c) $Pt_{33}Ni_{27}Co_{40}$ (d) $Pt_{34}Ni_{16}Co_{50}$.

the TEM images of the PtNiCo as-synthesized nanoparticles deposited on carbon grids. The thickness of the nanoparticle aggregate films varied from sample to sample between 100 and 600 nm.

4.2.2 Nanoparticle thermal processing and characterization

Previous work in our group investigated temperature-induced phase and morphology transformations of Au-based alloy nanoparticles on oxide substrates, carbon-black, and Si substrates [118–120] at relatively low temperatures. This chapter focuses on an investigation of the as-synthesized PtNiCo, PtCo, and PtNi nanoparticles on Si substrates annealed at relatively high temperatures. The samples were at room temperature for 30 seconds and then annealed to high temperature of 800 - 900$^{\circ}C$ on samples as specified in the table 4.1. The details of the XRD set up were detailed in chapter on experimental techniques.

Table 4.1.
Summary of the nanoparticle samples examined in this study

Sample	Size Initial (nm)	lattice constant Initial (A)	T (C)	Lattice Constant (Annealed) (A)	Random Alloy Lattice Constant(A)
$Pt_{34}Ni_{16}Co_{50}$	3.0 ± 0.4	3.899	900	3.853	3.67
$Pt_{28}Ni_{18}Co_{54}$	2.6 ± 0.3	3.813	800	3.733	3.64
$Pt_{44}Ni_{14}Co_{42}$	5.7 ± 0.3	3.813	900	3.716	3.71
$Pt_{33}Ni_{27}Co_{40}$	6.1 ± 0.3	3.836	850	3.747	3.66
$Pt_{58}Co_{42}$	2.5 ± 0.2	Non-cryst.	800	3.867	3.76
$Pt_{36}Ni_{64}$	1.5 ± 0.3	3.806	450	3.701	3.66

4.2.3 *In situ* time resolved XRD

It is noteworthy that the as-synthesized ternary Pt-Ni-Co nanoparticles exhibit an unusual grain asymmetry. Using the $\omega - 2\theta$ symmetric scans, we found that the particles are 10-30% larger in the (100) direction than in the (111) direction, due to either shape asymmetry or to stacking faults in the (111) direction. This morphology contrasts to the shape of other nanoparticles we have studied in the past (i.e. Au, Pt, AuPt, etc. [118, 120, 121]) and appears to be more pronounced for the smaller nanoparticles. The asymmetry reverses upon high-temperature annealing, leading to a (111)/(200) grain size ratio greater than one, similar to the size ratio commonly observed in other nanoparticle systems. The as-synthesized grain asymmetry seems to be related to the presence of Ni in the alloy, because a similar asymmetry is observed in $Pt_{36}Ni_{64}$ nanoparticles, but not in the $Pt_{58}Co_{42}$ or $Pt_{73}Co_{27}$ nanoparticles.

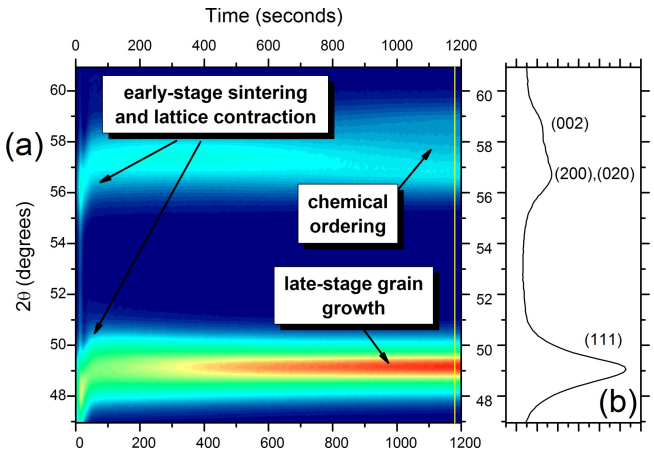

Figure 4.2. Overview of the temperature induced transformations in PtNiCo aggregates. (a) Time evolution of the XRD pattern for a $Pt_{44}Ni_{14}Co_{42}$ nanoparticle aggregate annealed at 700(Color map-red-high intensity; blue low intensity) (b)XRD spectrum at t=1200s showing cubic (111) and (200) peaks.t=0s represents the time the temperature was ramped from 100°C to 700°C at the rate of rate of 30°C/seconds.

4.3 Results and Discussion

The PtNiCo, PtNi, and PtCo nanoparticle were subjected to a series of successive thermal treatments in the temperature range between 400 and 950°C. The ternary PtNiCo nanoparticle aggregates undergo three types of structural changes upon thermal treatment: sintering, lattice contraction above 400°C, and chemical ordering below the orderdisorder transition temperature. The sintering process in nanocrystalline materials has been traditionally broken down into two main stages, a fast early stage, and a slow late stage. Figure 4.2(a) shows the time evolution of the XRD pattern of an aggregate of 5.7 nm $Pt_{44}Ni_{14}Co_{42}$ nanoparticles during isothermal annealing at 700°C. The color map was obtained from a time sequence of XRD patterns like the snapshot at 1200 s shown in figure 4.2(b). The main stages of the process (early versus late stage) and structural transformations (grain growth, lattice contraction, chemical ordering) are identified by arrows pointing to their experimental signatures (i.e. peak narrowing, peak shifting, and peak splitting, respectively). A TEM image

of the nanoparticles after thermal treatment at 850°C is shown in figure 4.3. The nanoparticles have been removed from the silica substrate and re-dispersed on carbon grids for TEM imaging. It is noteworthy that even though the size distribution after extensive annealing at high temperature is considerably broader than before heat treatment, the nanoparticles maintain their compact, roughly spherical shape without fusing into a continuous film. This post-treatment shape indicates relatively limited interactions between the nanoparticles. High-resolution TEM indicates that the particles less than 15 nm in diameter are typically single grain.

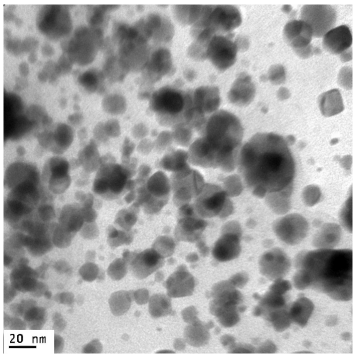

Figure 4.3. TEM of the $Pt_{44}Ni_{14}Co_{42}$ nanoparticles after annealing at 850°C for 20 minutes.

4.3.1 Early stages of sintering and lattice contraction

Theoretical models and computer simulations of isolated nanoparticle coalescence show this process to be driven by surface energy reduction [77,80,90,122,123]. Therefore, in the early stage of sintering in nanoscale aggregates, we expect the small as-synthesized nanoparticles to coalesce rapidly with their nearest neighbors through neck formation and growth. For the first time, we were able to experimentally capture the fine details of ternary alloy nanoparticle evolution in this early stage. In contrast to observations of single-metal nanoparticle sintering, the early stage coalescence of bimetallic and trimetallic nanoparticles is a complex process consisting of two distinct steps. Figure 4.4 shows the detailed XRD pattern evolution around the (111) and

(200) reflections in the early stages of isothermal annealing of $Pt_{44}Ni_{14}Co_{42}$ nanoparticles at 700°C shown in figure 4.2. This type of behavior appears to be unique to Ni-containing nanoparticles and is most pronounced in the binary PtNi nanoparticles. Figure 4.5 shows schematically a proposed model of structural evolution consistent with the XRD pattern evolution from figure 4.4.

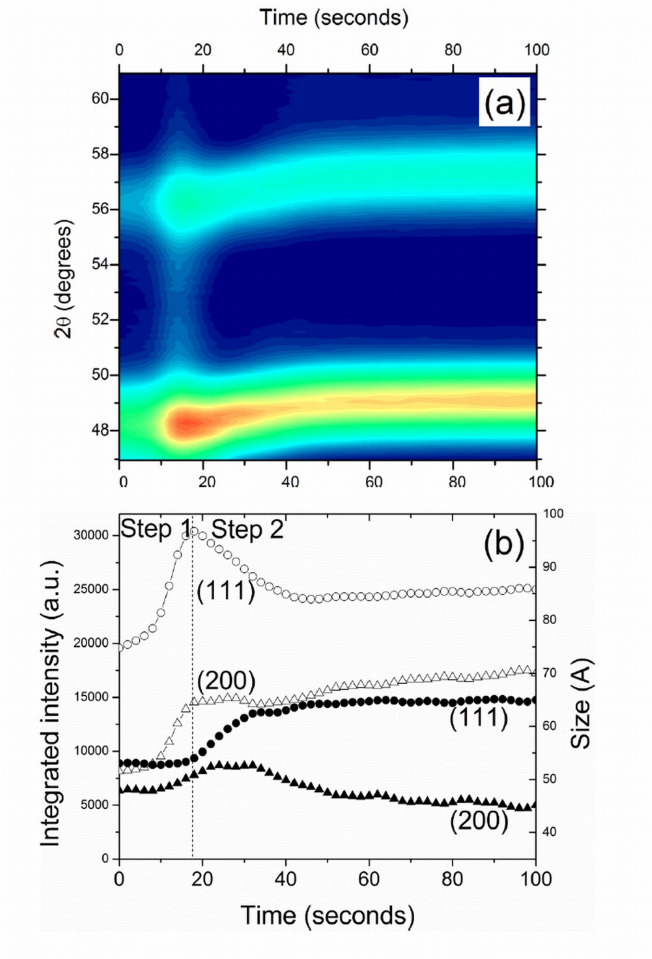

Figure 4.4. Kinetics of the early stage sintering of $Pt_{44}Ni_{14}Co_{42}$ nanoparticle aggregate annealed at 700C. (a) Color map of the time evolution of the XRD pattern. (b) Time evolution of the (111) and (200) intergrated intensity and (c) Time evolution of the (111) and (200) average grain size t=0 represents the time the temperature is ramped from 100°C to 700°C at the rate of 30°C/s.

The first step occurs mainly during the temperature ramp and is characterized by a dramatic increase of the (111) and (200) integrated intensities (up to 50%). We attribute this behavior to crystallization of a considerable fraction of the nanomaterial that was originally in a non-crystalline (i.e. amorphous or highly defected) phase. In this first step there is no significant increase of the average grain size (and sometimes there is a slight decrease of the average grain size), indicating that the newly crystallized regions are relatively small compared to the average particle size, and not coherently attached to the originally crystalline nanoparticles (figure 4.5). However, the surface of the crystalline nanoparticles may act as a source of heterogeneous nucleation sites for the non-crystalline particles. This hypothesis is supported by the rapid subsequent evolution of the nanoparticles.

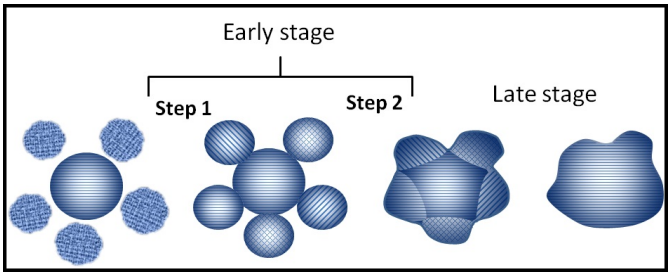

Figure 4.5. Model for the structural evolution during nanoparticle coalescence and sintering

The newly crystallized particles/structures are unstable to some extent as indicated primarily by the decay of the (111) integrated intensity in the second step (figure 4.5). This process may be due to coalescence of the small with the large nanoparticles through surface diffusion and is likely driven by surface energy minimization. The overall (111) grain size growth in the early stage is relatively small (from 5.3 to 6.5 nm) but measurable and occurs predominantly in the second step, indicating that it is due to a large extent to mass redistribution at the expense of the small structures.

The initial growth and drop of the (111) integrated peak intensity may also be attributed to development and subsequent decay of (111) preferential orientation (i.e. texture). While transient texture would be interesting on its own, we do not think

texture formation plays a significant role in these relatively thick (>200 nm), loosely bound aggregates (see also figure 3). In fact, we do have experimental evidence that thin (<100 nm) $Pt_{34}Ni_{16}Co_{50}$ and $Pt_{28}Ni_{18}Co_{54}$ nanoparticle aggregates develop significantly enhanced (100)preferred orientation in the late stages of the annealing process at 950°C, probably due to interactions between the nanoparticles and the substrate. More investigations are currently being done to identify the exact conditions for texture formation. The average lattice constant of as-synthesized PtNiCo and PtNi nanoparticles is typically larger than the value expected for a random alloy (solid solution) as shown in table 4.1, indicating that the particles are strained likely due to composition non-uniformities. Upon annealing at temperatures above 450°C the lattice undergoes a contraction reflected in the decrease of the average lattice constant towards the random alloy value. This effect is independent of particle size, particle density, and the presence of chemical ordering discussed below. The lattice constant decrease was within the experimental error (±2%) for the PtCo nanoparticles.

4.3.2 Late stage sintering and grain growth

Late-stage growth with significant grain growth is found only for annealing above 700°C. Figure 3 shows the TEM of $Pt_{44}Ni_{14}Co_{42}$ nanoparticles after annealing at 850°C for 20 min. This represents 54 to 58% of the bulk melting temperature, or 75% of the melting temperature corresponding to 2 nm diameter nanoparticles. No evidence of volume melting of the nanoparticles was found up to 950°C even for the smallest particles, most likely because sintering leads to significant particle growth long before the particles can reach their size-dependent melting temperature.

Several models developed for sintering in polycrystalline materials were tested for adequacy in reproducing the time evolution of nanoparticle aggregates. Grain growth in polycrystalline materials has been most often described by the generalized

parabolic (power) model [124, 125]. The growth is considered normal if the grain size follows an expression of the form

$$D^n - D_0^n = k_1 t \tag{4.1}$$

where D is the grain size at time t, D_0 is the initial grain size, n is the growth exponent, and k_1 is a constant that depends on temperature. For bulk materials the domain size is driven by domain boundary curvature and consequently the growth exponent takes the value 2. For nanocrystalline materials, the growth exponent was found to take values from 1 to 10. In most practical cases, however, the grain growth slows with time as reflected in an increase of the growth exponent, and the size eventually saturates.

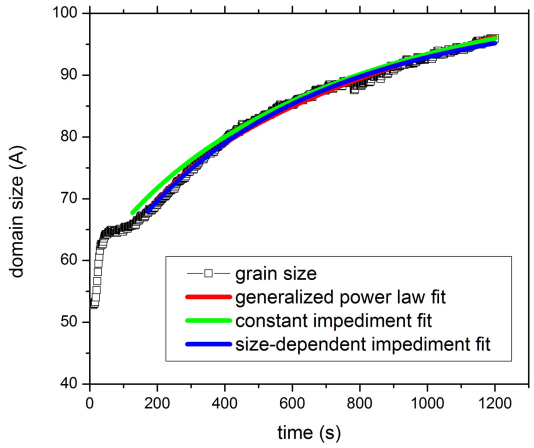

Figure 4.6. Time evolution of (111) grain size for the $Pt_{44}Ni_{14}Co_{42}$ nanoparticles annealed at 700°C and fits of the data described in the text. T=0 represent the time the temperature was ramped from 100°C to 700°C at the rate of 30°C/s.

To account for size saturation several authors introduced the concept of grain growth with impediment [124, 125]. If the impediment is constant, the grain growth is described by the following law:

$$k_2 t = \frac{D_0 - D(t)}{D_\infty} + ln\left(\frac{D_\infty - D_0}{D_\infty - D(t)}\right) \tag{4.2}$$

Where D_∞ is the saturation size, D_0 is the initial grain size and k_2 is another temperature-dependent constant. If the impediment depends on the size of the grains then the parabolic law is modified as follows to include saturation effects [126]:

$$D^2(t) = D_\infty^2 - \left(D_\infty^2 - D_0^2\right) \exp\left(-k_3 t\right) \tag{4.3}$$

If the diffusivity obeys an Arrhenius law with an activation energy E, then

$$a_{2,3} = T k_{2,3} D_\infty^2 \propto exp\left(\frac{-E}{RT}\right) \tag{4.4}$$

Grain growth in PtNiCo, PtCo, and PtNi nanoparticle aggregates was fit with all three growth law candidates as shown for one example in figure 4.6. All three models provide a reasonable quantitative description of the data, within experimental error. The generalized power law leads to relatively large values of n (n = 5.5 for the example in figure 4.6). The growth with constant impediment and the size-dependent impediment adequately describe the saturation of the grain size, but the latter was found to better capture the early time growth for all temperatures. An attempt was made to plot the temperature dependence of the coefficient a_3 for all measured Pt-based nanoparticle aggregates, but no single line can fit all the data, even for a single alloy composition. However, the data seem to cluster on two lines that were fit separately to calculate the activation energies. The error in the determination of k_3 is too large for a reliable estimate of the activation energy, but the two data sets are consistent with similar activation energies of the order of 100 kJ/mol (100 kJ/mol, and 120 kJ/mol, respectively). This value is consistent with the activation energy estimated by Natter et al for grain-boundary self-diffusion in nanocrystalline Fe [125]. The underlying cause for the clustering of the data on two lines deserves further investigation. At this point, we can only speculate that the different behavior of nominally identical samples is related to different local geometry (packing) of the nanoparticle aggregate due to different concentration of organic additives.

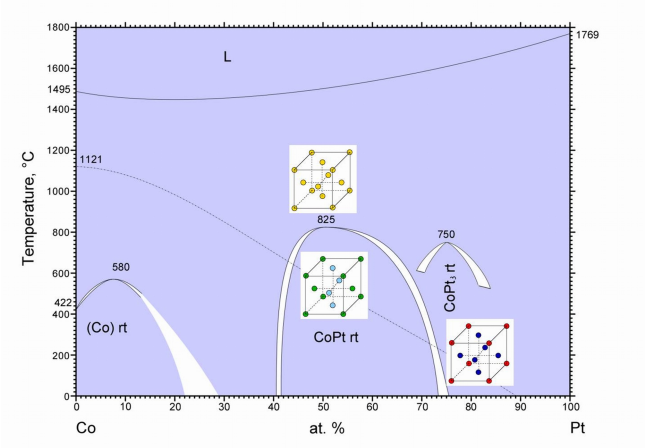

Figure 4.7. Pt-Co phase diagram showing the ordered phases.

4.3.3 Chemical ordering

The binary phase diagrams of bulk PtCo and PtNi alloys show chemically ordered structures at temperature below a composition-specific transformation temperature. For example, the $Pt_{50}Co_{50}$ alloy orders in the CuAu-I ($L1_0$) structure below 825^{circ}C (figure 4.7). Above this temperature the Pt and Co atoms are distributed randomly on the fcc lattice (solid solution). Below 825^{circ}C, the alloy develops long-range ordering characterized by alternating layers of Pt and Co atoms along the c-direction (see figure 4.7). The chemical ordering is accompanied by a tetragonal distortion (i.e. the ratio of the lattice constants $c/a \leq 1$). Pt50Ni50 exhibits a similar ordering transformation, but the transition temperature is significantly lower than for PtCo (658°C). The phase diagram of the bulk ternary alloys PtNiCo has not been studied in detail so far, but it is natural to assume that the ternary alloys will exhibit similar chemical ordering trends. The long-range chemical ordering leads to symmetry breaking in the lattice and consequently to the emergence of new diffraction peaks called superlattice peaks. (100) and (110) are two such superlattice peaks, whose presence in the diffraction pattern indicates chemical ordering. We found $L1_0$ type ordering in all four ternary alloy nanoparticles studied after annealing at 700°C for grain sizes as small as 4 nm (figure 4.8). The tetragonal distortion was generally found to be slightly smaller than

in the bulk materials (0.97), likely due to incomplete ordering. The orderdisorder transformation occurs around 800°C, which is slightly higher than the composition-weighted transition temperature (about 770°C). Therefore, annealing above 800°C results in formation of a random alloy. This random alloy survives moderately fast subsequent cooling to room temperature due to nucleation suppression. Therefore most nanomaterials of practical interest in catalysis annealed above 800°C are most likely random alloys.

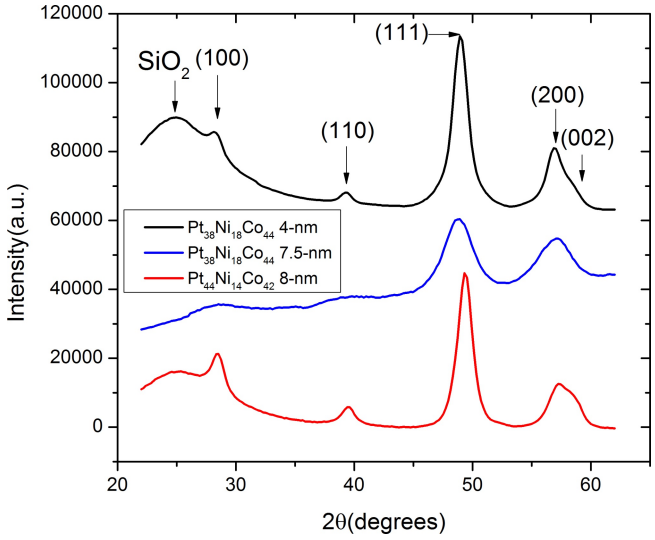

Figure 4.8. Evidence of ordered structures in PtNiCo nanoparticles aggregates of different sizes and compositions annealed below 800°C.

4.4 Conclusions

In conclusion, *in situ* real-time x-ray diffraction was used to examine the high-temperature (>700°C) structural transformations of ternary PtNiCo nanocatalysts and to compare them with the binary PtCo and PtNi nanoparticles. The early stage coalescence of the nanoparticles was found to be a two-step process involving rapid growth followed by decay of transient, possibly metastable structures. The latter step is accompanied by lattice contraction likely due to composition evolu-

tion towards a random alloy. The exact nature of these metastable structures is not completely understood at this point, but a model was proposed involving recrystallization of initially amorphous nanoparticles. The enhanced electrocatalytic activity of annealed PtNiCo trimetallic nanoparticles may be due to these high-temperature induced structural changes (i.e. lattice shrinkage and composition changes) [110]. Extended thermal treatment of PtNiCo nanoparticles was found to lead to relatively limited size increases, the average grain sizes remaining below 10 nm even at the highest temperatures probed (up to 950°C). This property points to the synthesis of nanocrystalline materials from colloidal particles as an alternative fabrication method when maintaining the nanoscale grain size is important for maintaining physical properties. In the probed time regime, the grain growth is sufficiently well described by the law for grain growth with size-dependent impediment. Therefore this growth law may be employed as a useful predictive tool to roughly estimate the size of the particles as a function of annealing temperature and time. However, to further clarify the behavior of the nanoparticles on longer time scales, further experimental investigations are needed and are currently being planned. An activation energy of about 100 kJ/mol was derived, a value that is consistent with grain-boundary self-diffusion as the dominant process for grain growth. However, the temperature dependence of the a_3 growth coefficient indicated that there are two distinct sintering mechanisms possibly associated with the morphology (packing geometry) of the nanoparticle aggregate. Formation of $L1_0$-type chemical ordered structures was observed below the orderdisorder transformation temperature of about 800°C. This little explored ordered structure may also affect the catalytic properties of the nanoparticles.

5. NANOALLOYING AND PHASE TRANSFORMATIONS DURING THERMAL ANNEALING OF Pd AND Cu NANOPARTICLE MIXTURES

5.1 Introduction

The study of multi-metallic nanoparticles is an active area of research due to the flexibility to tune nanoparticle properties for various applications through manipulation of their structure and composition. Metallic nanomaterials have a wide range of applications from electronics to catalysis. In particular the surface structure, composition distribution and ordering properties of nano-scale alloys are of interest as they play a major role in determining the chemical reactivity and selectivity of nanoparticle catalysts. To date, wide spread commercialization of fuel cells is hindered by the high cost of the platinum catalysts. Nanoalloy catalysts are promising alternatives to bulk noble metal catalysts like Pt and Au. Pd has lower activity when used as a catalyst in fuel cells but when combined with transition metals, the resulting alloy activity becomes comparable with that of Pt-based catalysts [127]. The influence of metals such as Fe, Cu, Co, Mn and Mo on the catalytic performance of Pd in many chemical reactions was reviewed by Coq et al. [128] and Wang et al. [129]. Bimetallic Pd nanoparticles have also been found to be good catalysts in hydrogenation reactions and as hydrogen storage materials. Interestingly, the Pd/Cu alloys were found to be resistant to H_2S poisoning when they have an fcc structure. Pd membranes also enhance efficiency and reduce costs in the coal gasification process [130]. Finally, PdCu alloys have applications in oxygen-assisted water gas shift reactions [131] and selective hydrogenation of dienes [132].

Thermal annealing is an important step for the activation and stabilization of nanoscale catalysts. Since catalytic activity is promoted by active sites which in turn

can be controlled by size, morphology, and composition distribution, to enhance the electrochemical activity, the nanocatalysts are typically heat treated in various atmospheres. At high temperature, the nanostructures undergo phase reconstructions, phase transformations, morphological and size changes that result in modified electronic band structures. In particular, the alloy formation, composition and structure are dictated by this post-preparation treatment. Alloying has been studied extensively in bulk multimetallic systems. Yet, alloying is not fully understood in nanoparticles systems. Oftentimes annealing of nanoparticles leads to limited alloy uniformity and the presence of multiple alloy phases. The alloy phases become more uniform with longer annealing times and higher temperature, but the process is typically accompanied by inevitable sintering resulting in larger particle size.

The alloying process depends mainly on composition and temperature. In the case of multi-metallic nanoparticles, however, the synthesis method was also found to play a major role for catalysis properties. For example, carbon-supported PdCu bimetallic nanoparticles with composition ratio ranging from 1:9 to 9:1 synthesized by co-impregnation were surveyed by Wang et al. in the temperature range 300C to 800C [129]. They reported the highest electrochemical activity for molar ratios of 1:1 and 1:3 heat treated at 600C. Kairuki et al. [133] explored organic monolayer stabilized alloy PdCu nanoparticles having a composition ratio of 1:1 and 1:3 synthesized by colloidal preparation method. The random solid solution alloy structure for a bimetallic composition of Pd:Cu =1:1 exhibited higher mass activity for electrochemical oxidation of methanol. The (1:1) PdCu/C mass activity was also found to increase with the increase in heat treatment and particle size. In a recent study [134], as-synthesized PdCu nanoparticles supported on carbon were also shown to exhibit enhanced electrocatalytic activity in alkaline electrolyte in comparison with pure Pd. The observed difference of the electrocatalytic properties was attributed to the surface enrichment of Pd on the alloyed PdCu surface [134].

A review of the literature shows that the nanoparticle structure is sensitive not only to composition, temperature, and preparation technique, but also to annealing

atmosphere. Using high-angle annular dark-field scanning transmission electron microscopy (HAADF-STEM), Yin et al. [135] found that $Pd_{85}Cu_{15}/C$ nanoparticles are crystalline with a random solid-solution structure while $Pd_{39}Cu_{61}/C$ nanoparticles have a chemically ordered PdCu structure along the [110] axis after annealing at 400C in an inert atmosphere. Using transmission electron microscopy (TEM) and extended x-ray absorption fine structure (EXAFS), Mattei et al. [136] studied the 3:1 Pd:Cu solid solution obtained by sequential ion implantation in silica in selected atmospheres of air and forming gas. They identified migration of Pd atoms to the surface and formation of large clusters when the material was annealed in a reducing atmosphere. When the nanoclusters are annealed in air, Cu oxidizes to CuO and forms a partial shell around a Pd-rich core. The atomic ratio of Pd/Cu was also found to depend on the implantation range.

Last but not the least, the structure of nano-sized bimetallic nanoparticles depends on the nature of the support. Supported metal particles are ideal candidates for investigating support-related properties and effects. The support-nanoalloy interaction influences structural and chemical ordering in the nanoparticles, and may influence the formation of active sites on the nanoalloys for catalysis. Strukul et al. [137] reported on the activity of Pd on Cu-alumina supports. Sun et al. [138] used electron energy loss spectroscopy (EELS) and X-ray energy dispersive spectroscopy (EDS) with scanning transmission electron microscopy (STEM) to conclude that the final structure is dependent on metal loading and specific reduction processes. They had studied the PdCu nanoparticles at 523 K, 773 K and 1073 K and there was no evidence of formation of the expected ordered B2 phase. At 523 K and 773 K, the nanoparticles had compositions ranging from pure Pd to PdCu alloys. On further reduction at 1073 K, PdCu alloys with either Pd or Cu rich surfaces were formed.

Considerable work has been done to study the structural evolution of PdCu alloy nanoparticles. This chapter focuses on nanoscale alloying via thermal evolution of mixtures of ultrafine Pd and Cu precursor nanoparticles. The Pd:Cu molar ratio is nominally 1:1 and the temperature range monitored is $25°C$ - $700°C$. The fast

phase transformations at the nanoscale are probed with synchrotron-based *in situ* x-ray diffraction (XRD). We have previously demonstrated the utility of this technique for unraveling the phase and morphological transformations in other binary and ternary nanoparticles including AuPt, PtNiCo and AuCu [118, 119, 139]. The XRD experiments are complemented with ex-situ transmission electron microscopy. The nanoscale alloying and the time evolution of Pd:Cu nanoparticles mixtures on various surfaces (SiO2/Si, Carbon and alumina) are examined in Helium and forming gas atmospheres. The structural evolution of Pd:Cu nanoparticle mixtures dispersed on SiO2/Si and carbon annealed in He and forming gas are qualitatively similar in nature. The Pd and Cu nanoparticle mixtures were found to form an ordered alloy phase with CsCl-type (B2) structure upon annealing at $300°C$. When annealed at $700°C$, the nanoparticles undergo a phase transformation from B2 to a disordered fcc structure. Surprisingly, though, the evolution of the nanoparticle mixture follows a different path for mixtures dispersed on alumina. In the latter case, the two metals segregate into Cu- and Pd-rich domains at $300°C$ and the B2 alloy structure was absent throughout the annealing process. Upon annealing at higher temperature, the two metals inter-diffused to form disordered alloys

5.2 Synthesis of Pd and Cu nanoparticles

The organic-monolayercapped ultrafine metal nanoparticles were synthesized by a combination of reduction/decomposition and thermal processing using metal precursors, reducing agents, and capping agents. The Pd and Cu nanoparticles capped with decanthiolate monolayers were synthesized separately according to the techniques detailed in [119, 140, 141] and the references therein.

5.2.1 Copper nanoparticles

The synthesis of decanethiolatecapped Cu nanoclusters was recently described in references [119,140]. In the modified synthesis, CuCl2 was dissolved in water (40 mM)

in the presence of 430mM of potassium bromide to convert Cu^{2+} to $CuBr_4^2$. This solution was then mixed with a solution of tetraoctylammonium bromide (TOABr) in toluene (40 mL toluene, 1 g TOABr) under vigorous stirring to induce a phase transfer of the $CuBr_4^2$ from the aqueous phase to the organic phase. After stirring for 45 min, the aqueous solution was removed, leaving a deep maroon colored organic phase. The copper toluene solution was stirred under an argon purge to eliminate all oxygen from the system. After purging for 30 min, 1.0 mL of decanethiol was added, causing the solution color to change from maroon to clear. Next, 10 mL of a solution of sodium borohydride in water (1 M) was added drop-wise to the solution. The solution became a deep cloudy orange, indicating the formation of copper nanoparticles. The solution was stirred under argon for 2 h. After removing the water layer, the Cu nanoparticles in the toluene phase were collected for further experiments.

5.2.2 Palladium nanoparticles

The synthesis of palladium nanoclusters was modified from Murrays protocol [141]. Starting from potassium tetracholoropalladate (K_2PdCl_4; 18 mM) as metal precursor dissolved in H2O, TOABr as the surfactant dissolved in toluene (125 mL toluene, 0.38 g TOABr) was added into the solution. After 1520 min stirring, $PdCl_4^2$ showing as deep red was transferred into the toluene phase, followed by the H_2O layer removal, 0.4 mL decanethiol was added to the toluene solution, turning the deep red to an orange color. Then 10 mL of a 0.45M solution of $NaBH_4$ in water was added drop-wise to the solution. The Pd nanoparticles in the toluene phase were collected after stirring overnight.

5.3 Results

The sizes of the as-prepared Pd and Cu nanoparticles measured with TEM were 1.8 ± 0.2 nm and 0.7 ± 0.2 nm, respectively. These Pd and Cu nanoparticles were extracted in an organic solvent like toluene. Inductively coupled plasma atomic emis-

sion spectroscopy (ICP-AES) analysis revealed the composition of the as prepared mixture to be 34% (Pd) and 66% (Cu).

First we present results for control samples of pure Pd and pure Cu nanoparticle samples supported on SiO2/Si and then we describe the behavior of Pd:Cu nanoparticles mixtures on different substrates and annealed in different atmospheres.

5.3.1 Control samples

The palladium nanoparticles are expected to coalesce and sinter to form bigger particles when annealed at high temperatures similar to the behavior observed for Au and Pt nanoparticles [118,119]. The smaller Cu nanoparticles, on the other hand, react with the alkanetiolate capping agent (dodecanethiol) to form Cu_2S nanodisks when annealed at relatively low temperature (≈ 140°C) [140].

Palladium nanoparticles

To study the behavior of single-metal Pd nanoparticles, they were dispersed on SiO2/Si substrates and isothermally annealed at 500°C in helium gas. The Pd nanoparticles were found to form larger Pd nanoparticles and a few compounds as shown in figure 5.1. The peak at 46.4° corresponds to the Pd (111) reflection. A survey of the $\theta - 2\theta$ scan shown in figure 5.1(b) done after annealing at $500°C$ suggests the formation of palladium sulfide (PdS), palladium oxide (Pd_2O), and palladium chloride ($PdCl_2$). The peaks at 43.2° and 50.3° correspond to the (111) and (200) reflections of Pd_2O. Pd_2O has a cubic structure with Pd occupying the corner of the cube while O atoms occupy the face centers. The calculated value of the lattice parameter of $4.22 \pm 0.01\mathring{A}$ was similar with the value for bulk Pd_2O $4.28\mathring{A}$ reported in the literature [142]. The data was also checked for the formation of the more common palladium (II) oxide (PdO) but none of the reflections in our data matched the expected PdO reflections. The peaks at 37.6° and 41.4° correspond to the PdS (201) and (211) planes, respectively, with a P42/m (tetragonal) space group and a lattice

parameter of 6.2$\mathring{A}$ that is consistent with expectations [143]. The remaining reflections at 48.1° and 57.3° likely correspond to the (112) and (114) planes of the $PdCl_2$ that has octahedral structure with Pnmn space group [143] and a lattice parameter of 3.81$\mathring{A}$. The formation of Pd_2O and PdS is likely due to the proximity reaction of Pd atoms with the capping molecules containing oxygen and sulphur. However, the formation of $PdCl_2$ is likely due to the presence of residual Cl from the metal precursor potassium tetra-chloro-palladate used to synthesize the Pd nanoparticles.

Copper Nanoparticles

The Cu nanoparticles on SiO_2/Si substrates were monitored during ramp annealing from 25°C to 225°C in helium gas (Figure 5.1(c)) and were found to form Cu_2S nano-discs. The diffraction data reveals peaks at 51.6°, 54.3° and 57.4° as shown in figure 5.1(d). The peak at 51.6° corresponds to the Cu (111) plane. The peaks at 54.6° and 57.4° correspond to the Cu_2S (110) and Cu_2S (103) reflections. Mott et al. [140] have previously reported that copper nanoclusters synthesized by the two-phase method react with the capping agent, alkanethiolate, to form copper sulfide nanodiscs in a thermally activated reaction. A similar behavior was seen in the evolution of the Au-Cu nanoparticle mixtures [119]. Yin et al. also observed that TOABr, the phase transfer catalyst, plays a role in the formation of the Cu_2S [144].

5.3.2 PdCu nanoparticle mixtures on SiO_2/Si

This study focuses on the structural evolution of Pd:Cu nanoparticle mixtures for 2 steps of thermal treatment: (1) Isothermal annealing at 300°C, and (2) Ramp annealing from 300°C to 700°C with the heating rate of 40°C/min. The evolution route of Pd:Cu nanoparticle mixtures is different from the temperature induced structural evolution of unary nanoparticles. The as-prepared nanoparticle mixtures have a bi-modal distribution peaked at 0.7 ± 0.2nm (Cu) and 1.8 ± 0.2nm (Pd) measured from counting more than 360 nanoparticles as shown in figure 5.2(a). The thermal

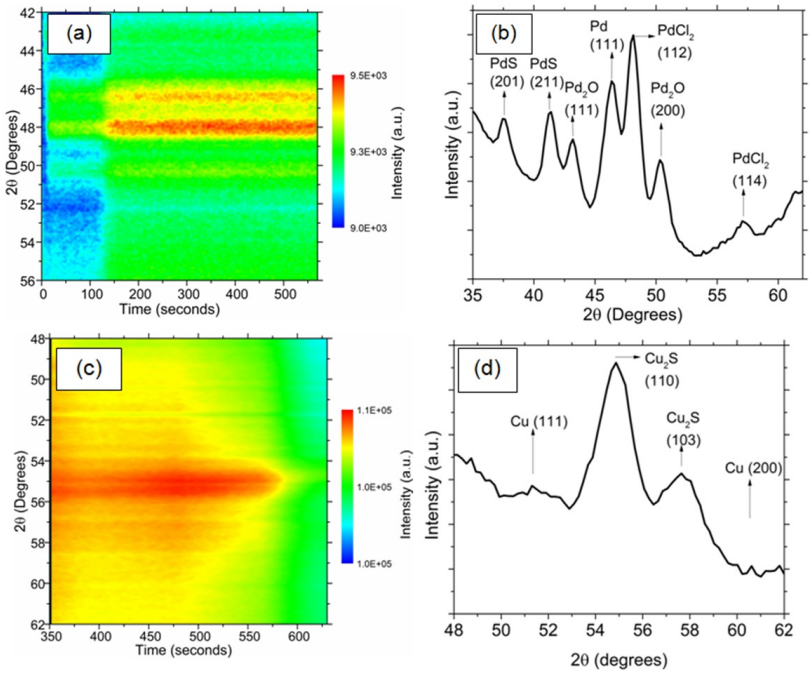

Figure 5.1. (a) Color map of the XRD intensity evolution for Pd nanoparticles annealed at 500°C on SiO2/Si support in He atmosphere. (b) $\theta - 2\theta$ XRD scan after the thermal treatment of Pd nanoparticles in (a). (c) Color map of the XRD intensity evolution of Cu nanoparticles dispersed on SiO2/Si ramped annealed from 25 to 225°C in He gas. (d) $\theta - 2\theta$ XRD scan after the thermal treatment of Cu nanoparticles in (c).

treatment leads to changes in structure and size. For example, the SiO2/Si supported Pd:Cu nanoparticles have TEM sizes of 11.3 ± 6.7 nm after annealing in He gas at 300°C as seen in figure 5.2(b). After annealing in He gas at 700°C, the analysis of TEM images as shown in figure 5.2(c) revealed an average particle size of 23.95 ± 12.3 nm.

The bulk Pd-Cu system has a complex phase diagram exhibiting several different ordered structures at different compositions [145]. From the phase diagram shown in figure 5.3, the Pd-Cu alloys with Pd% between 36-50% have an ordered Cs-Cl-type (B2) structure, also known as the β phase, at low temperatures and transform to a disordered fcc alloy at high temperatures. The formation of the B2 phase was

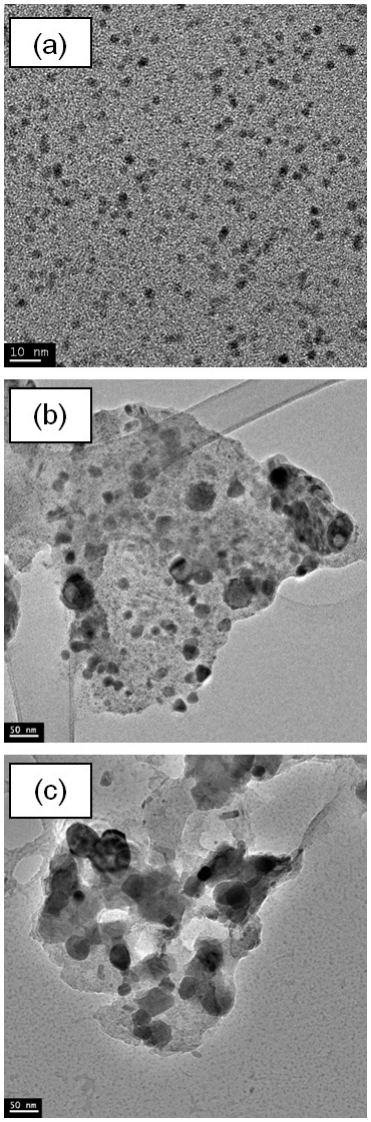

Figure 5.2. (a) TEM image of the as-synthesized PdCu nanoparticles mixture (scale bar is 10 nm). (b) TEM image of SiO2/Si-supported PdCu nanoparticles after annealing at 300°C in He gas (scale bar is 50 nm). (c) TEM image of SiO2/Si-supported PdCu nanoparticles after annealing to 700°C in He gas (scale bar is 50 nm).

reported also for Pd-Cu nanoalloys in several papers [130, 133, 134, 146]. If complete alloying occurs in the mixture, based on the composition established by ICP-AES for the as synthesized sample, we expect the Pd:Cu physical nanoparticle mixtures to behave as bulk alloys with Pd composition in the range from 36% to 50%.

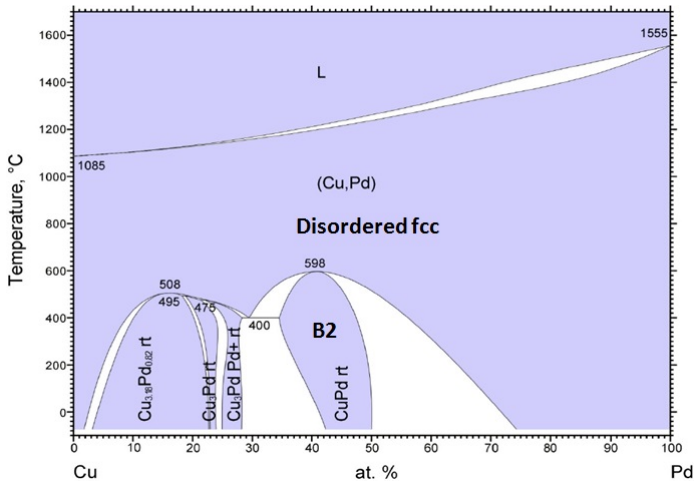

Figure 5.3. Phase diagram of bulk Pd-Cu [145]. Reprinted with permission of ASM International. All rights reserved. www.asminternational.org.

Annealing in Helium gas

We start by examining the Pd:Cu nanoparticle mixtures dispensed on SiO2/Si substrates and annealed in high-purity He gas. The analysis focuses on the changes occurring in the XRD peaks present in the angular range of 40° to 60° degrees. This range was chosen in order to monitor the strongest fcc Bragg peaks, (111) and (200). Figures 5.4(a) and (b) show the color map of the XRD intensity evolution in this range during the two thermal cycles. Figure 5.4(c) shows the expanded range of the $\theta - 2\theta$ scan taken at room temperature after each thermal treatment.

During isothermal annealing of the physical mixture of Pd and Cu nanoparticles at 300°C, we found a single dominant XRD peak growing at 51°. The fact that only one peak is visible in this range is important, because fcc structures have two peaks in this range corresponding to (111) and (200) reflections. For example, pure Pd nanoparticles have an fcc structure with a lattice parameter of 3.92 and exhibit peaks at 46.4° (111) and 54.9° (200) [133], while fcc Cu nanoparticles with a lattice parameter of 3.59$\mathring{A}$ exhibit peaks at 51.5° (111) and 60.5° (200) [133]. We attribute the single peak dominating the diffraction pattern in figure 5.4(a) and (c) to the

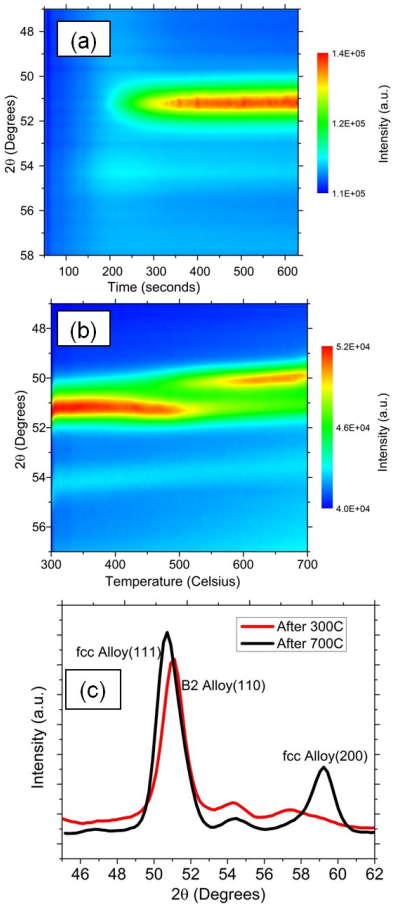

Figure 5.4. (a) Color map of the XRD intensity evolution for the Pd:Cu nanoparticle mixture on SiO2/Si substrate isothermally annealed at 300°C in a He atmosphere showing the formation of the ordered B2 phase. (b) Color map of the XRD intensity evolution of the Pd:Cu nanoparticle mixture on SiO2/Si ramped annealed from 300°C to 700°C in a He atmosphere showing the transformation of the B2 phase into a disordered fcc alloy phase. (c) $\theta - 2\theta$ XRD scans after annealing at 300°C and 700°C.

(110) reflection of the PdCu alloy B2 phase. The B2 phase has an ordered CsCl-type structure (space group $Pm3\bar{m}$) and exhibits a single (110) peak in the monitored angular range (lattice parameter of $2.95 \pm 0.15 \mathring{A}$) [146]. Unreacted Cu can be excluded even though the Cu (111) reflection partially overlaps with the B2 (110) reflection because the (200) fcc peak is absent. We also note the presence of other small peaks in the $\theta - 2\theta$ patterns (Fig. 5.4(c)) likely due to Cu_2S nanoparticles.

The formation of the ordered PdCu B2 phase during annealing of the nanoparticle mixture at 300°C (figure 5.4(a)) is evidence for alloying of Cu and Pd at the nanoscale. We note that the sample heating starts at time zero and that the temperature stabilizes at 300°C in less than 20s. Therefore, most of the transformation occurs at 300°C, rather than during the initial heating. The B2 phase growth becomes visible a significant time (more than 200 s in this case) after the sample has reached 300°C. This incubation time depends on the temperature and atmosphere of the annealing process. During this incubation time, the as-synthesized nanoparticles likely melt and coalesce. Given the small size of the as-synthesized nanoparticles, it is natural to assume that the first step of the process involves melting of the Cu and possibly even of the Pd nanoparticles. Unfortunately, our XRD technique is only sensitive to crystalline phases and does not provide quantitative information about intermediate amorphous or liquid phases. The mixing of the two metals likely occurs through diffusion of Cu from the surface of the larger Pd nanoparticles into their volume in the non-crystalline phase during the incubation time. The B2 phase then nucleates and grows into this noncrystalline alloyed phase.

Additional evidence for the formation of the B2 phase was obtained from high resolution TEM images. Figure 5.5 shows a PdCu nanoparticle after annealing of the mixture at 300°C. Fast Fourier transform from the marked particle is indexed as B2 structure with the orientation along [311] zone axis [146].

In the second thermal treatment the samples were ramp-annealed from 300°C to 700°C and a solid-state phase transformation from the ordered B2 to a disordered fcc structure was observed as shown in figure 5.4(b). The transformation takes place between 450°C and 500°C and the XRD data captures the decay and growth with accuracy. The new phase emerging is the disordered fcc alloy characterized by peaks at 50.3° and 58° pertaining to the (111) and (200) reflections, respectively. The lattice parameter from the XRD data was found to be $3.67 \pm 0.18\mathring{A}$, close to the value of $3.7\mathring{A}$ reported by Jones et al. [147].

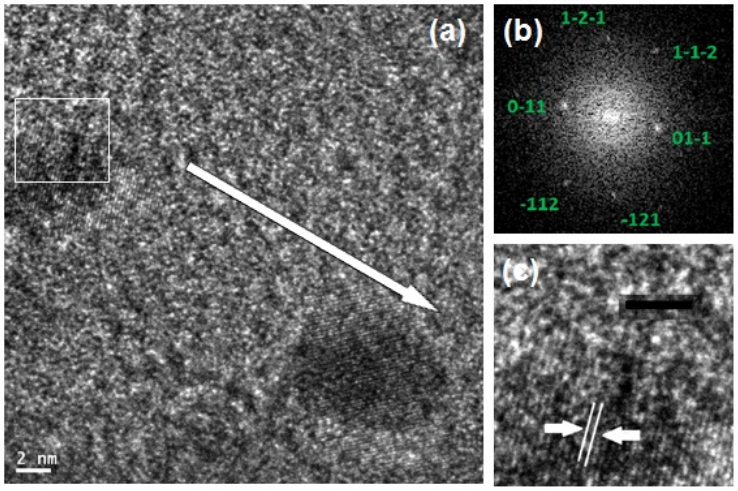

Figure 5.5. (a) TEM image of the Pd:Cu nanoparticle mixture after isothermal annealing at 300°C on SiO2/Si substrate in a He atmosphere. (b) The FFT from a marked area in (a) is indexed as [311] zone axis of the PdCu B2 alloy phase. (c) High resolution image of the PdCu particle marked in (a) reveals uniform lattice fringes across the particle with an inter-planar distance of 2.14$\mathring{A}$ that corresponds to [110] plane of B2 phase. Scale bars are 2nm and 5nm for images (a) and (c), respectively.

The lattice parameter of the fcc alloy formed after annealing at 700°C calculated from the XRD data was found to be 3.667$\mathring{A}$. Given the lattice parameters of Pd and Cu as 3.89$\mathring{A}$ and 3.61$\mathring{A}$, respectively, and assuming Vegards law (linear dependence of the alloy lattice parameter on the lattice parameters and alloy composition)143, the Pd fraction was estimated to be x=0.28 ± 0.03. This value is within experimental errors, but slightly lower than expected from measurements of the composition of the as-synthesized mixture by other techniques. This may be due to composition inhomogeneity that will be discussed later, or to the presence of small pure Pd and Cu nanoparticles that cannot be completely ruled out based on the XRD data alone.

The XRD crystalline domain sizes of the PdCu alloy nanoparticles were calculated with the Debye-Scherrer equation from *in situ* $\theta 2\theta$ scans measured after each thermal cycle and subsequent cooling to room temperature (figure 5.4(c)). The sizes were found to be 9.7 ± 0.5 nm and 14.4 ± 0.7 nm, after annealing at 300°C and 700°C ,

respectively. These values are representative because the XRD sizes do not change significantly after cooling to room temperature. We note that the XRD gives the coherently diffracting domain size that may be different from the particle size determined by TEM. TEM measures particle size, but the particles may consist of one or more crystalline domains. As mentioned above, we estimated an average TEM size of 11 ± 7 nm after annealing at 300°C (figure 5.2(b)), and an average particle size of 24 ± 12 nm after annealing at 700°C in helium (figure 5.2(c)). The good agreement between XRD and TEM sizes after annealing at 300°C indicates that the particles are mostly single-domain. After annealing to 700°C, there is a large difference between the TEM and XRD sizes, indicating that the particles contain more than one domain. The TEM images of these samples also showed the presence of nanorods, likely due to Cu2S formation. The large distribution of the nanoparticle sizes after annealing to 700°C is due to large-scale sintering and the difficulty in distinguishing between the PdCu alloy and other compound particles such as Cu2S. Further discussion of the time evolution of the particle sizes is given in the following section.

The lattice parameter of the fcc alloy formed after annealing at 700°C calculated from the XRD data was found to be $3.667\mathring{A}$. Given the lattice parameters of Pd and Cu as $3.89\mathring{A}$ and $3.61\mathring{A}$, respectively, and assuming Vegards law (linear dependence of the alloy lattice parameter on the lattice parameters and alloy composition) [105], the Pd fraction was estimated to be x=0.28 ± 0.03. This value is within experimental errors, but slightly lower than expected from measurements of the composition of the as-synthesized mixture by other techniques. This may be due to composition inhomogeneity that will be discussed later, or to the presence of small pure Pd and Cu nanoparticles that cannot be completely ruled out based on the XRD data alone.

Annealing in forming gas atmosphere

The nanoparticles annealed in forming gas display a behavior qualitatively similar with the samples annealed in helium gas. Specifically, the Pd:Cu nanoparticle

mixtures undergo the same structural transformations. As in the case of thermal treatments in helium gas, the samples were first annealed at 300°C (figure 5.6(a)) and then ramp annealed from 300 to 700°C in forming gas (figure 5.6(b)). Figure 5.6(c) shows the expanded range of the $\theta - 2\theta$ scan taken at room temperature after each thermal treatment, highlighting the presence of two structures, B2 structure and fcc structure after annealing at 300°C and up to 700°C, respectively.

The evolution of the B2 (110) peak integrated intensity and the XRD domain size at 300°C are shown in figure 5.6(e). The (110) integrated intensity is proportional to the B2 phase volume, or in other words to the degree of alloying. The incubation time is shorter than in the case of annealing in helium gas (< 100 s). Moreover, the growth of the ordered B2 domains is faster than in the case of annealing in helium gas and is virtually complete in 200s. The XRD domain size rapidly increases to about 15 nm simultaneously with the saturation of the integrated intensity. No significant coarsening of the domains is seen at late times at this temperature. The final XRD size measured at room temperature was 15.9 ± 0.8 nm, value that is larger than the B2 particle size obtained during annealing in helium gas at the same temperature. This indicates that the coalescence process in the melted/disordered phase is facilitated by the forming gas likely because H2 prevents the formation of various Cu and Pd oxides.

The B2 phase formed at 300°C decays when annealed at higher temperature (figure 5.6(b)), while the disordered fcc phase grows as evidenced from the emergence of the fcc (111) and (200) reflections around 450°C. The transformation from B2 to disordered fcc structure (spanning from 400°C to 500°C) proceeds faster and at slightly lower temperature in case of the Pd:Cu mixture annealed in forming gas than in the case of annealing in helium. This phase transformation is further illustrated by the evolution of the calculated integrated intensities (figure 5.6(d)) and the evolution of the domain sizes (figure 5.6(f)). Figure 5.6(d) shows the integrated intensity of the three peaks corresponding to the (110) of the ordered B2 phase, and (111) and (200) of the disordered fcc phase. The decay of the B2 phase and simultaneous growth of

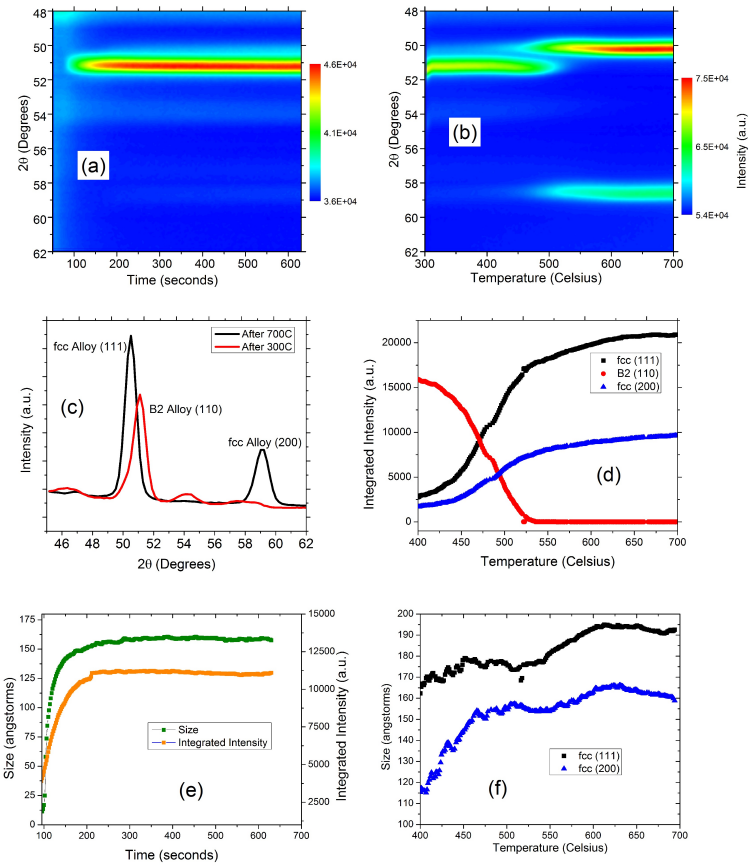

Figure 5.6. (a) Color map of the XRD intensity evolution for Pd:Cu nanoparticle mixture on SiO2/Si substrate isothermally annealed at 300°C in a forming gas atmosphere showing the formation of the ordered B2 phase. (b) Color map of the XRD intensity evolution of the Pd:Cu nanoparticle mixture on SiO2/Si ramped annealed from 300°C to 700°C in a forming gas atmosphere showing the transformation of the B2 phase into a disordered fcc alloy phase. (c) $\theta - 2\theta$ XRD scans after annealing at 300°C and 700°C. (d) Time evolution of the calculated XRD integrated intensities corresponding to the various peaks shown in (b) during ramp annealing from 300°C to 700°C. (e) Time evolution of the calculated XRD integrated intensities and domain size corresponding to the B2 phase shown in (a) during annealing at 300°C. (f) Time evolution of disordered fcc domain sizes calculated for the (111) and (200) peaks shown in (b) during ramp annealing from 300°C to 700°C.

the disordered fcc phase become visible around 400°C. By 525°C, the B2 phase is completely consumed by the new phase. Moreover, figure 5.6(f) shows the size of the fcc domains calculated from the width of the (111) and (200) peaks. The disordered domains rapidly grow to about 15 nm (the size of the starting B2 crystals) in the 400450°C temperature range. The fcc domains are slightly asymmetrical, with the size along the (111) direction being larger than the size along the (200) direction. Moreover, the domains continue to coarsen throughout of the remaining thermal treatment to 700°C. The XRD final size (measured at room temperature) of the disordered alloy nanoparticles after annealing to 700°C was 19.3 ± 0.1 nm. At this point we have not examined the late-stage kinetics of particle growth at high temperature, but we expect that once the solid-phase transformation is complete, the particles will continue to sinter following the model described in our previous work [139].

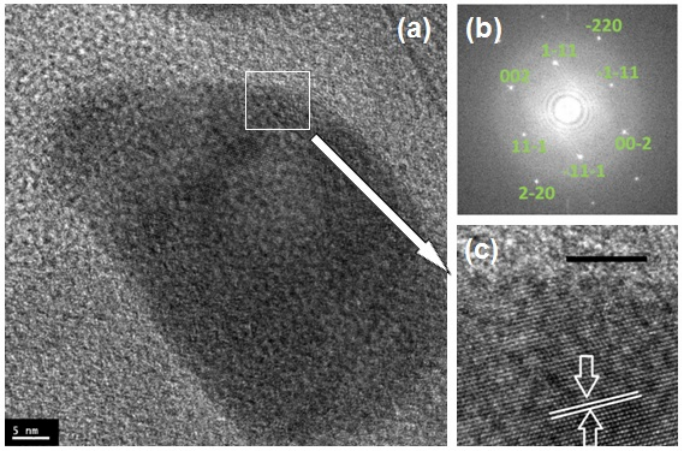

Figure 5.7. (a) TEM image of the Pd:Cu nanoparticle mixture after annealing to 700°C on SiO2/Si substrate in a forming gas atmosphere. (b) The FFT from the region indicated in (a) reveal fcc structure along [110] zone axis with (111) inter-planar spacing of 2.16$\mathring{A}$. (c) A high resolution image of random alloy phase along [110] zone axis. Scale bars are 5 nm for images (a) and (c).

Figure 5.7 shows a high resolution image of PdCu alloy nanoparticles formed after annealing of the mixture in forming gas at 700°C. The fast Fourier transform corresponding to the blown up region reveals a (111) plane with a lattice fringe

of 2.16$\mathring{A}$. The TEM calculated size of the PdCu alloy nanoparticles produced by annealing at 700°C in forming gas was found to be 28.04 ± 17.8 nm. Both our XRD and TEM sizes indicate that the PdCu alloy nanoparticles produced by annealing in forming gas at 300 and 700°C are larger, compared to final sizes of the alloy nanoparticles made by annealing in helium gas.

5.3.3 PdCu nanoparticle mixtures on other substrates

Carbon black

We have investigated the thermal evolution of Pd:Cu nanoparticle mixtures dispersed on carbon black and annealed in helium gas [148]. The nanoparticles form the B2 phase after annealing at 300°C and then undergo an incomplete transformation to a disordered fcc alloy during ramp annealing to 700°C, as shown in figures 5.8(a) and (b). The lattice parameter of the B2 structure was estimated to be $2.93 \pm 0.15\mathring{A}$, and the XRD crystalline domain size was 5.5 nm. The B2 phase transforms into the fcc alloy phase around 450°C. The phase transformation is indicated by the shift of the peak at 51° to lower angle and the growth of the fcc (200) peak at 58.5°. The disordered fcc alloy displayed peaks at 50.2°(111) and 58.2°(200) at room temperature (figure 5.8(c)), corresponding to a lattice parameter of 3.68$\mathring{A}$ and a crystalline domain size of 6 nm. The asymmetry of the (111) peak suggests that the transformation is incomplete, even at 700°C. The alloy produced after annealing at 700°C is Cu-rich, with a Pd concentration of just 25%, slightly lower than the composition of PdCu nanoparticles supported on SiO2/Si. The domain sizes are considerably smaller than observed on SiO2/Si substrates. In particular, no significant grain growth was observed at high temperature.

TEM imaging (not shown in here) also showed the nanoparticles on carbon black to have smaller final sizes as compared to the final sizes of the nanoparticles dispersed on SiO2/Si substrates. For example, the TEM size distribution of the PdCu alloy nanoparticles dispersed on carbon black and annealed in helium gas at 700°C was

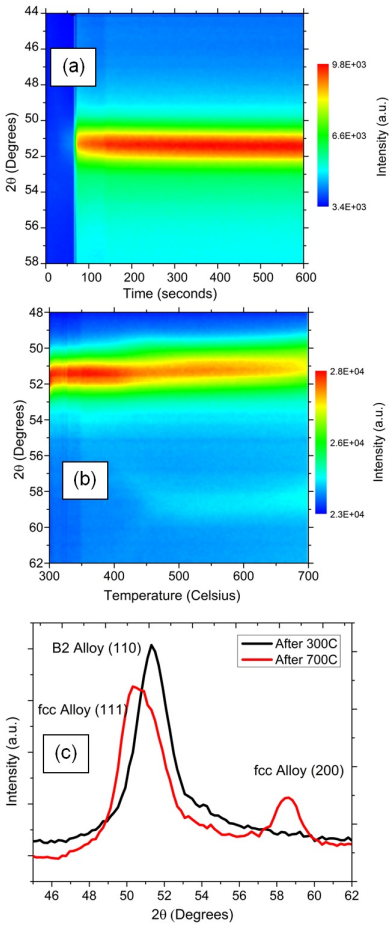

Figure 5.8. (a) Color map of the XRD intensity evolution for a Pd:Cu nanoparticle mixture on carbon-black substrate isothermally annealed at 300°C in a He gas atmosphere showing the formation of the ordered B2 phase. (b) Color map of the XRD intensity evolution for the Pd:Cu nanoparticle mixture on carbon-black ramped annealed from 300°C to 700°C in a forming gas atmosphere showing the transformation of the B2 phase into a disordered fcc alloy phase. (c) $\theta - 2\theta$ XRD scans after annealing at 300°C and 700°C.

found to be bi-modal, with peaks at 3.7 ± 0.1 nm and 6.4 ± 0.3 nm after counting 400 particles. The smaller particle size on carbon black is likely due to the low particle loading and limited particle mobility on carbon black as opposed to SiO2/Si substrates.

Alumina

The Pd:Cu nanoparticle mixtures were also dispersed on alumina membranes and annealed in helium, as shown in the color map of the XRD intensity evolution in figures 5.9(a) and (b). The structural evolution of the nanoparticle mixtures in this case was dramatically different from the other substrates studied. On annealing at 300°C, the Pd and Cu metals appear to segregate to form separate fcc almost-pure Pd and Cu phases. This is illustrated in figures 5.9(a) and (c) by the presence of the Cu and Pd (111) and (200) x-ray peaks. The Pd and Cu phases undergo grain growth without significant intermixing at this temperature.

As a result of this segregation, the B2 structure was never synthesized in these Pd-Cu nanocatalysts dispersed on alumina. The Pd and Cu metal phases remained separate until annealed well beyond 600°C. Figure 5.9(b) is the color map of the intensity evolution of the Pd:Cu nanoparticle mixture during ramped annealing from 300°C to 700°C . Above 600°C, the nanoparticles sinter and the two metals interdiffuse, forming alloy phases. This alloying temperature is significantly higher than that of Pd:Cu nanoparticle mixtures dispersed on carbon or SiO2/Si and annealed in helium. On further analysis, we find that the Pd:Cu nanoparticle mixture forms two dominant alloy phases with lattice parameters of 3.69$\mathring{A}$ and 3.87$\mathring{A}$. Using Vegards law, we estimated the two alloy phases to be 30% and 90% Pd, respectively. Hence we confirm the formation of two different alloys when dispersed in alumina, one rich in Cu, and another one with very high Pd composition. Our results are in agreement with Sun et al. [138], who explored the Pd-Cu catalysts on -Al2O3 and concluded that a bimetallic alloy is formed at 800°C with either Pd- or Cu-rich surfaces. There was no evidence of formation of the B2 phase in their study, either. However, Sanchez-Escribano et al. [149] found evidence of formation of both disordered fcc and ordered CsCl-like structures for the Pd-Cu alloy prepared by co-impregnation and supported on $\gamma - Al_2O_3$.

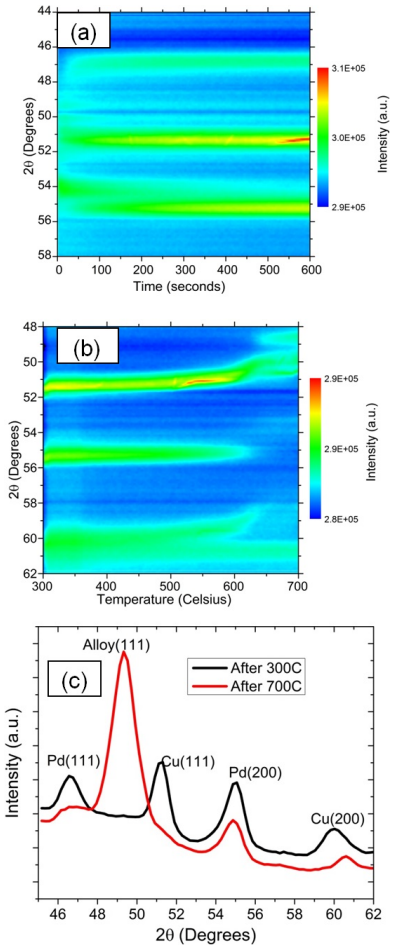

Figure 5.9. (a) Color map of the XRD intensity evolution for a Pd:Cu nanoparticle mixture on alumina substrate isothermally annealed at 300°C in a He gas atmosphere. No B2 phase is formed in this process. (b) Color map of the XRD intensity evolution of the PdCu nanoparticle mixture on alumina ramped annealed from 300°C to 700°C in a He gas atmosphere showing the formation of a disordered fcc alloy phase. (c) $\theta - 2\theta$ XRD scans after annealing at 300°C and 700°C .

5.4 Discussion

A significant body of knowledge on the structure and phase transformations in binary nanoparticles systems comes from theoretical simulations [1]. The PdCu system exhibits a multitude of interesting ordered structures. In particular, in the vicinity of 50% Pd-composition, PdCu alloys form an ordered, body-centered, cubic-like CsCl

structure (B2 phase) at low temperature even though the constituents Pd and Cu both have face-centered cubic lattices [145]. Some experimental reports of bimetallic PdCu nanoparticles found formation of the B2 phase at low temperatures [150]. Others, however, found no evidence of the B2 phase. Zhu et al. [151] compared x-ray diffraction data with theoretical calculations employing molecular dynamics/Monte Carlo corrected effective medium inter-atomic potential and concluded that distorted fcc clusters of sizes less than 10 nm, rather than B2 clusters, are most likely formed. Furthermore, theoretical studies by Shah and Yang [152] examined equiatomic PdCu nanoclusters with spherical shape containing 50-10000 atoms. They showed that the fcc structure is energetically favored over the CsCl-like structure for cluster sizes up to a few thousand atoms. They also predicted a structural transition from the fcc to the CsCl-structure for clusters consisting of about 10000 atoms. Shah et al. supported their theoretical calculations with experimental results that showed the distorted fcc cluster to best fit diffraction data for clusters of size ranging from 6 to 10 nm. In contrast to the latter theoretical and experimental findings, our experimental data identified the ordered B2 phase as the stable phase for PdCu nanoparticles as small as 6 nm formed through thermal annealing of Pd:Cu nanoparticle mixtures. This B2 phase transforms to a disordered fcc phase above approximately 450°C.

An important aspect of the structure of the nanoparticles with consequences for chemical activity is component segregation, especially to the surface. The elemental segregation is expected to occur primarily on the surface of bimetallic nanoparticles, leading to core-shell, or core-multi-shell, formation. However, the results of theoretical studies on Pd-Cu nanoparticles have been mixed. Some studies have reported surface segregation of Cu, while others have reported Pd enrichment. For example, Mottet et al. [71] performed Monte Carlo simulations of unsupported PdCu clusters with fcc, bcc polyhedra, and icosahedral structures. They found Cu segregation on the surface with slight Pd enrichment just under the surface for fcc and icosahedral structures. The segregation was also dependent on the facet orientation; i.e., Pd atoms preferentially occupy (111) facet sites. They also showed how phase and morphological

configurations change with size, concentration, and temperature. Similarly, Zhu et al. [151] found that the surface layer is enriched with Cu, while the second layer is Pd-rich, and they confirmed the facet-dependence of Cu enrichment. Renouprez et al. [153] observed higher concentration of Cu in PdCu clusters supported on silica using low-energy ion scattering (LEIS) and Monte Carlo simulations. The factors in favor of Cu surface segregation include lower surface free energy, negative heat of mixing when alloying, and difference in atomic radii of Cu and Pd. However, Bradley et al. [154] found Pd enrichment in supported PdCu bimetallic alloys using x-ray absorption spectroscopy (XAS) and attributed it to strong driving force of Cu to maximize coordination number with Pd. Molenbroek et al. [155] also used EXAFS to study nanoparticles with compositions ratio of Pd:Cu of 1:1 and 1:2 synthesized by atomic layer deposition and co-impregnation techniques and found Cu-rich surfaces for alumina-supported particles, but random alloying for silica supported particles.

Since we are investigating alloying in Cu:Pd nanoparticles mixtures, we expect the thermally induced evolution of the physical mixtures to be somewhat different from the evolution of bimetallic PdCu nanoparticles. Coalescence of two nanoparticles is typically driven by surface diffusion. In the case of two different metals, the coalescence can result in alloyed, coreshell,or multi-domain particles. For PdCu, volume diffusion also plays a major role in the intermixing of the constituents into different alloy phases. The competition between surface and volume diffusion may lead to non-uniform bimetallic nanoparticles of different compositions with either Pd- or Cu rich surfaces. It is possible that the physical mixtures evolve in a manner similar to bi-layers of Pd and Cu. Pomerantz et al. [130] have found the Kirkendall effect in PdCu bi-layers due to the differences in the diffusion coefficients of Pd and Cu. To explore these issues, we investigated the possibility of enrichment or segregation by either Pd or Cu in the annealed nanoparticles using aberration-corrected HAADF-STEM and EDX mapping of Pd:Cu nanoparticle mixtures supported on carbon black and annealed to 700°C in helium gas, as shown in figure 5.10. EDX indicates approximately homogeneous mixing of the two metals in the volume of the nanoparticles, but also

supports the possibility of slight Pd enrichment on the surface. This finding is surprising considering expectations based on the composition of the mixture (34% Pd: 66% Cu determined by ICP-AES) and theoretical predictions [71,151,153]. Moreover, in our experiments Cu needs to diffuse from the surface to the volume, and therefore we would expect Cu surface enrichment. However, our results are consistent with a previous experimental study of PdCu nanoparticles [134], and they suggest that the Pd-rich surface is energetically stable at the nanoscale. EDX also shows the presence of small Pd nanoparticles. Even though figure 5.10 indicates local elemental segregation on the surface of the larger alloyed particles, more investigations are needed to identify the dependence of surface segregation on the crystallographic orientation of the facets.

We have not yet performed EDX of the alumina-supported nanoparticles for which the XRD data indicates large scale phase segregation at 300°C and partial alloying when annealed to 700°C. The effect of the supporting substrate on the alloying/segregation of multi-metallic nanoparticles is a topic of extreme interest due to its relevance for catalytic performance [156] and is still under investigation. At this point we can only speculate that our observations of enhanced segregation on alumina are related to strong and/or different binding [153] of the original ultrafine Cu and Pd nanoparticles on the alumina substrate and ensuing low particle mobility. Significantly different surface mobility of the two species in the mixture may result in size/component segregation as early as when the mixture is dispensed on the substrate, or later when the mixture is heated to 300°C. Either scenario would explain formation of pure Cu and Pd phases. These two phases intermix to some extent as the sample is further annealed above 600°C, but since the degree of the transformation depends on the size of the Pd and Cu domains, temperature, and duration of the heat treatment, the intermixing is incomplete.

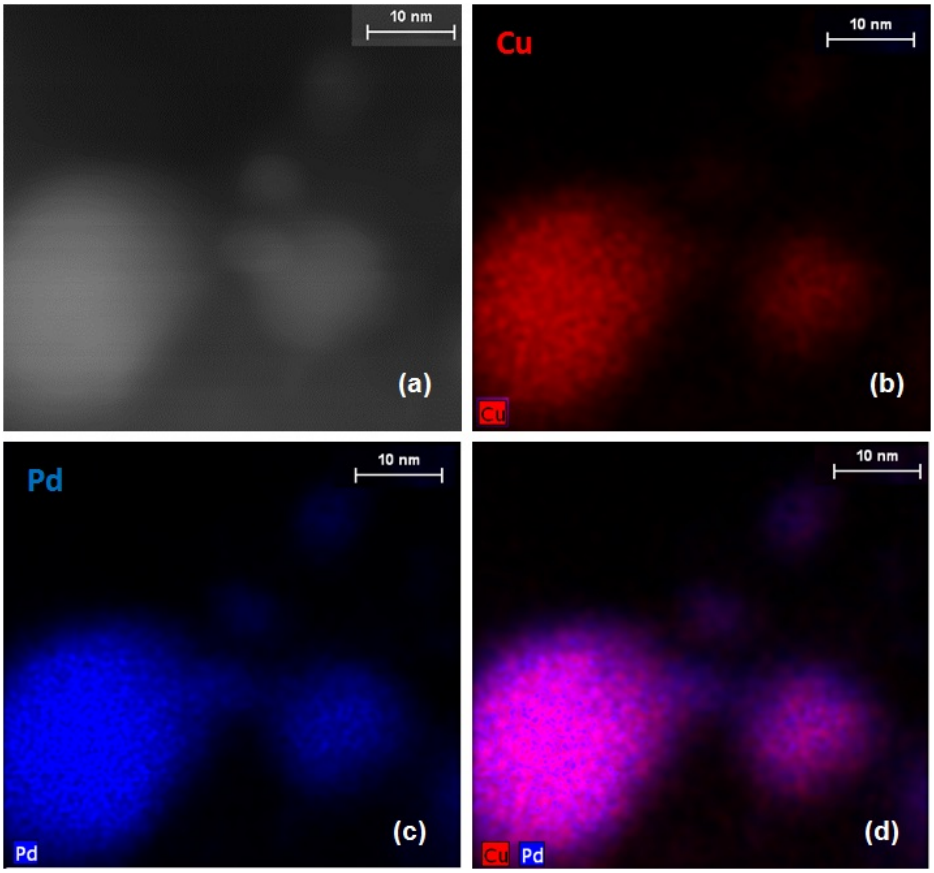

Figure 5.10. HAADF-STEM and EDX maps of PdCu alloy nanoparticles after annealing to 700° on Carbon black in He gas: (a) HAADF-STEM, (b) Cu map, (c) Pd map, and (d) combined Pd and Cu map. It shows a slight Pd enrichment on the surface of the nanoparticles.

5.5 Conclusion

In situ real time XRD and transmission electron microscopy were used to examine the structural transformations in Pd:Cu nanoparticle mixtures on several different support substrates in high-purity He and forming gas. Annealing of the nanoparticle mixtures dispersed on SiO2/Si and C-black at 300°C leads to formation of alloy nanoparticles with chemically-ordered CsCl-type (B2) structure. Upon further annealing to 700°, the B2 structure transforms into a chemically-disordered Cu-rich fcc alloy. The temperature range of the transformation is consistent with expectations

based on the bulk Pd-Cu phase diagram. The behavior of silica- and C-supported Pd:Cu nanoparticle mixtures was qualitatively similar when the heat treatment was performed in high-purity Helium or forming (H_2/N_2) gas. The difference between final sizes for silica- and C-supported nanoparticles can be attributed to particle loading. A significant quantitative difference between the final size of the nanoparticles was found for the two types of atmospheres, with the nanoparticles annealed in forming gas being larger than the nanoparticles annealed in He gas. This is caused by the reduction of the metal oxides in H_2/N_2 gas that promotes nanoparticle coalescence and sintering. EDX mapping of the nanoparticles annealed to 700° indicated slight Pd-enrichment on the nanoparticle surface. This surface Pd-enrichment also explains the lower than expected Pd-composition calculated from the XRD data for the volume of the disordered alloy.

The degree of metal intermixing is highly dependent on the nature of the supporting material. The alumina-supported Pd:Cu nanoparticle mixtures produced pure Pd and Cu phases when annealed at 300°C. Upon annealing to 700°C, the alumina-supported samples formed two distinct disordered fcc alloys, a Cu-rich (30% Pd) and a Pd-rich (90% Pd) alloy. The B2 structure was absent in the evolution of Pd:Cu nanoparticle mixtures dispersed on alumina. Understanding the implications of these findings to the control of catalytic properties of the bimetallic nanoparticles is part of our on-going research.

6. FUTURE RESEARCH DIRECTIONS

Some of the future research directions are discussed briefly in this chapter. The first section of this chapter presents a study of Pd and Cu nanoparticle mixture as a function of Pd:Cu composition ratio. Faceting and defects play a major role in the structural evolution of the mono and multi-metallic nanoparticles. Experimentally these are currently investigated using synchrotron based XRD and TEM in PtNiFe nanoparticles. Another direction of study involves computer simulations of sintering and structural phase transformations in mono metallic nanoparticles that can be compared to experimental studies using TEM.

6.1 Chemical composition and ordering studies of physical mixtures of Pd and Cu nanoparticles

The direct ethanol fuel cell (DEFC) is more convenient than direct methanol fuel cell as ethanol is less toxic and can be obtained from biomass conversion of common agricultural products such as sugar cane and corn. The major challenge in DEFC is finding an efficient catalyst. Thermal annealing and post-synthesis treatment are required for the activation and stability of these catalysts. PdCu is found to have higher mass activity than Pd for ethanol oxidation reaction in alkaline electrolyte [134]. The Pd-Cu bimetallic nanoparticles are not only used as catalysts in fuel cells but also have important applications in coal gasification process, selective hydrogenation of dienes and hydrogen storage reactions.

The bulk Pd-Cu system undergoes different structural phase transformations at different compositions. The compositions of interest in this study correspond to (a) 50% Pd and Cu and (b) 75% Pd and 25% Cu. In Pd:Cu of composition ratio 1:1, ordered B2 phase is formed during annealing at 450°C. During the ramped annealing

from 450°C to 750°C, the B2 phase transforms into two different alloys, one alloy rich in copper and the other rich in Pd. This structural evolution is different from that of Pd-Cu system in bulk. In the 3:1 composition, the B2 is phase dominates in the isothermal anneal at 450°C but a disordered alloy fcc phase is also formed. Upon annealing to 750°C, the disordered fcc phase grows at the expense of the B2 phase.

6.1.1 Nanoparticle mixtures Pd:Cu = 1:1

These Pd:Cu nanoparticles samples were prepared by mixing Pd nanoparticles and Cu nanoparticles in the ratio 1:1 by volume. We monitor the structural evolution of the Pd-Cu nanoparticles mixture in two thermal treatments. Figure 6.1 shows the color map of the XRD intensity evolution in the two thermal treatments. For the isothermal anneal to 450°C, the temperature is ramped from 25°C to 450°C at a rate of 1000C/min and stabilizes at 450°C in less than 20 seconds. Figure 6.1(a) shows the intensity evolution of the (110) peak at 2θ angle of $50.71 \pm 0.03°$ during this annealing step. We see that the PdCu forms an ordered phase referred to as the B2 structure as discussed before in chapter 5 [133, 157]. From the analysis of the XRD data, we estimate the lattice parameter of the B2 structure was $2.96 \pm 0.01\mathring{A}$ and the grain size was 13.2 ± 1 nm. This lattice parameter corresponds to the (110) plane of the PdCu B2 structure (space group Pm3-m) as confirmed by the work of Yamauchi and Tsukuda [146]. This transformation occurs at 450°C and not during the heating. Additional verification of this phase was also done by HRTEM analysis similar to that shown in chapter 5 [157].

The second step in the annealing protocol is increasing the temperature from 450°C to 750°C at the ramp rate of 30°C/min after 30 seconds at 450°C. Here a complex change involving phase transformation and phase segregation is witnessed. The PdCu B2 structure transforms into two different fcc alloy structures. The B2 structure having a lattice parameter of $2.96 \pm 0.01\mathring{A}$, transforms into (a) a dominant fcc alloy structure with a lattice parameter of $3.67 \pm 0.01\mathring{A}$ with the peaks at angles

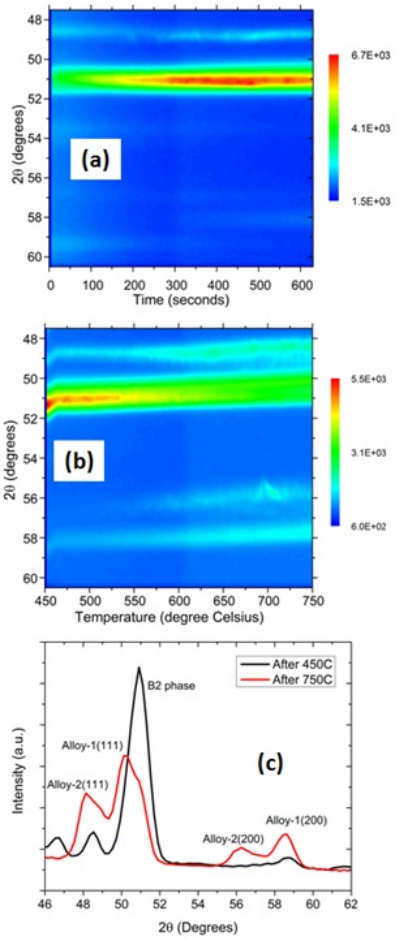

Figure 6.1. (a) Color map of the XRD intensity evolution for the Pd:Cu = 1:1 nanoparticle mixture on SiO2/Si substrate isothermally annealed at 450°C in a forming gas atmosphere showing the formation of the ordered B2 phase. (b) Color map of the XRD intensity evolution of the Pd:Cu nanoparticle mixture on SiO2/Si ramp annealed from 450°C to 750°C in a He atmosphere showing the transformation of the B2 phase into two disordered fcc alloy phases. (c) $\theta - 2\theta$ XRD scans after annealing at 450°C and 750°C.

$49.9 \pm 0.2°$ and $58.3 \pm 0.1°$ corresponding to the fcc(111) and fcc (200) planes (denoted as Alloy 1 here on) and (b) a secondary fcc alloy structure with a lattice parameter of $3.81 \pm 0.01 \mathring{A}$ calculated from the peaks at angles $48.1 \pm 0.1°$ and $56.2 \pm 0.2°$ corresponding to the fcc (111) and fcc (200) planes (denoted as Alloy 2 here on). Using the Debye-Scherrer relation, the grain sizes corresponding to the fcc (111) direction for

Alloy-1 and Alloy-2 were found to be 20.5 ± 2.9 nm and $13.6 \pm 1.4nm$ respectively. We also see the presence of the two different alloy phases in the $\theta - 2\theta$ XRD scan taken after the samples annealed at 450°C and 750°C were quenched to room temperature as shown in figure 6.1(c).

Next we look at the composition of the Pd:Cu alloy nanoparticles. From XRD data, using Vegards law, we can calculate the lattice parameter to find the % content of each of the metals in the alloy nanoparticles. From the smaller lattice parameter of Alloy 1, we find the Cu % content in the nanoparticles is 78% and Pd is mere 22%. For Alloy 2, we find the Cu % content in this part of the nanoparticles is 29% and Pd content is 71%. So we report the formation of two alloys- one with majority Cu and another with majority Pd. This unique structural evolution as not seen in other Pd:Cu compositions of 1:3 [157] and in 3:1 as discussed further in the next subsection.

The structure and phases of the Pd:Cu = 1:1 nanoparticle mixture annealed at 750°C were confirmed by high resolution-TEM images. After annealing in forming gas to 750°C, the analysis of the TEM images estimated the average size to be $22.85 \pm 7.4\mathring{A}$ from counting 350 nanoparticles. Figure 6.2(a) further corroborates the existence of two different alloy structures. The fast Fourier transform (FFT) of one specific region reveals the zone axis and lattice fringes along a particular plane. Figure 6.2(b) reveals the lattice fringe of $2.19\mathring{A}$ of the (111) plane. Figure 6.2(c) is the FFT of figure 6.2(b) showing the [311] zone axis of alloy 1 (Fm-3m space group) [158]. Similarly figure 6.2(d) shows the lattice fringe of $1.93\mathring{A}$ of the (002) plane. Figure 6.2(e) is the FFT of figure 6.2(d) showing the [110] zone axis of alloy 2 (Fm-3m space group) [159]. These high resolution images of the PdCu alloy nanoparticles confirm the crystalline nature of the two alloys. Conventional TEM images of different regions of the sample did not reveal any morphological differences corresponding to the two different alloys formed in these samples.

The composition and phase segregation observed in the XRD was further confirmed by the EDX and HAADF-STEM analysis on these samples. HAADF-STEM of such nanoparticles is shown in figure 6.3(a) and it revealed a relatively uniform

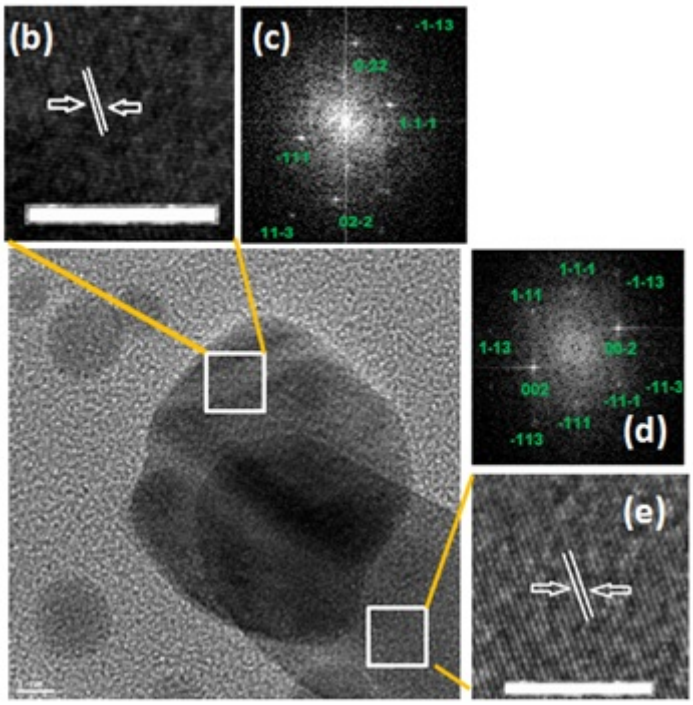

Figure 6.2. (a) TEM image of the Pd:Cu= 1:1 nanoparticle mixture after isothermal annealing at 750°C on SiO2/Si substrate in forming gas atmosphere. (b) High resolution image of the PdCu particle marked in (a) reveals uniform lattice fringes across the particle with an inter-planar distance of 2.19$\mathring{A}$ that corresponds to [111] plane of Alloy 1 phase. (c) The FFT from a marked area in (b) is indexed as [311] zone axis of the PdCu alloy 1 phase. (d) High resolution image of the PdCu particle marked in (a) reveals uniform lattice fringes across the particle with an inter-planar distance of 1.93$\mathring{A}$ that corresponds to [002] plane of alloy 2 phase. (d) The FFT from a marked area in (e) is indexed as [110] zone axis of the PdCu alloy 2 phase. Scale bars are 5nm

alloy distribution. However, HAADF-STEM is only sensitive to the atomic number (Z) of elements, it cannot sense the different alloy structure in the nanoparticles. Our EDX maps of the nanoparticles showed a uniform distribution of Pd and Cu in the alloy nanoparticles. However, the EDX point scans revealed composition variation in the different regions of the nanoparticle mixtures probed. Figure 6.3(a) shows the HAADF-STEM image of an alloy nanoparticle formed from the annealing protocol

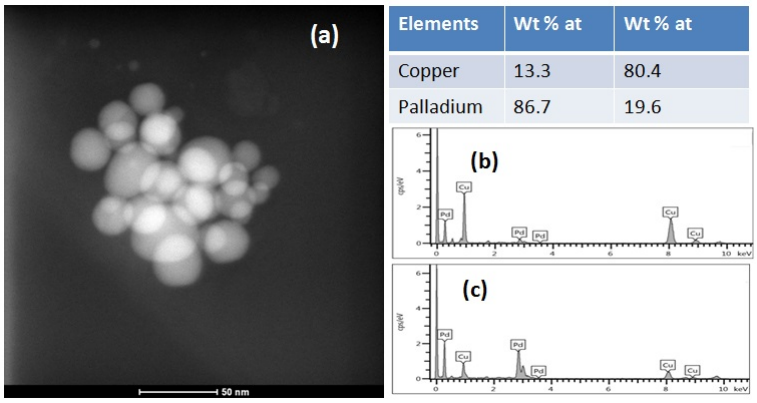

Elements	Wt % at	Wt % at
Copper	13.3	80.4
Palladium	86.7	19.6

Figure 6.3. (a) HAADF-STEM image of the Pd:Cu = 1:1 nanoparticles mixture. Scale bar is 50 nm (b) EDX spectrum obtained in (a). (c) EDX spectrum obtained in (a). Table: Pd and Cu compositions from (b) and (c).

followed in this study and the corresponding table reveals the atomic percentages from the EDX spectra (figure 6.3(b) and 6.3(c)) in different regions in the nanoparticles. This confirms the formation of two alloy structures in these Pd:Cu nanoparticle mixtures with different atomic percentages of Pd and Cu as shown in the table in figure 6.3. We speculate the formation of Pd-rich and Cu-rich phases by spinodal decomposition. The bright regions in the HAADF-STEM images are attributed to more atomic columns (thicker in PdCu alloy) of the samples.

6.1.2 Nanoparticle mixtures Pd:Cu = 3:1

The two metallic nanoparticles in toluene synthesized separately were mixed by volume in the ratio 3:1, with more Pd in the mixture. When annealed at 450°C isothermally, the Pd:Cu nanoparticle mixture showed the presence of two structures: (a) B2 phase as seen in 1:1 composition and (b) fcc alloy phase (Alloy 3) as shown in figure 6.4. The B2 phase has an (110) peak at 50.7° and the calculated lattice parameter is 2.96±0.01$\mathring{A}$. There are additional peaks at 48.16±0.05° and 56.62±0.21°

which corresponds to the fcc structure (111) and (200) planes, respectively, as seen in figure 6.4(a).

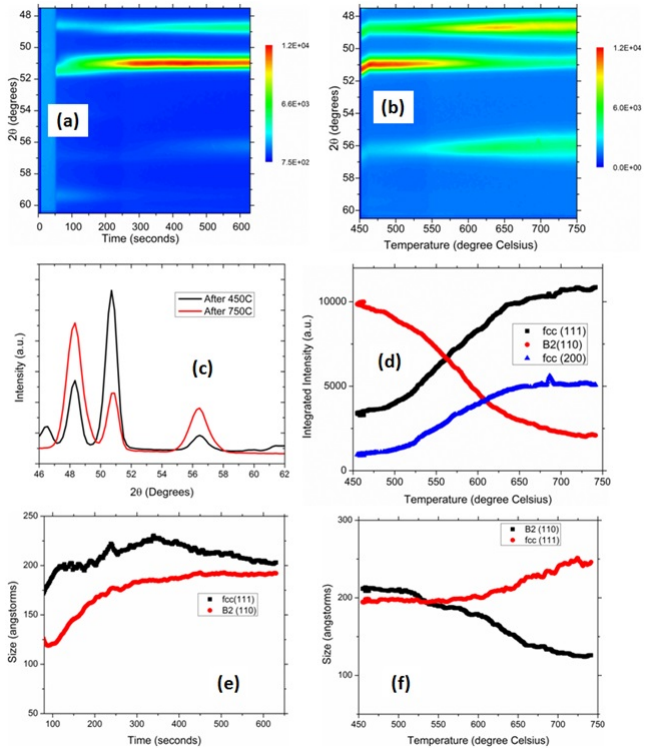

Figure 6.4. (a) Color map of the XRD intensity evolution for the Pd:Cu = 3:1 nanoparticle mixture on SiO2/Si substrate isothermally annealed at 450°C in a forming gas atmosphere showing the formation of the ordered B2 phase and another alloyed phase. (b) Color map of the XRD intensity evolution of the Pd:Cu nanoparticle mixture on SiO2/Si ramp annealed from 450°C to 750°C in forming gas atmosphere showing the incomplete transformation of the B2 phase into the disordered fcc alloy phase. (c) $\theta - 2\theta$ XRD scans after annealing at 450°C and 750°C. (d) Time evolution of the calculated XRD integrated intensities corresponding to the various peaks shown in (b) during ramp annealing from 450°C to 750°C. (e) Time evolution of the calculated XRD and domain size corresponding to the B2 and fcc phase shown in (a) during annealing at 450°C. (f) Time evolution of disordered fcc domain sizes calculated for the (111) and (200) peaks shown in (b) during ramp annealing from 450°C to 750°C.

The evolution of the coherent XRD crystalline domain sizes calculated from figure 6.4(a) is shown as a function of time in figure 6.4(e). The growth of both ordered

phase (B2) and the Alloy 3 phase is not simultaneous. The corresponding lattice parameter of the dominant (111) fcc structure is $3.80 \pm 0.004\mathring{A}$ and the qualitative size is 17.2 ± 2.2nm. Upon annealing from 450°C to 750°C, there were changes in structure as evidenced in figure 6.4(b). Here the dominant phase is the Alloy 3 phase and the B2 phase is observed to decrease with temperature. In figure 6.4(c), this was confirmed by the $\theta-2\theta$ scans done on the sample after quenching to room temperature from 450°C and 750°C. The sizes calculated from the $\theta - 2\theta$ scans are as follows. For the 450°C anneal, the size of the B2(110) phase is 16.3 ± 0.5 nm . For the 750°C treatment, the size of the dominant fcc(111) phase is 11.8 ± 0.7 nm. The XRD peaks indicate that the B2 phase was the dominant phase when the mixture was annealed at 450°C and the fcc (111) phase is the dominant phase when annealed to 750°C. The integrated intensity plot in figure 6(d) reveals that the B2 phase decreases steadily above 550°C, whereas the fcc alloy grows with temperature. The qualitative sizes of the fcc domains increased with increasing temperature as shown in figure 6.4(f).

After annealing in forming gas to 750°C, the analysis of the TEM images estimated the average size to be $23.25 \pm 13.8\mathring{A}$ from counting 550 nanoparticles. The high resolution TEM images (figure 6.5(a)) of the Pd:Cu = 3:1 nanoparticle mixtures substantiate the formation of Alloy 3 phase with majority Pd in it after annealing to 750°C. Figure 6.5(b) shows a blow up of the lattice fringes and it is found to have spacing of $2.16\mathring{A}$ corresponding to the (111) lattice plane of Alloy 2 (belonging to the space group Fm-3m) [159]. The FFT of the region corresponds to the [111] zone axis of Alloy 2.

Using Vegards law with the XRD data, the Cu content was estimated as 29%. Here the alloy nucleation is predicted to happen during the pre-annealing process. The alloy composition is further verified with EDX analysis shown in figure 6.6. The % content of Cu in these Pd:Cu = 3:1 nanoparticle mixtures obtained with EDX was found to be 24% which is in agreement to that calculated from the XRD data.

Concluding this section, B2 phase is formed during annealing to 450°C in both compositions. However during annealing to 750°C, their behaviors are dramatically

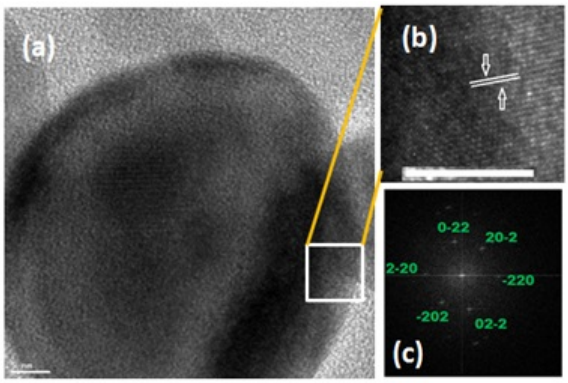

Figure 6.5. (a) TEM image of the Pd:Cu = 3:1 nanoparticle mixture after isothermal annealing at 750°C on SiO2/Si substrate in forming gas atmosphere. (b) High resolution image of the PdCu particle marked in (a) reveals uniform lattice fringes across the particle with an inter-planar distance of 2.14$\mathring{A}$ that corresponds to [110] plane of Alloy 2 phase. (c) The FFT from a marked area in (a) is indexed as [111] zone axis of the PdCu alloy 2 phase. Scale bars are 5nm for images (a) and (c), respectively.

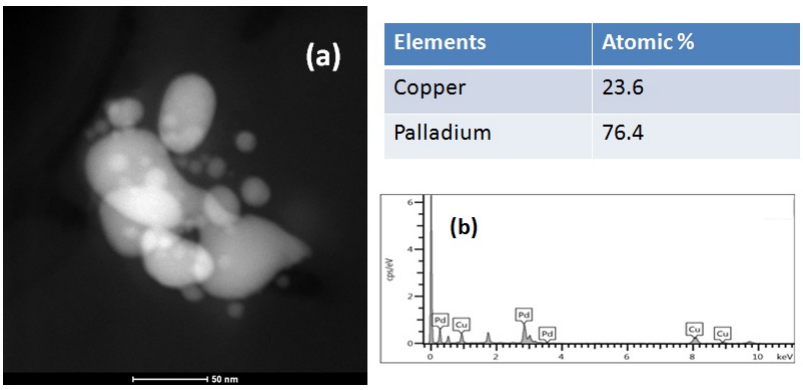

Elements	Atomic %
Copper	23.6
Palladium	76.4

Figure 6.6. (a) HAADF-STEM image of the Pd:Cu = 3:1 nanoparticle mixture after annealing at 750°C. Scale bar is 100 nm (b) EDX spectrum obtained in (a). Table: Pd and Cu compositions from (b).

different. In 1:1 composition, the B2 phase underwent transformation to two different alloys, one rich in Pd and the other poor in Pd. The formation mechanism can be rationalized by spinodal decomposition involving diffusion. This behavior is attributed to the composition of Pd and Cu atoms in the nanoparticles and the finite

size effect of nanoparticles as well. In 3:1 composition, the B2 phase decays but not completely and the disordered fcc alloy formed is the dominant phase after annealing to 750°C. The temperature range for the transformation in both compositions was slightly smaller than that of the bulk. The detail of the alloy formation requires further exploration with other techniques to probe each monolayers of the nanoparticles (from shell to the core) and high resolution imaging *in situ* TEM. We need to explore the structural evolution of Pd:Cu nanoparticles mixtures of different sizes to build a phase diagram as a function of size and composition. These studies will be the major direction of our ongoing investigations to create tunable structures and compositions of multi-metallic nanoparticles.

6.2 High temperature studies of PtNiFe

It is of great practical interest to prevent the nanoparticles from sintering and to maintain their size, shape and structure in catalysis, nanofabrication, sensor technology etc. In catalysis, sintering hinders the nanoparticles from achieving higher catalytic efficiency. It is very important to prevent the particle growth while maintaining optimal surface loading of the nanoparticles. Nanoparticle loading can be manipulated by controlling the thickness of the films of nanoparticles in solvents while dispersing them on substrates.

In order to mimic the behavior of the nanoparticles on electrodes in fuel cell, we plan to disperse nanoparticles on silica/silicon substrates by different casting techniques to control the surface loading. To reduce the film thickness on the substrates, we can use drop casting, spin casting [160] and micro-contact printing [161]. These techniques have been used to reduce the film thickness in a controlled manner. Sintering behavior is expected to be different in thick films (3 dimensional) and thin films (2 dimensional few monolayers). The factors affecting the films of nanoparticles on substrates are evaporation rate of the solvent, hydrophilicity/hydrophobicity of capping agents, interparticle separation, concentration of the nanoparticles in solvent,

strength of interaction between particles, substrate and solvent etc. In the regime between 2D and 3D films, the sintering is expected to follow coalescence [162–164].

We have performed preliminary research to monitor the sintering of the nanoparticles as a function of thickness of the nanoparticles films and annealing temperature. *In situ* real time x-ray diffraction was used to study the phase and morphological transformations in PtNiFe nanocatalysts used in fuel cells. The nanoparticles were synthesized by single-organic phase method involving metal precursors, reducing agent and capping agent [165]. Luo et al. have concluded that the ternary nanoparticles are highly active towards molecular oxygen electrocatalytic reduction. The PtNiFe nanoparticles of size 4nm supported on planar silica on silicon were monitored as a function of thermal treatment in the temperature range 600 to 1000°C. The PtNiFe nanoparticles were dispersed on a silica/silcon substrate by drop casting, spin casting and micro-contact printing. The nanoparticles aggregate and undergo alloying, but the low density as-prepared nanoparticle samples exhibit signature of preferential orientation during annealing in the case of the spin-cast specimen. This was absent in both drop-cast and contact printed specimen. The influence of annealing atmospheres on the evolution of these nanoparticles was also investigated.

The structure of the PtNiFe nanoparticles was monitored by synchrotron based XRD and it is summarized in figure 6.7. Figure 6.7 (a) shows the evolution of the intensity of the fcc peaks ((111), (200)) developed during annealing of PtNiFe nanoparticles drop cast on SiO2/Si substrate to 950°C in a He atmosphere. We see that alloy peaks developed at 48.2° and 56.3° corresponding to the fcc (111) and fcc (200) structure. The lattice parameter of the alloy was found to be $3.81 \pm 0.11\mathring{A}$. The side panel shows that the fcc (200) peak is more intense than the fcc (111) peak. This was confirmed by the analysis of the XRD data. In figure 6.7(b), the integrated intensity corresponding to both fcc(111) and fcc(200) peaks are plotted as a function of time. The integrated intensity of the (200) peaks is dominant. This is possibly due to the formation of facets in the alloy nanoparticles. Figure 6.7(c) shows there is no

substantial difference in the coherent grain size corresponding to the (111) and (200) peaks. The grain size grows from 4.7 nm to 9.4 nm during the annealing process.

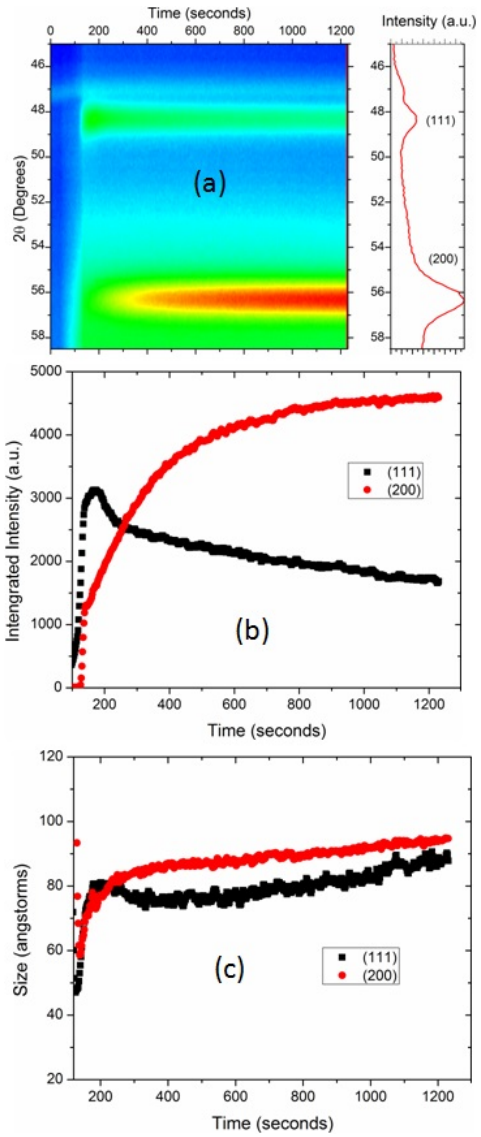

Figure 6.7. (a) Color map of the XRD intensity evolution for PtNiFe nanoparticle mixture spin cast on SiO2/Si substrate isothermally annealed at 950°C in He atmosphere. (b) Time evolution of the calculated XRD integrated intensities corresponding to the (111) and (200) phases seen in (a). (c) Time evolution of disordered fcc domain sizes calculated for the (111) and (200) peaks seen in (a).

Further experimental investigations using TEM and AFM are required for confirming that faceting is dominant in spin cast samples. Also, more synchrotron based XRD studies have to be carried out on drop-cast samples to understand the structural evolution of few monolayers of nanoparticles dispersed on flat substrates.

6.3 Simulations of coalescence and sintering of nanoparticles

Sintering in bulk has been explained with atom diffusion in the neck region between the particles. Macroscopic sintering models cannot be directly applied to understand the nanoscale phenomena. In nanoparticles, the neck region is often a fraction of a nanometer and is a region difficult to study via transport phenomena with great accuracy. Molecular dynamics can access the time and length scales critical to study the sintering of nanoparticles accurately. Sintering of nanoparticles happens via reduction in surface area and the pertinent mechanisms were found to be grain boundary diffusion and surface diffusion [115].

We present some preliminary results from a study of solid state sintering in gold nanoparticles modeled with the Embedded atom method (EAM) potential. For developing a fundamental understanding at the basic level, the simulations are run to model sintering for unsupported nanoparticles in vacuum. The simulations were set up with free boundary conditions in NVT ensemble where different temperatures employed were 300K, 500K, 700K, 900K and 1100K. Particle sizes are chosen to be 2 nm, 5 nm and 10 nm and the pair wise combination of those resulted in six different pairs as (5 nm, 2 nm), (5 nm, 5 nm), (5 nm, 10 nm), (10 nm, 2 nm), (10 nm, 5 nm) and (10 nm, 10 nm). The melting temperature is a function of particle size and the melting temperature for the chosen particle sizes are approximated by Buffat and Boral to be 530 K, 1080 K and 1230 K for 2 nm, 5 nm and 10 nm particles, respectively [56]. The crystal structure of gold is taken as the face-centered cubic with the lattice constant a = 4.08$\mathring{A}$. For each simulation, two spherical nanoparticles of the specified size and temperature of interest are created with 2$\mathring{A}$ separation between the edges of nanopar-

ticles without prior stabilization. The simulation is run for 50,000 steps where the time step is chosen to be 2 fs (0.002 ps) resulting in a total simulation time of 100 ps. The physical quantities checked were positions, velocities, total energy, potential energy, stress (diagonal and off-diagonal), mean square displacement and radius of gyrations. The molecular dynamic (MD) simulation is coded using LAMMPS (Large-scale Atomic/Molecular Massively Parallel Simulator) and was visualized using VMD (Visual Molecular Dynamics). This project was started in collaboration with Dr. Hojin Kim and Prof. A. Strachan, Department of Material Science and Engineering at Purdue University.

The nanoparticles were placed at a fixed distance of $2\mathring{A}$ to ensure the nanoparticles sense each other and sinter at all the sizes and temperatures monitored here. All the nanoparticle pairs followed the same behavior of initial contact, neck formation and finally merging completely. Smaller particle size and higher temperature promote a complete sintering, whereas bigger particles tend to form a neck at lower temperatures. Figure 6.8 shows the snapshot of the final structure of 3 pairs of nanoparticles at three temperatures.

The radius of gyration monitors the shapes of the combined nanoparticles through the sintering process. $R_g^2 = \frac{1}{M}\sum_{i=1}^{N} m_i \left(r_i - r_{cm}\right)$ where R_g is the radius of gyration, N the total number of atoms, M the mass of both of nanoparticles and r_{cm} is the position of the center of mass of the system. During sintering, the atomic diffusion leads to the change in the shape of the nanoparticles from perfect sphere. The temperature and the initial size have a strong effect on the radius of gyration.

Another important quantity is the mean square displacement (MSD). It measures the distance the nanoparticles travel in the sintering process. It is given by $MSD = \frac{1}{N}\sum_{i=1}^{N}\left(r_i\left(t\right) - r_i\left(0\right)\right)^2$ where N is the number of atoms sampled, r(t) is the atom position at a given time t. The smaller nanoparticle pairs have higher MSD compared to larger nanoparticles in the case of same sized pairs. In case of unequal sized pairs, MSD does not follow a trend.

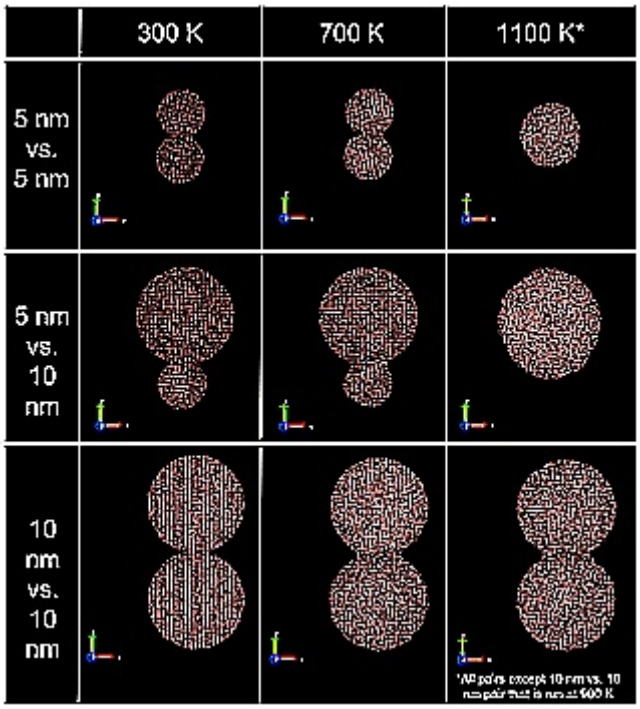

Figure 6.8. Snapshots of the final structure of nanoparticles at t = 100 ps for three different pairs at three different temperatures.

Similar studies have been carried out by different groups [59,166]. Yang et al. [166] have made use of EAM potential to simulate sintering of gold nanoparticles by laser heating from 298K to 1098 K. The effect of initial size and heating rates on the neck formation, radius of gyration and mean square displacement were discussed. They also monitored the local structure in the neck region and found that most fcc structures are replaced by hcp structure undergoing deformation and surface diffusion during annealing. Further simulations are required to understand the sintering process, to calculate the coefficient of diffusion, and to predict parameters that control the grain growth in these metallic nanoparticles. These studies can be verified experimentally by *in situ* transmission electron microscopy [116].

7. SUMMARY

Nanoalloys have many interesting applications in various fields due to their unique properties emerging from size effects on electronic structure. However, manipulation and control of nano-material properties require a deeper understanding of its atomic structure including particle size, shape, chemical ordering, and element distribution on the surface and in the volume of the nanoparticles. The goal of this thesis was to understand the modifications of well-known structural transformations in the nanoscale regime. This study focused on understanding the structural intricacies of nanoparticle catalysts with applications in fuel cells. Thermal treatment is a substantial part of the nanocatalyst synthesis procedure and plays an important role in determining the structure-properties correlations of multi-metallic nanoparticles. The main structural changes detailed in this work are primarily solid phase transformations, specifically coalescence, chemical ordering, surface segregation, grain growth, and lattice contraction. The structural evolution of multi-metallic nanoparticles was monitored using *in situ* time resolved x-ray diffraction complemented by ex situ transmission electron microscopy. Understanding the structure formed during thermal treatment is important for explaining the functional aspects of catalysts. In most cases the higher mass activity of multi-metallic nanoparticles was found to be correlated with the formation of uniform random alloys. The phase diagram of two multi-metallic systems was also explored for nanoscale systems. Furthermore, our work showed that it is possible to tailor the structural evolution of multi-metallic nanoparticles through the choice of supporting substrates and annealing conditions.

Chapter 4 focused on kinetic processes occurring during high-temperature annealing of PtNiCo nanocatalysts. PtNiCo nanoparticles of various sizes (2.6 - 6.1 nm) and compositions around 50% Co were synthesized by a combination of molecular encapsulation, reduction/decomposition, and thermal processing protocols. We found

that sintering of PtNiCo nanoparticles occurs in two distinct stages. In the first stage the coalescence is driven by surface reduction similar to the one observed in the case of pure Pt nanoparticles. In the second stage, the grains grow significantly and the process is driven by grain boundary diffusion. The second stage was compared with existing growth models to get insight into the kinetics of grain growth. Each stage is characterized by additional size-dependent transformations (chemical ordering, lattice shrinking) that are critical for the chemical performance of the nanomaterials. These high-temperature induced structural changes grain growth, phase changes, lattice shrinkage and chemical ordering are probably responsible for the enhanced electrocatalytic activity of annealed PtNiCo trimetallic nanoparticles. Ternary alloy compositions similar to the ones used in our study ($Pt_xNi_{100-x-y}Co_y$, x = 28 - 44%, y = 40 - 54%) were found in a separate study to exhibit four times the mass activity, with almost twice the stability of a commercial Pt/C catalyst when thermally annealed above 700°C. Our experiments and analysis provide the tools to estimate the activation energy for grain boundary diffusion and to predict the size of the nanoparticles as a function of thermal treatment time and temperature.

Chapter 5 examined alloying in Pd:Cu mixtures and found it to be different from the evolution of PdCu alloy nanoparticles. Pd and Cu nanoparticles capped with decanthiolate monolayers were synthesized separately and mixed by volume for obtaining different compositions. The nanoparticle mixtures were then dispersed on several types of substrates: SiO_2/Si, carbon black, and alumina. The Pd:Cu = 1:3 nanoparticle mixtures supported on silica and carbon black intermix when annealed at 300°C to form a chemically ordered CsCl-type (B2) alloy phase. The B2 phase transforms into a disordered fcc alloy at higher temperature (>550°C). The alloy nanoparticles obtained from nanoparticle mixtures and supported on silica and carbon black are homogeneous in volume, but evidence was found of slight Pd surface enrichment using STEM-EDX. The high catalytic activity of PdCu in EOR was attributed to this Pd surface enrichment on PdCu alloy nanoparticles. When supported on alumina, the two metals segregated at 300°C to produce almost pure fcc Cu and

Pd phases. Upon further annealing of the mixture on alumina above 600°C, the two metals interdiffused, forming two distinct disordered alloys of compositions 30% and 90% Pd. In Pd:Cu 1:1 mixtures, the B2 phase dramatically transforms into two different disordered alloys of different compositions, one rich in Pd and another rich in Cu. This behavior contrasts sharply with the behavior of bulk PdCu alloys of the same composition. For Pd:Cu 3:1 composition, a disordered fcc phase and the B2 phase are formed simultaneously at 450°C. Upon further annealing to 750°C, the disordered fcc phase grows at the expense of the B2 phase. Phase transition and grain growth can be manipulated with a combination of supporting substrate and annealing atmosphere.

This thesis is testimony to the rapid recent progress in understanding the structure-function relationship in multi-metallic nanoparticles. However, there are many aspects that remain to be explored. From the experimental point of view, a few research directions are worth pursuing. Of particular importance are the experiments to monitor the nanocatalyst evolution *in situ* and in operando. Transmission electron microscopy equipped with aberration correction and capabilities to do high resolution imaging *in situ* during temperature changes and in different gas atmospheres can provide additional structural information about thermally induced transformations. Synchrotron based *in situ* X-ray absorption spectroscopy is another experimental technique that provides understanding of the electronic structure of multi-metallic nanoparticles. With all experimental techniques is important to survey and test a wide variety of multi-metallic nanoparticles of noble and transition metals with different compositions, size, shape, temperature, substrates, annealing atmosphere and other relevant parameters. Finally, extensive catalytic studies are required to connect the reaction mechanisms and functionalities with *in situ* structural characterization of these nanocatalysts. The combination of all experimental techniques will in the future help in building a consensus on the exact effects of structural parameters on catalytic performance.

In addition to experimental studies, computer simulations using full scale density functional theory and molecular dynamics calculations can shine light on the interaction of the nanoparticles with each other and with different kinds of substrates and annealing atmospheres. Some of the studies carried out by other research groups were briefly discussed in chapter 1 and 2. A brief section in chapter 6 described our limited efforts in this direction. However, a full computational study was beyond the scope of this thesis.

REFERENCES

REFERENCES

[1] Riccardo Ferrando, Julius Jellinek, and Roy L Johnston. Nanoalloys: from theory to applications of alloy clusters and nanoparticles. *Chemical Reviews*, 108(3):845–910, 2008.

[2] Chuan-Jian Zhong, Jin Luo, Peter N Njoki, Derrick Mott, Bridgid Wanjala, Rameshwori Loukrakpam, Stephanie Lim, Lingyan Wang, Bin Fang, and Zhichuan Xu. Fuel cell technology: nano-engineered multimetallic catalysts. *Energy & Environmental Science*, 1(4):454–466, 2008.

[3] Gabor A Somorjai and Keith McCrea. Roadmap for catalysis science in the 21st century: a personal view of building the future on past and present accomplishments. *Applied Catalysis A: General*, 222(1):3–18, 2001.

[4] D. Alloyeau, C. Mottet, and C. Ricolleau. *Nanoalloys: Synthesis, Structure and Properties*. Engineering Materials. Springer, 2012.

[5] Han-Wei Lei, Sanghyuk Suh, Bogdan Gurau, Bizuneh Workie, Renxuan Liu, and Eugene S Smotkin. Deuterium isotope analysis of methanol oxidation on mixed metal anode catalysts. *Electrochimica acta*, 47(18):2913–2919, 2002.

[6] Shengzhou Chen, Fei Ye, and Weiming Lin. Effect of operating conditions on the performance of a direct methanol fuel cell with ptrumo/cnts as anode catalyst. *International Journal of Hydrogen Energy*, 35(15):8225–8233, 2010.

[7] A Naitabdi, LK Ono, and B Roldan Cuenya. Local investigation of the electronic properties of size-selected au nanoparticles by scanning tunneling spectroscopy. *Applied physics letters*, 89(4):043101, 2006.

[8] Gabor A Somorjai and Jeong Y Park. Colloid science of metal nanoparticle catalysts in 2d and 3d structures. challenges of nucleation, growth, composition, particle shape, size control and their influence on activity and selectivity. *Topics in Catalysis*, 49(3-4):126–135, 2008.

[9] AK Santra and DW Goodman. Oxide-supported metal clusters: models for heterogeneous catalysts. *Journal of Physics: Condensed Matter*, 15(2):R31, 2003.

[10] Ayman M Karim, Vinay Prasad, Giannis Mpourmpakis, William W Lonergan, Anatoly I Frenkel, Jingguang G Chen, and Dionisios G Vlachos. Correlating particle size and shape of supported ru/γ-al2o3 catalysts with nh3 decomposition activity. *Journal of the American Chemical Society*, 131(34):12230–12239, 2009.

[11] U Heiz, A Sanchez, S Abbet, and W-D Schneider. Catalytic oxidation of carbon monoxide on monodispersed platinum clusters: each atom counts. *Journal of the American Chemical Society*, 121(13):3214–3217, 1999.

[12] Michel Che and Carroll O Bennett. of supported metals. *Advances in Catalysis*, 36:55, 1989.

[13] Francesca Baletto and Riccardo Ferrando. Structural properties of nanoclusters: energetic, thermodynamic, and kinetic effects. *Reviews of modern physics*, 77(1):371, 2005.

[14] F Baletto, R Ferrando, A Fortunelli, F Montalenti, and C Mottet. Crossover among structural motifs in transition and noble-metal clusters. *The Journal of chemical physics*, 116(9):3856–3863, 2002.

[15] Radha Narayanan and Mostafa A El-Sayed. Shape-dependent catalytic activity of platinum nanoparticles in colloidal solution. *Nano Letters*, 4(7):1343–1348, 2004.

[16] Run Xu, Dingsheng Wang, Jiatao Zhang, and Yadong Li. Shape-dependent catalytic activity of silver nanoparticles for the oxidation of styrene. *Chemistry–An Asian Journal*, 1(6):888–893, 2006.

[17] Na Tian, Zhi-You Zhou, Shi-Gang Sun, Yong Ding, and Zhong Lin Wang. Synthesis of tetrahexahedral platinum nanocrystals with high-index facets and high electro-oxidation activity. *science*, 316(5825):732–735, 2007.

[18] H-J Freund, M Bäumer, and H Kuhlenbeck. Catalysis and surface science: What do we learn from studies of oxide-supported cluster model systems? *Advances in Catalysis*, 45:333–384, 2000.

[19] DR Strongin, J Carrazza, Simon R Bare, and GA Somorjai. The importance of c¡ sub¿ 7¡/sub¿ sites and surface roughness in the ammonia synthesis reaction over iron. *Journal of Catalysis*, 103(1):213–215, 1987.

[20] R Van Hardeveld and F Hartog. The statistics of surface atoms and surface sites on metal crystals. *Surface Science*, 15(2):189–230, 1969.

[21] H-J Freund, J Libuda, M Bäumer, T Risse, and A Carlsson. Cluster, facets, and edges: Site-dependent selective chemistry on model catalysts. *The Chemical Record*, 3(3):181–201, 2003.

[22] Rutger A Van Santen. Complementary structure sensitive and insensitive catalytic relationships. *Accounts of chemical research*, 42(1):57–66, 2008.

[23] Feng Tao, Sefa Dag, Lin-Wang Wang, Zhi Liu, Derek R Butcher, Hendrik Bluhm, Miquel Salmeron, and Gabor A Somorjai. Break-up of stepped platinum catalyst surfaces by high co coverage. *Science*, 327(5967):850–853, 2010.

[24] PJ Ferreira, Y Shao-Horn, D Morgan, R Makharia, S Kocha, HA Gasteiger, et al. Instability of pt/ c electrocatalysts in proton exchange membrane fuel cells a mechanistic investigation. *Journal of The Electrochemical Society*, 152(11):A2256–A2271, 2005.

[25] Markus M Schubert, Stefan Hackenberg, Andre C Van Veen, Martin Muhler, Vojtech Plzak, and R Jürgen Behm. Co oxidation over supported gold catalystsinert and active support materials and their role for the oxygen supply during reaction. *Journal of Catalysis*, 197(1):113–122, 2001.

[26] Bokwon Yoon, Hannu Häkkinen, Uzi Landman, Anke S Wörz, Jean-Marie Antonietti, Stéphane Abbet, Ken Judai, and Ueli Heiz. Charging effects on bonding and catalyzed oxidation of co on au8 clusters on mgo. *Science*, 307(5708):403–407, 2005.

[27] GM Pajonk. Contribution of spillover effects to heterogeneous catalysis. *Applied Catalysis A: General*, 202(2):157–169, 2000.

[28] JA Rodriguez, S Ma, P Liu, J Hrbek, J Evans, and M Perez. Activity of ceox and tiox nanoparticles grown on au (111) in the water-gas shift reaction. *Science*, 318(5857):1757–1760, 2007.

[29] Wenfu Yan, Bei Chen, Shannon M Mahurin, Sheng Dai, and Steven H Overbury. Brookite-supported highly stable gold catalytic system for co oxidation. *Chemical Communications*, (17):1918–1919, 2004.

[30] F Maire, M Capelle, G Meunier, JF Beziau, D Bazin, H Dexpert, F Garin, JL Schmitt, and G Maire. An x-ray absorption spectroscopic investigation of aged automotive catalysts. *Studies in Surface Science and Catalysis*, 96:749–762, 1995.

[31] Zhiqiang Niu, Qing Peng, Ming Gong, Hongpan Rong, and Yadong Li. Oleylamine-mediated shape evolution of palladium nanocrystals. *Angewandte Chemie*, 123(28):6439–6443, 2011.

[32] Bin Shan, Jangsuk Hyun, Neeti Kapur, and Kyeongjae Cho. First-principles study of pdau segregation with co coverage. In *MRS Proceedings*, volume 1177, pages 1177–Z02. Cambridge Univ Press, 2009.

[33] Junyang Xian, Qing Hua, Zhiquan Jiang, Yunsheng Ma, and Weixin Huang. Size-dependent interaction of the poly (n-vinyl-2-pyrrolidone) capping ligand with pd nanocrystals. *Langmuir*, 28(17):6736–6741, 2012.

[34] Theodore E Madey, Wenhua Chen, Hao Wang, Payam Kaghazchi, and Timo Jacob. Nanoscale surface chemistry over faceted substrates: structure, reactivity and nanotemplates. *Chemical Society Reviews*, 37(10):2310–2327, 2008.

[35] M Cabie, S Giorgio, CR Henry, M Rosa Axet, K Philippot, and B Chaudret. Direct observation of the reversible changes of the morphology of pt nanoparticles under gas environment. *The Journal of Physical Chemistry C*, 114(5):2160–2163, 2010.

[36] Xiaoyan Liu, Aiqin Wang, Lin Li, Tao Zhang, Chung-Yuan Mou, and Jyh-Fu Lee. Structural changes of au–cu bimetallic catalysts in co oxidation: In situ xrd, epr, xanes, and ft-ir characterizations. *Journal of Catalysis*, 278(2):288–296, 2011.

[37] David E Starr, Shamil K Shaikhutdinov, and Hans-Joachim Freund. Gold supported on oxide surfaces: environmental effects as studied by stm. *Topics in catalysis*, 36(1-4):33–41, 2005.

[38] P Nolte, A Stierle, NY Jin-Phillipp, N Kasper, TU Schulli, and H Dosch. Shape changes of supported rh nanoparticles during oxidation and reduction cycles. *Science*, 321(5896):1654–1658, 2008.

[39] LAURO OLIVER Paz-Borbon, RL Johnston, GIOVANNI Barcaro, and ALESSANDRO Fortunelli. Chemisorption of co and h on pd, pt and au nanoclusters: a dft approach. *The European Physical Journal D-Atomic, Molecular, Optical and Plasma Physics*, 52(1):131–134, 2009.

[40] Vasiliki Papaefthimiou, Thierry Dintzer, Véronique Dupuis, Alexandre Tamion, Florent Tournus, Detre Teschner, Michael Havecker, Axel Knop-Gericke, Robert Schlogl, and Spiros Zafeiratos. When a metastable oxide stabilizes at the nanoscale: wurtzite coo formation upon dealloying of ptco nanoparticles. *The Journal of Physical Chemistry Letters*, 2(8):900–904, 2011.

[41] A Hamnett. Mechanism and electrocatalysis in the direct methanol fuel cell. *Catalysis Today*, 38(4):445–457, 1997.

[42] Jason R Croy, S Mostafa, L Hickman, H Heinrich, and B Roldan Cuenya. Bimetallic pt-metal catalysts for the decomposition of methanol: Effect of secondary metal on the oxidation state, activity, and selectivity of pt. *Applied Catalysis A: General*, 350(2):207–216, 2008.

[43] Vojislav R Stamenkovic, Bongjin Simon Mun, Matthias Arenz, Karl JJ Mayrhofer, Christopher A Lucas, Guofeng Wang, Philip N Ross, and Nenad M Markovic. Trends in electrocatalysis on extended and nanoscale pt-bimetallic alloy surfaces. *Nature materials*, 6(3):241–247, 2007.

[44] Laurent Piccolo, Agnes Piednoir, and Jean-Claude Bertolini. Pd–au single-crystal surfaces: segregation properties and catalytic activity in the selective hydrogenation of 1, 3-butadiene. *Surface science*, 592(1):169–181, 2005.

[45] A Bensaddik, A Caballero, D Bazin, H Dexpert, B Didillon, and J Lynch. In situ study by xas of the sulfidation of industrial catalysts: the pt and ptreal2o3 systems. *Applied Catalysis A: General*, 162(1):171–180, 1997.

[46] Heechang Ye and Richard M Crooks. Effect of elemental composition of ptpd bimetallic nanoparticles containing an average of 180 atoms on the kinetics of the electrochemical oxygen reduction reaction. *Journal of the American Chemical Society*, 129(12):3627–3633, 2007.

[47] SM Davis, F Zaera, and GA Somorjai. The reactivity and composition of strongly adsorbed carbonaceous deposits on platinum. model of the working hydrocarbon conversion catalyst. *Journal of Catalysis*, 77(2):439–459, 1982.

[48] O Ducreux, B Rebours, J Lynch, M Roy-Auberger, and D Bazin. Microstructure of supported cobalt fischer-tropsch catalysts. *Oil & Gas Science and Technology-Revue de l'IFP*, 64(1):49–62, 2009.

[49] Lin Gan, Ruitao Lv, Hongda Du, Baohua Li, and Feiyu Kang. High loading of pt–ru nanocatalysts by pentagon defects introduced in a bamboo-shaped carbon nanotube support for high performance anode of direct methanol fuel cells. *Electrochemistry Communications*, 11(2):355–358, 2009.

[50] Karl JJ Mayrhofer, Viktorija Juhart, Katrin Hartl, Marianne Hanzlik, and Matthias Arenz. Adsorbate-induced surface segregation for core–shell nanocatalysts. *Angewandte Chemie International Edition*, 48(19):3529–3531, 2009.

[51] P Miegge, JL Rousset, B Tardy, J Massardier, and JC Bertolini. Pd¡ sub¿ 1¡/sub¿ ni¡ sub¿ 99¡/sub¿ and pd¡ sub¿ 5¡/sub¿ ni¡ sub¿ 95¡/sub¿: Pd surface segregation and reactivity for the hydrogenation of 1, 3-butadiene. *Journal of Catalysis*, 149(2):404–413, 1994.

[52] David A. Porter, Kenneth E. Easterling, and Mohamed Sherif. *Phase Transformations in Metals and Alloys, Third Edition (Revised Reprint)*. Taylor & Francis, 2009.

[53] R.E. Smallman and R.J. Bishop. *Modern Physical Metallurgy and Materials Engineering: Science, Process, Applications*. Referex Engineering. Butterworth-Heinemann, 1999.

[54] D. Vollath. *Nanomaterials: An Introduction to Synthesis, Properties and Applications*. Wiley, 2008.

[55] G.A. Somorjai and Y. Li. *Introduction to Surface Chemistry and Catalysis*. John Wiley & Sons, 2010.

[56] Ph Buffat and Jean Pierre Borel. Size effect on the melting temperature of gold particles. *Physical Review A*, 13(6):2287, 1976.

[57] Reinhard Lipowsky. Critical phenomena at surfaces and interfaces. In *Ordered IntermetallicsPhysical Metallurgy and Mechanical Behaviour*, pages 107–121. Springer, 1992.

[58] QS Mei and K Lu. Melting and superheating of crystalline solids: from bulk to nanocrystals. *Progress in Materials Science*, 52(8):1175–1262, 2007.

[59] Ling Miao, Venkat R Bhethanabotla, and Babu Joseph. Melting of pd clusters and nanowires: A comparison study using molecular dynamics simulation. *Physical Review B*, 72(13):134109, 2005.

[60] Fuyi Chen, Benjamin C Curley, Giulia Rossi, and Roy L Johnston. Structure, melting, and thermal stability of 55 atom ag-au nanoalloys. *The Journal of Physical Chemistry C*, 111(26):9157–9165, 2007.

[61] F Delogu. The mechanism of chemical disordering in cu3au nanometre-sized systems. *Nanotechnology*, 18(23):235706, 2007.

[62] Fuyi Chen, Benjamin C Curley, Giulia Rossi, and Roy L Johnston. Structure, melting, and thermal stability of 55 atom ag-au nanoalloys. *The Journal of Physical Chemistry C*, 111(26):9157–9165, 2007.

[63] Subramanian KRS Sankaranarayanan, Venkat R Bhethanabotla, and Babu Joseph. Molecular dynamics simulation study of the melting of pd-pt nanoclusters. *Physical Review B*, 71(19):195415, 2005.

[64] Julius Jellinek. Nanoalloys: tuning properties and characteristics through size and composition. *Faraday discussions*, 138:11–35, 2008.

[65] Alvaro Mayoral, Francis Leonard Deepak, Rodrigo Esparza, Gilberto Casillas, Cesar Magen, Eduardo Perez-Tijerina, and Miguel Jose-Yacaman. On the structure of bimetallic noble metal nanoparticles as revealed by aberration corrected scanning transmission electron microscopy (stem). *Micron*, 43(4):557–564, 2012.

[66] Daojian Cheng and Dapeng Cao. Structural transition and melting of onion-ring pd–pt bimetallic clusters. *Chemical Physics Letters*, 461(1):71–76, 2008.

[67] Pascal Andreazza, Christine Mottet, Caroline Andreazza-Vignolle, Jose Penuelas, Helio CN Tolentino, Maurizio De Santis, Roberto Felici, and Nathalie Bouet. Probing nanoscale structural and order/disorder phase transitions of supported co-pt clusters under annealing. *Physical Review B*, 82(15):155453, 2010.

[68] Giovanni Barcaro, Alessandro Fortunelli, Micha Polak, and Leonid Rubinovich. Patchy multishell segregation in pd- pt alloy nanoparticles. *Nano letters*, 11(4):1766–1769, 2011.

[69] Lauro Oliver Paz-Borbón, Roy L Johnston, Giovanni Barcaro, and Alessandro Fortunelli. A mixed structural motif in 34-atom pd-pt clusters. *The Journal of Physical Chemistry C*, 111(7):2936–2941, 2007.

[70] Marcelo M Mariscal, Sergio A Dassie, and Ezequiel PM Leiva. Collision as a way of forming bimetallic nanoclusters of various structures and chemical compositions. *The Journal of chemical physics*, 123(18):184505, 2005.

[71] C Mottet, G Tréglia, and B Legrand. Theoretical investigation of chemical and morphological ordering in pd c cu 1-c clusters. *Physical Review B*, 66(4):045413, 2002.

[72] Ch Ricolleau, A Loiseau, F Ducastelle, and R Caudron. Logarithmic divergence of the antiphase boundary width in cu-pd (17%). *Physical review letters*, 68(24):3591, 1992.

[73] D Le Floc'h, A Loiseau, Ch Ricolleau, C Barreteau, R Caudron, F Ducastelle, and JM Pénisson. Critical behavior of antiphase boundaries in fe 3 al close to the do 3 b 2 phase transition. *Physical review letters*, 81(11):2272, 1998.

[74] AS Barnard. Modelling of nanoparticles: approaches to morphology and evolution. *Reports on Progress in Physics*, 73(8):086502, 2010.

[75] G Rossi, A Rapallo, C Mottet, A Fortunelli, F Baletto, and R Ferrando. Magic polyicosahedral core-shell clusters. *Physical review letters*, 93(10):105503, 2004.

[76] Giovanni Barcaro, Riccardo Ferrando, Alessandro Fortunelli, and Giulia Rossi. Exotic supported copt nanostructures: from clusters to wires. *The Journal of Physical Chemistry Letters*, 1(1):111–115, 2009.

[77] Laurent J Lewis, Pablo Jensen, and Jean-Louis Barrat. Melting, freezing, and coalescence of gold nanoclusters. *Physical Review B*, 56(4):2248, 1997.

[78] FA Nichols and WW Mullins. Morphological changes of a surface of revolution due to capillarity-induced surface diffusion. *Journal of Applied Physics*, 36(6):1826–1835, 1965.

[79] FRENKEL Ya. Viscous flow of crystalline bodies under the action of surface tension. *SCI. SINTERING Sci. Sintering*, 12(1):7, 1980.

[80] T Hawa and MR Zachariah. Molecular dynamics simulation and continuum modeling of straight-chain aggregate sintering: Development of a phenomenological scaling law. *Physical Review B*, 76(5):054109, 2007.

[81] S.J.L. Kang. *Sintering: Densification, Grain Growth and Microstructure*. Elsevier Science, 2004.

[82] Conyers Herring. Diffusional viscosity of a polycrystalline solid. *Journal of Applied Physics*, 21(5):437–445, 1950.

[83] W_ D_ Kingery and Morris Berg. Study of the initial stages of sintering solids by viscous flow, evaporation-condensation, and self-diffusion. *Journal of Applied Physics*, 26(10):1205–1212, 1955.

[84] RL Coble. Initial sintering of alumina and hematite. *Journal of the American Ceramic Society*, 41(2):55–62, 1958.

[85] George C Kuczynski. Self-diffusion in sintering of metallic particles. *AIME TRANS*, 185:169–178, 1949.

[86] R.M. German. *Sintering Theory and Practice*. A Wiley-Interscience publication. Wiley, 1996.

[87] WS Coblenz, JM Dynys, RM Cannon, and RL Coble. Initial stage solid state sintering models. a critical analysis and assessment. *Sintering Processes. Materials Science Research*, 13:141–157, 1980.

[88] Yangchuan Xing and Daniel E Rosner. Prediction of spherule size in gas phase nanoparticle synthesis. *Journal of Nanoparticle Research*, 1(2):277–291, 1999.

[89] Huilong Zhu and RS Averback. Sintering of nano-particle powders: simulations and experiments. *MATERIAL AND MANUFACTURING PROCESS*, 11(6):905–923, 1996.

[90] S Arcidiacono, NR Bieri, D Poulikakos, and CP Grigoropoulos. On the coalescence of gold nanoparticles. *International Journal of Multiphase Flow*, 30(7):979–994, 2004.

[91] Gregory Grochola, Salvy P Russo, and Ian K Snook. On morphologies of gold nanoparticles grown from molecular dynamics simulation. *The Journal of chemical physics*, 126(16):164707, 2007.

[92] Chin-Lung Kuo and Paulette Clancy. Melting and freezing characteristics and structural properties of supported and unsupported gold nanoclusters. *The Journal of Physical Chemistry B*, 109(28):13743–13754, 2005.

[93] Hidehiro Yasuda, Hirotaro Mori, Masao Komatsu, Kiyoko Takeda, and Hiroshi Fujita. In situ observation of spontaneous alloying in atom clusters. *Journal of electron microscopy*, 41(4):267–269, 1992.

[94] Yasushi Shimizu, Kensuke S Ikeda, and Shin-ichi Sawada. Spontaneous alloying in binary metal microclusters: A molecular dynamics study. *Physical Review B*, 64(7):075412, 2001.

[95] Shin-ichi Sawada, Yasushi Shimizu, and Kensuke S Ikeda. Molecular-dynamics simulations of rapid alloying of microclusters using a many-body potential. *Physical Review B*, 67(2):024204, 2003.

[96] M Brust, J Fink, D Bethell, DJ Schiffrin, and C Kiely. Synthesis and reactions of functionalised gold nanoparticles. *J. Chem. Soc., Chem. Commun.*, (16):1655–1656, 1995.

[97] Mathias Brust, Merryl Walker, Donald Bethell, David J Schiffrin, and Robin Whyman. Synthesis of thiol-derivatised gold nanoparticles in a two-phase liquid–liquid system. *J. Chem. Soc., Chem. Commun.*, (7):801–802, 1994.

[98] Zhiqiang Niu and Yadong Li. Removal and utilization of capping agents in nanocatalysis. *Chemistry of Materials*, 26(1):72–83, 2013.

[99] Charles Kittel. *Introduction to Solid State Physics*. Wiley, 2005.

[100] B.E. Warren. *X-Ray Diffraction*. Dover Books on Physics. Dover Publications, 2012.

[101] R.E. Dinnebier and S.J.L. Billinge. *Powder Diffraction: Theory and Practice*. Royal Society of Chemistry, 2008.

[102] LA Clevenger, RA Roy, C Cabral, KL Saenger, S Brauer, G Morales, KF Ludwig, G Gifford, J Bucchignano, J Jordan-Sweet, et al. A comparison of c54-tisi2 formation in blanket and submicron gate structures using in situ x-ray diffraction during rapid thermal annealing. *Journal of materials research*, 10(09):2355–2359, 1995.

[103] Jean L Jordan-Sweet. Synchrotron x-ray scattering techniques for microelectronics-related materials studies. *IBM Journal of Research and Development*, 44(4):457–476, 2000.

[104] Holger Borchert, Elena V Shevchenko, Aymeric Robert, Ivo Mekis, Andreas Kornowski, Gerhard Grübel, and Horst Weller. Determination of nanocrystal sizes: a comparison of tem, saxs, and xrd studies of highly monodisperse copt3 particles. *Langmuir*, 21(5):1931–1936, 2005.

[105] Alan R Denton and Neil W Ashcroft. Vegards law. *Physical Review A*, 43(6):3161, 1991.

[106] D.B. Williams and C.B. Carter. *Transmission Electron Microscopy: A Textbook for Materials Science*. Number v. 3 in Cambridge library collection. Springer, 2009.

[107] J. Regalbuto. *Catalyst Preparation: Science and Engineering*. Taylor & Francis, 2006.

[108] H Bonnemann and KS Nagabhushana. Advantageous fuel cell catalysts from colloidal nanometals. *Journal of New Materials for Electrochemical Systems*, 7(2):93–108, 2004.

[109] Rameshwori Loukrakpam, Jin Luo, Ting He, Yongsheng Chen, Zhichuan Xu, Peter N Njoki, Bridgid N Wanjala, Bin Fang, Derrick Mott, Jun Yin, et al. Nanoengineered ptco and ptni catalysts for oxygen reduction reaction: an assessment of the structural and electrocatalytic properties. *The Journal of Physical Chemistry C*, 115(5):1682–1694, 2011.

[110] Bridgid N Wanjala, Rameshwori Loukrakpam, Jin Luo, Peter N Njoki, Derrick Mott, Chuan-Jian Zhong, Minhua Shao, Lesia Protsailo, and Tetsuo Kawamura. Thermal treatment of ptnico electrocatalysts: Effects of nanoscale strain and structure on the activity and stability for the oxygen reduction reaction. *The Journal of Physical Chemistry C*, 114(41):17580–17590, 2010.

[111] Nigel P Brandon, S Skinner, and Brian CH Steele. Recent advances in materials for fuel cells. *Annual Review of Materials Research*, 33(1):183–213, 2003.

[112] Ermete Antolini. Platinum-based ternary catalysts for low temperature fuel cells: Part i. preparation methods and structural characteristics. *Applied Catalysis B: Environmental*, 74(3):324–336, 2007.

[113] ZZ Fang and H Wang. Densification and grain growth during sintering of nanosized particles. *International Materials Reviews*, 53(6):326–352, 2008.

[114] Roger Ristau, Ramchandra Tiruvalam, Patrick L Clasen, Edward P Gorskowski, Martin P Harmer, Christopher J Kiely, Irshad Hussain, and Mathias Brust. Electron microscopy studies of the thermal stability of gold nanoparticle arrays. *Gold Bulletin*, 42(2):133–143, 2009.

[115] Bridget Ingham, Teck H Lim, Christian J Dotzler, Anna Henning, Michael F Toney, and Richard D Tilley. How nanoparticles coalesce: an in situ study of au nanoparticle aggregation and grain growth. *Chemistry of Materials*, 23(14):3312–3317, 2011.

[116] MA Asoro, D Kovar, Y Shao-Horn, LF Allard, and PJ Ferreira. Coalescence and sintering of pt nanoparticles: in situ observation by aberration-corrected haadf stem. *Nanotechnology*, 21(2):025701, 2010.

[117] Charles T Campbell, Stephen C Parker, and David E Starr. The effect of size-dependent nanoparticle energetics on catalyst sintering. *Science*, 298(5594):811–814, 2002.

[118] O Malis, C Byard, D Mott, BN Wanjala, R Loukrakpam, J Luo, and CJ Zhong. Low-temperature phase and morphology transformations in noble metal nanocatalysts. *Nanotechnology*, 22(2):025701, 2011.

[119] Jun Yin, Peipei Hu, Bridgid Wanjala, Oana Malis, and Chuan-Jian Zhong. Harnessing molecule–solid duality of nanoclusters/nanoparticles for nanoscale control of size, shape and alloying. *Chemical Communications*, 47(35):9885–9887, 2011.

[120] O Malis, M Radu, D Mott, B Wanjala, J Luo, and CJ Zhong. An in situ real-time x-ray diffraction study of phase segregation in au–pt nanoparticles. *Nanotechnology*, 20(24):245708, 2009.

[121] Bridgid N Wanjala, Jin Luo, Rameshwori Loukrakpam, Bin Fang, Derrick Mott, Peter N Njoki, Mark Engelhard, H Richard Naslund, Jia Kai Wu, Lichang Wang, et al. Nanoscale alloying, phase-segregation, and core- shell evolution of gold- platinum nanoparticles and their electrocatalytic effect on oxygen reduction reaction. *Chemistry of Materials*, 22(14):4282–4294, 2010.

[122] T Hawa and MR Zachariah. Development of a phenomenological scaling law for fractal aggregate sintering from molecular dynamics simulation. *Journal of Aerosol Science*, 38(8):793–806, 2007.

[123] Kari EJ Lehtinen and Michael R Zachariah. Effect of coalescence energy release on the temporal shape evolution of nanoparticles. *Physical Review B*, 63(20):205402, 2001.

[124] H Natter, M Schmelzer, M-S Löffler, CE Krill, A Fitch, and R Hempelmann. Grain-growth kinetics of nanocrystalline iron studied in situ by synchrotron real-time x-ray diffraction. *The Journal of Physical Chemistry B*, 104(11):2467–2476, 2000.

[125] O Yevtushenko, H Natter, and R Hempelmann. Grain-growth kinetics of nanostructured gold. *Thin solid films*, 515(1):353–356, 2006.

[126] Andreas Michels, CE Krill, H Ehrhardt, R Birringer, and DT Wu. Modelling the influence of grain-size-dependent solute drag on the kinetics of grain growth in nanocrystalline materials. *Acta materialia*, 47(7):2143–2152, 1999.

[127] K. Kinoshita. *Electrochemical Oxygen Technology*. The ECS Series of Texts and Monographs. John Wiley & Sons, 1992.

[128] Bernard Coq and François Figueras. Bimetallic palladium catalysts: influence of the co-metal on the catalyst performance. *Journal of Molecular Catalysis A: Chemical*, 173(1):117–134, 2001.

[129] Xiaoping Wang, Nancy Kariuki, John T Vaughey, Jason Goodpaster, Romesh Kumar, and Deborah J Myers. Bimetallic pd–cu oxygen reduction electrocatalysts. *Journal of The Electrochemical Society*, 155(6):B602–B609, 2008.

[130] Natalie Pomerantz, Yi Hua Ma, and E Andrew Payzant. Isothermal solid-state transformation kinetics applied to pd/cu alloy membrane fabrication. *AIChE journal*, 56(12):3062–3073, 2010.

[131] Elise B Fox, Subramani Velu, Mark H Engelhard, Ya-Huei Chin, Jeffrey T Miller, Jeremy Kropf, and Chunshan Song. Characterization of ceo¡ sub¿ 2¡/sub¿-supported cu–pd bimetallic catalyst for the oxygen-assisted water–gas shift reaction. *Journal of Catalysis*, 260(2):358–370, 2008.

[132] L Guczi, Z Schay, Gy Stefler, LF Liotta, G Deganello, and AM Venezia. Pumice-supported cu–pd catalysts: influence of copper on the activity and selectivity of palladium in the hydrogenation of phenylacetylene and but-1-ene. *Journal of Catalysis*, 182(2):456–462, 1999.

[133] Nancy N Kariuki, Xiaoping Wang, Jennifer R Mawdsley, Magali S Ferrandon, Suhas G Niyogi, John T Vaughey, and Deborah J Myers. Colloidal synthesis and characterization of carbon-supported pd- cu nanoparticle oxygen reduction electrocatalysts. *Chemistry of Materials*, 22(14):4144–4152, 2010.

[134] Jun Yin, Shiyao Shan, Mei Shan Ng, Lefu Yang, Derrick Mott, Weiqin Fang, Ning Kang, Jin Luo, and Chuan-Jian Zhong. Catalytic and electrocatalytic oxidation of ethanol over palladium-based nanoalloy catalysts. *Langmuir*, 29(29):9249–9258, 2013.

[135] Zhen Yin, Wu Zhou, Yongjun Gao, Ding Ma, Christopher J Kiely, and Xinhe Bao. Supported pd–cu bimetallic nanoparticles that have high activity for the electrochemical oxidation of methanol. *Chemistry-A European Journal*, 18(16):4887–4893, 2012.

[136] G Mattei, C Maurizio, P Mazzoldi, F DAcapito, G Battaglin, E Cattaruzza, C de Julián Fernández, and C Sada. Dynamics of compositional evolution of pd-cu alloy nanoclusters upon heating in selected atmospheres. *Physical Review B*, 71(19):195418, 2005.

[137] Giorgio Strukul, Francesco Pinna, Marcello Marella, Letizia Meregalli, and Michele Tomaselli. Sol-gel palladium catalysts for nitrate and nitrite removal from drinking water. *Catalysis today*, 27(1):209–214, 1996.

[138] K Sun, J Liu, NK Nag, and ND Browning. Atomic scale characterization of supported pd-cu/γ-al2o3 bimetallic catalysts. *The Journal of Physical Chemistry B*, 106(47):12239–12246, 2002.

[139] V Mukundan, BN Wanjala, R Loukrakpam, J Luo, J Yin, CJ Zhong, and O Malis. Limited grain growth and chemical ordering during high-temperature sintering of ptnico nanoparticle aggregates. *Nanotechnology*, 23(33):335705, 2012.

[140] Derrick Mott, Jun Yin, Mark Engelhard, Rameshwori Loukrakpam, Paul Chang, George Miller, In-Tae Bae, Narayan Chandra Das, Chongmin Wang, Jin Luo, et al. From ultrafine thiolate-capped copper nanoclusters toward copper sulfide nanodiscs: a thermally activated evolution route. *Chemistry of Materials*, 22(1):261–271, 2009.

[141] Francis P Zamborini, Stephen M Gross, and Royce W Murray. Synthesis, characterization, reactivity, and electrochemistry of palladium monolayer protected clusters. *Langmuir*, 17(2):481–488, 2001.

[142] Jitendra Kumar and Rakesh Saxena. Formation of nacl-and cu¡ sub¿ 2¡/sub¿ o-type oxides of platinum and palladium on carbon and alumina support films. *Journal of the Less Common Metals*, 147(1):59–71, 1989.

[143] Robert T Downs and Michelle Hall-Wallace. The american mineralogist crystal structure database. *American Mineralogist*, 88(1):247–250, 2003.

[144] Jun Yin, Shiyao Shan, Lefu Yang, Derrick Mott, Oana Malis, Valeri Petkov, Fan Cai, Mei Shan Ng, Jin Luo, Bing H Chen, et al. Gold–copper nanoparticles: Nanostructural evolution and bifunctional catalytic sites. *Chemistry of Materials*, 24(24):4662–4674, 2012.

[145] Pierre Villars, Hiroaki Okamoto, and Karin Cenzual. Asm alloy phase diagrams center. *ASM International, Materials Park*, 2006.

[146] Miho Yamauchi and Tatsuya Tsukuda. Production of an ordered (b2) cupd nanoalloy by low-temperature annealing under hydrogen atmosphere. *Dalton Transactions*, 40(18):4842–4845, 2011.

[147] D Madoc Jones and EA Owen. Experimental study of the variation of the degree of order with temperature in a copper-palladium alloy. *Proceedings of the Physical Society. Section B*, 67(4):297, 1954.

[148] Vineetha Mukundan, Jun Yin, Chuan-Jian Zhong, and Oana Malis. Phase transformations in physical mixtures of pd-cu nanoparticles. In *MRS Proceedings*, volume 1528, pages mrsf12–1528. Cambridge Univ Press, 2013.

[149] Vicente Sanchez-Escribano, Laura Arrighi, Paola Riani, Rinaldo Marazza, and Guido Busca. Characterization of pd-cu alloy nanoparticles on γ-al2o3-supported catalysts. *Langmuir*, 22(22):9214–9219, 2006.

[150] Suzanne Giorgio and Claude Henry. Bimetallic pdcu and pdcu _3 particles prepared by wet impregnation-hrtem study of the structure and the interface with the mgo substrate. *Microscopy Microanalysis Microstructures*, 8(6):379–391, 1997.

[151] Ling Zhu, KS Liang, B Zhang, JS Bradley, and Andrew E DePristo. Bimetallic pd–cu catalysts: X-ray diffraction and theoretical modeling studies. *Journal of Catalysis*, 167(2):412–416, 1997.

[152] Vaishali Shah and Liqiu Yang. Nanometre fcc clusters versus bulk bcc alloy: the structure of cu-pd catalysts. *Philosophical Magazine A*, 79(8):2025–2049, 1999.

[153] AJ Renouprez, K Lebas, G Bergeret, JL Rousset, and P Delichere. Supported pd-cu catalysts prepared from bimetallic organo-metallic complexes: relation between surface composition measured by ion scattering and reactivity. *Studies in Surface Science and Catalysis*, 101:1105–1114, 1996.

[154] John S Bradley, Grayson H Via, Laurent Bonneviot, and Ernestine W Hill. Infrared and exafs study of compositional effects in nanoscale colloidal palladium-copper alloys. *Chemistry of materials*, 8(8):1895–1903, 1996.

[155] AM Molenbroek, S Haukka, and BS Clausen. Alloying in cu/pd nanoparticle catalysts. *The Journal of Physical Chemistry B*, 102(52):10680–10689, 1998.

[156] Lefu Yang, Shiyao Shan, Rameshwori Loukrakpam, Valeri Petkov, Yang Ren, Bridgid N Wanjala, Mark H Engelhard, Jin Luo, Jun Yin, Yongsheng Chen, et al. Role of support–nanoalloy interactions in the atomic-scale structural and chemical ordering for tuning catalytic sites. *Journal of the American Chemical Society*, 134(36):15048–15060, 2012.

[157] Vineetha Mukundan, Jun Yin, Pharrah Joseph, Jin Luo, Shiyao Shan, Dmitri N Zakharov, Chuan-Jian Zhong, and Oana Malis. Nanoalloying and phase transformations during thermal treatment of physical mixtures of pd and cu nanoparticles. *Science and Technology of Advanced Materials*, 15(2):025002, 2014.

[158] D Madoc Jones and EA Owen. Experimental study of the variation of the degree of order with temperature in a copper-palladium alloy. *Proceedings of the Physical Society. Section B*, 67(4):297, 1954.

[159] K Baba, U Miyagawa, K Watanabe, Y Sakamoto, and TB Flanagan. Electrical resistivity changes due to interstitial hydrogen in palladium-rich substitutional alloys. *Journal of Materials Science*, 25(9):3910–3916, 1990.

[160] Aaron C Johnston-Peck, Junwei Wang, and Joseph B Tracy. Formation and grain analysis of spin-cast magnetic nanoparticle monolayers. *Langmuir*, 27(8):5040–5046, 2011.

[161] Venugopal Santhanam and Ronald P Andres. Microcontact printing of uniform nanoparticle arrays. *Nano Letters*, 4(1):41–44, 2004.

[162] Paul Meakin. Diffusion-limited droplet coalescence. *Physica A: Statistical Mechanics and its Applications*, 165(1):1–18, 1990.

[163] R Mendoza, I Savin, K Thornton, and PW Voorhees. Topological complexity and the dynamics of coarsening. *Nature materials*, 3(6):385–388, 2004.

[164] Jordi Soriano, Ido Braslavsky, Di Xu, Oleg Krichevsky, and Joel Stavans. Universality of persistence exponents in two-dimensional ostwald ripening. *Physical review letters*, 103(22):226101, 2009.

[165] Jin Luo, Lingyan Wang, Derrick Mott, Peter N Njoki, Nancy Kariuki, Chuan-Jian Zhong, and T He. Ternary alloy nanoparticles with controllable sizes and composition and electrocatalytic activity. *Journal of Materials Chemistry*, 16(17):1665–1673, 2006.

[166] Lingqi Yang, Yong Gan, Yuwen Zhang, and JK Chen. Molecular dynamics simulation of neck growth in laser sintering of different-sized gold nanoparticles under different heating rates. *Applied Physics A*, 106(3):725–735, 2012.

VITA

VITA

Vineetha Mukundan completed her bachelor's in science from Madras University, India and master's in science from Indian Institute of Technology, Madras, India. She came to the US to pursue a PhD degree in physics from Purdue University. Her research interests focusses on characterization of nanomaterials for structure-property-processing relationship. Most of her PhD work was carried out in Brookhaven National Laboratory and Purdue University.